Study on the plasma waves observed by single spacecraft interferometry in the terrestrial inner magnetosphere

Tomoe Taki

2024

Acknowledgements

I would like to express my gratitude to all people who supported my research.

I would like to express my gratitude to my supervisor, Professor Hirotsugu Kojima of Kyoto University RISH. He kindly guided me when my research was going well and when it was not. Whenever I asked him to take time out of his busy schedule, he always made time to consult with me. I am very grateful for your concern not only for my research results but also for my physical and mental health.

I would also like to express my gratitude to Associate Professor Satoshi Kurita of Kyoto University RISH. He supported my research by discussing with me so many times when I was struggling with the analysis and interpretation of the results. Both professors took special time to discuss with me after I left Kyoto University until I finished my dissertation, for which I am very grateful.

Assistant Professor Yoshikatsu Ueda of Kyoto University RISH gave me direct guidance for one year, and the knowledge and experience I gained during that period were utilized in my subsequent research life. I appreciate his support.

Professor Tetsuji Matsuo of Kyoto University and Professor Yusuke Ebihara of Kyoto University RISH, who reviewed my research, gave me many critical comments on my research at various points in my research life. I cannot count the number of times I have been supported by their words.

Professor Yoshiharu Omura, Professor Naoki Shinohara, Associate Professor Tomohiko Mitani, Junior Associate Professor Yikai Hsieh and Assistant Professor Bo Yang of the Space Group gave me many valuable comments at the research meetings. I thank them for their useful comments. I am grateful to Designated Assistant Professor Satoko Nakamura of Nagoya University for her detailed consultation in the unknown early stages of the research. I was very grateful to her for her detailed concern for me in spite of her busy schedule, which was both admirable and encouraging.

I am grateful to the members of the Arase satellite PWE, MGF, and LEP-e for their willingness to allow me to use their valuable observation data. I hope that I have been able to repay their help in some small way with the results of this research. I am especially grateful to Professor Yoshiya Kasahara of Kanazawa University, Professor Yoshizumi Miyoshi of Nagoya University ISEE, Dr. Yoichi Kazama of ACADEMIA SINICA, Professor Hideyuki Usui of Kobe University, and Professor Iku Shinohara of ISAS/JAXA for their constant concern for the results of this research.

I thank Kyoto University Division of Graduate Studies for their support. Thanks to them, I was able to concentrate on my research and attend many academic conferences.

Thank you to everyone at SCREEN Semiconductor Solutions. They encouraged my doctoral thesis in parallel with my daily work.

I would like to thank Ms. Etsuko Kawasaki and Ms. Etsuko Ito, secretaries of Kojima Laboratory, for supporting my research life a lot. I would like to thank all the students in the Space Group. Especially, Dr. Ryo Mochizuki, Mr. Motoyuki Kikukawa, Mr. Katsumi Kawai, and Mr. Ibuki Fukasawa, who were enrolled in the doctoral course at the same period, provided me with many consultations in daily life, and thanks to them, I could enjoy my research life with friendly competition. I would like to thank my friends who were enrolled in doctoral programs at other graduate departments at the same period. It was an invaluable time for me to exchange many words with them about both my research and my research life.

I would like to thank my parents. They encouraged my decision to go to the doctoral program and warmly watched over me during the period when I was not able to achieve results in my research.

Thanks to their help, I was able to complete this doctoral thesis.

Abstract

This study investigates the plasma waves in the Earth's inner magnetosphere using single spacecraft interferometry observations. The primary focus is on Electrostatic Solitary Waves (ESW) and Whistler-mode Chorus Waves, observed by the Arase satellite. Interferometry, an observational technique typically involving multiple observation points, was adapted for use with a single spacecraft, allowing for detailed analysis of the spatial and velocity characteristics of plasma waves.

The Earth's magnetosphere is a region of space dominated by the Earth's magnetic field, containing various plasma environments depending on the region. This study highlights the importance of satellite observations in understanding these environments. Specifically, the interferometry method enables the calculation of wave velocities and spatial scales, crucial for interpreting the plasma dynamics and wave dispersion relations.

The Arase satellite, equipped with advanced plasma wave experiment (PWE) instruments, provided high-resolution data for this study. The methodology involved analyzing electric field waveforms to determine the time differences, and subsequently the spatial scales and velocities of the observed ESW and chorus waves. The study also utilized numerical simulations to model the observed wave characteristics and validate the interferometry observations.

ESW, characterized by bipolar electric field waveforms, were observed in the inner magnetosphere. The spatial scales of these waves ranged from several hundred meters to several kilometers. A two-dimensional Gaussian model was proposed to describe the solitary potentials, and numerical simulations successfully reproduced the observed waveforms. The study also discussed the potential role of ESW in particle acceleration processes within the magnetosphere.

Chorus waves, electromagnetic in nature, were analyzed using phase difference calculations from the Arase satellite data. These waves, polarized perpendicularly to the background magnetic field, displayed distinct phase velocity characteristics. The interferometry model developed for chorus waves explained the observed spin dependence of phase differences and provided upper and lower limits for the phase velocities.

ECH waves were another focal point of this study. Analysis of these waves revealed significant phase differences and apparent phase speeds. By developing an interferometry observation model for ECH waves, the study was able to explain the observed spin dependence numerically. Furthermore, the study presented a method to estimate the wave vector direction and derived dispersion relations consistent with theoretical predictions, providing insights into the cold electron temperature in the inner magnetosphere.

This comprehensive study demonstrated the efficacy of single spacecraft interferometry in observing and analyzing plasma waves in the Earth's inner magnetosphere. The findings contribute to a better understanding of the plasma environments and wave-particle interactions in

this region. Future work may involve expanding these methodologies to multi-spacecraft missions for even more detailed spatial and temporal resolution of magnetospheric dynamics.

Contents

Chapter 1

General introduction

1.1 Magnetosphere

In the Earth's magnetosphere, there are various plasma environments in each region. A schematic diagram of the magnetosphere is shown in Figure 1.1[1]. The Earth's magnetosphere has the shape of being swept away by the solar wind, and the bow shock is distorted by solar activity. The area near the magnetic equator on the anti-solar side is called the plasma sheet, where low-density, high-temperature plasma exists. When a solar flare occurs, reconnection of magnetic field lines occurs in the plasma sheet, and high-temperature plasma particles are transported with the magnetic field lines to the vicinity of the Earth[2]. On the other hand, the area near the Earth at altitudes above about 70 km is called the ionosphere, where both the neutral atmosphere and ionized plasma exist. Plasma density varies with altitude and day/night, but there is a high density of low-temperature plasma[3]. The upper region of the ionosphere is called the inner magnetosphere. Within the inner magnetosphere, various plasma environments have been observed depending on the location. In the plasmasphere, which is the innermost part of the inner magnetosphere, low-temperature, high-density plasma exists, and outside the plasmasphere, the plasma density drastically decreases. On the other hand, there is a region where many high-energy particles exist, called the radiation belt. This region is also called the Van Allen Belts because it was discovered by the Explorer 1 satellite launched by Van Allen's group in 1958. Satellite observations are important for understanding the plasma environment in the Earth's magnetosphere.

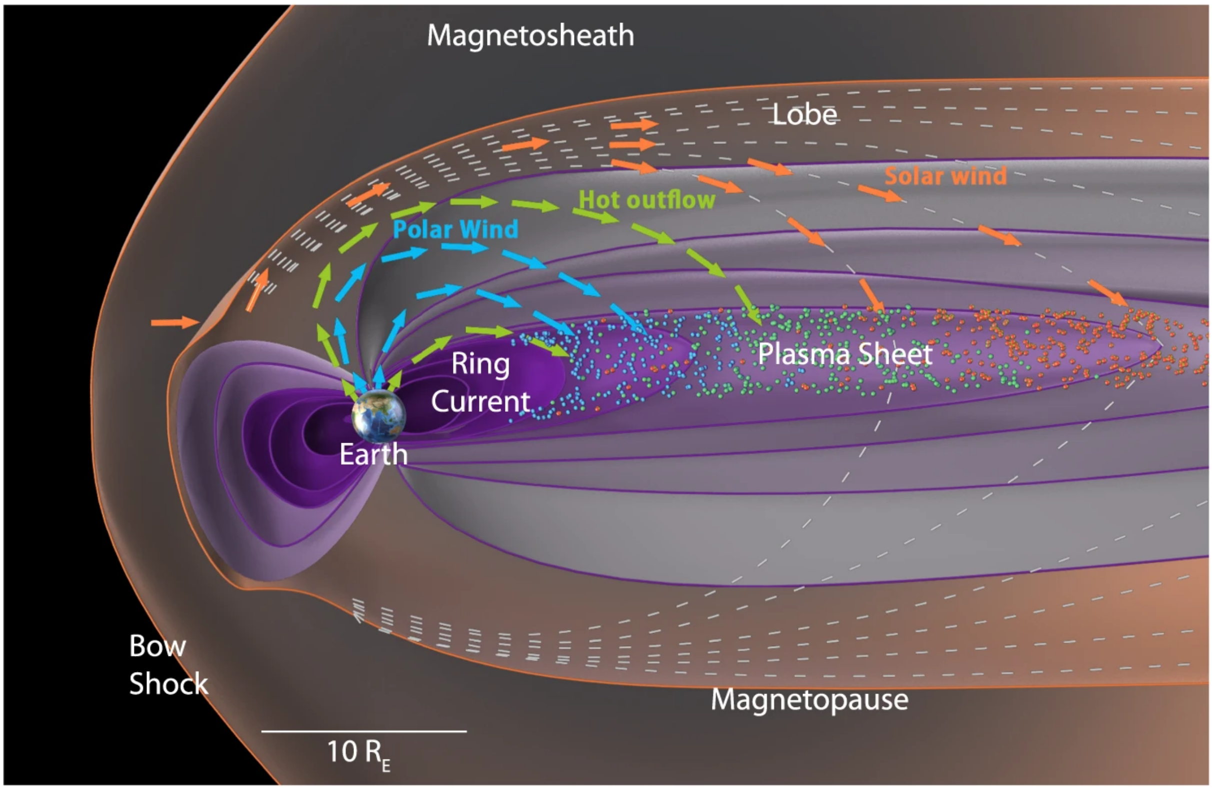

Figure 1.1: Schematic diagram of the magnetosphere[1]

1.2 Interferometry observation

For example, Electrostatic Solitary Waves (ESW) were known as Broadband Elestrostatic Noise (BEN) because only broadband electrostatic spectra were obtained in spectral observations. The GEOTAIL satellite waveform observation revealed that the spectra are ESW. The characteristics of the field oscillation suggested that it is a spatially spreading electrostatic solitary potential.

The observation of the velocity of waves is of particular importance. Waves are known to be excited according to the dispersion relation.

Among wave observations by satellites, it is possible to estimate the plasma environment at the time of excitation of the waves by examining each parameter of the waves in space. The phase velocity of waves is particularly important. This is because the dispersion relation can be obtained by determining the phase velocity of the waves.

In addition, since the ESW is a spatial potential, it is possible to calculate the spatial scale by obtaining the relative velocity to the satellite. It has been suggested that there is fine spatial structure in the ionosphere and magnetosphere, and the structure and magnitude of the isolated potential is important.

In order to obtain the velocity of waves from observations, interferometry observation is performed. Interferometry observation is an observation method that makes it possible to calculate the velocity and spatial scale of an object by simultaneously observing the same object from multiple points. It is used to observe the structure of active volcanoes by observing the ground from an aircraft, or to observe the depth of water by acoustic exploration underwater. For satellites in the magnetosphere, interferometry observations can be used to obtain spatial scales of potential structures and velocities of waves in the region.

Satellite interferometry observations can be performed by multiple satellites or by a single satellite. The Dynamics Explorer (DE) satellites were launched by the United States in 1981. Simultaneous observations were conducted using the DE-1 satellite, which orbited at a high altitude from 600 km to 4 Re, and the DE-2 satellite, which orbited at a low altitude from 300 km to 1300 km. These observations were carried out to elucidate the coupling processes between the atmosphere, ionosphere, and magnetosphere. The temperature and density distribution of hot plasma, as well as electric and magnetic fields, were measured[4].

The Cluster II satellites, launched in 2000 under the leadership of ESA, perform observations in formation flights of four satellites. They traveled the boundary between the magnetosphere and the solar wind, and revealed small-scale plasma structures through simultaneous multi-point observations. In May 2008, the Cluster satellite also performed a measurement called a tilt campaign. Two satellites were navigated in close proximity and the spin axis of one was tilted 46 degrees. By comparing the spin modulation of the electric field waveforms of the two satellites, elliptical polarization was observed[5].

The Magnetospheric Multiscale Mission (MMS) satellites were launched by NASA in 2015. The MMS satellites consist of four satellites from A to D. They sail at high altitude to observe the day side magnetopause and magnetotail.

The Radiation Belt Storm Probes (RBSP) satellites consisted of two satellites launched from A and B to observe the Van Allen Belt mainly.

The THEMIS satellites, five of which were launched to observe the Van Allen zone, were used to observe the magnetotail[6]. Five THEMIS satellites were launched into the magnetosphere, and two of them later orbited the Moon as ARTEMIS satellites. One of them, ARTEMIS P1 (THEMIS-B), performed a lunar wake flyby to observe the electrostatic wave. The phase velocity was calculated by comparing the phase of the electrostatic fields between the two antennas. It was suggested that the electrostatic field is excited by the electron beam generated by the net potential due to the lunar wake[7, 8].

On the other hand, the Arase satellite, which is the subject of this study, was launched as a single satellite to perform interferometry observations.

The Arase satellite is a satellite that performs observations in the Earth's inner magnetosphere, and has an elliptical orbit with an altitude of about 460 km at perigee and about 32110 km at apogee. It has a large orbital inclination angle and observes a wide range of regions from high magnetic latitudes to the magnetic equator.

The Arase satellite maintains its attitude by spinning with an 8-second period, and the spin angle is in the direction of the sun. It has a wire probe for electric field observation and a search coil for the next observation on the spin surface. Arase satellites normally perform dipole observations for each antenna pair. By treating the two antennas as separate monopole antennas, Arase satellite treats them as two different observation points and achieves interferometry observation with a single satellite. The RBSP satellite is an example of a quasi interferometry observation by calculating the electric field of each antenna in a quasi-analytical method by assuming the satellite potential for a single satellite.

There are only a few examples of interferometry observations with a single satellite. In addition, each satellite has a different antenna system and satellite size, so it is necessary to create an observation model for a single satellite.

Furthermore, Arase satellites do not have antennas to observe the electric field in the spin axis direction, which means that some data cannot be observed during interferometry observation. In this study, we propose interferometry observation models for three types of phenomena observed in the magnetosphere: isolated potential structures, electromagnetic waves, and static waves. Then, we attempted to estimate the unobserved components using the proposed observation model, and worked on the calculation of the scale of the spatial structure of the potential and the velocity of the waves. From the results, the plasma environment in the Earth's inner magnetosphere is discussed.

1.3 Objectives of this thesis

The objective of this study is to estimate the plasma environment of the magnetosphere along the Arase satellite's orbit using interferometry observations. In this study, three types of waves were selected as the subjects of interferometry observations.

1.3.1 Electrostatic potential

Electrostatic solitary waves (ESW) are bipolar, pulse-like waveforms observed by the GEOTAIL satellite in the magnetotail region. In the case observed by the GEOTAIL satellite in the magnetotail region, the electric field oscillates only in the direction parallel to the background magnetic field, followed by a bipolar waveform with positive-negative symmetry. The observed electric field waveforms are shown in Figure 1.2 [9, 10]. From these features, a spatial structure of the potential was proposed in which the potential changes in the vertical plane to the background magnetic field. The suggested spatial structure of the potential is shown in Figure

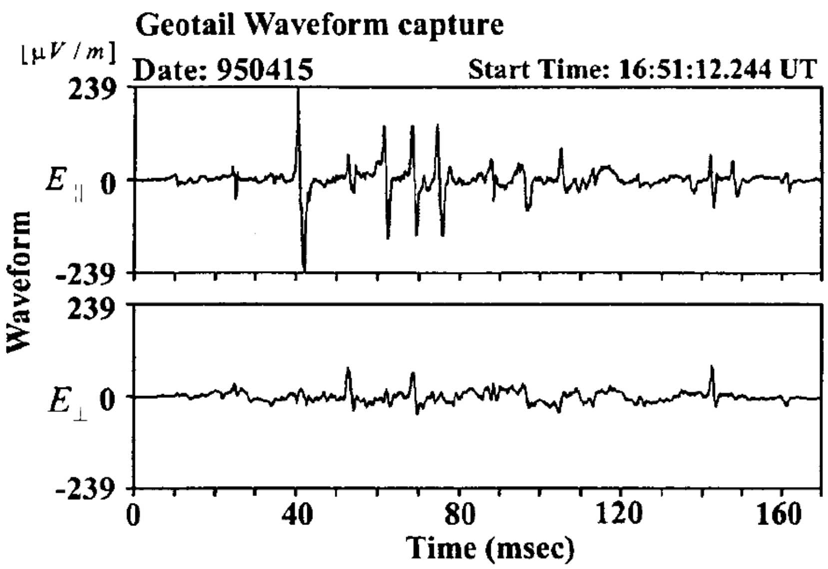

Figure 1.2: Parallel and perpendicular electric field waveforms observed by the GEOTAIL satellite in the magnetotail[10]

1.3[10]. ESW was considered to be observed when a satellite passes through these electrostatic potential structures. The electric field observed on the RBSP satellite is asymmetric in maximum and minimum values, indicating that it has net potential. It was proposed that this could accelerate electrons[11, 12, 13].

1.3.2 Whistler-mode chorus waves

We performed the analysis on Whistler-mode Chorus Waves. Chorus waves are electromagnetic waves excited in the whistler mode. The relationship between frequency and refraction index of R-mode waves, including whistler mode, is shown in Figure 1.4. These are right-hand polarized electromagnetic waves propagating parallel to the direction of the background magnetic field. It is observed in the frequency band of $0.1 f_{\mathrm{ce}}$ to $0.8 f_{\mathrm{ce}}$. Chorus waves cause Landau resonance around 1/2 f_{ce}, which accelerates the electrons and simultaneously damps itself[15, 16, 17]. Upper-band chorus and lower-band chorus occur above and below 1/2 f_{ce}, respectively. A notable feature of these electromagnetic waves is their very high phase velocity.

Chorus waves have different characteristics for upper-band chorus and lower-band chorus. Lower-band chorus tends to have larger amplitudes, while upper-band chorus generally has smaller amplitudes. Upper-band chorus waves with large amplitudes are suggested to accelerate electron precipitation in polar regions, leading to the formation of diffuse auroras[19]. Chorus waves with wave normal angles below 20 degrees and between 60 to 80 degrees are frequently

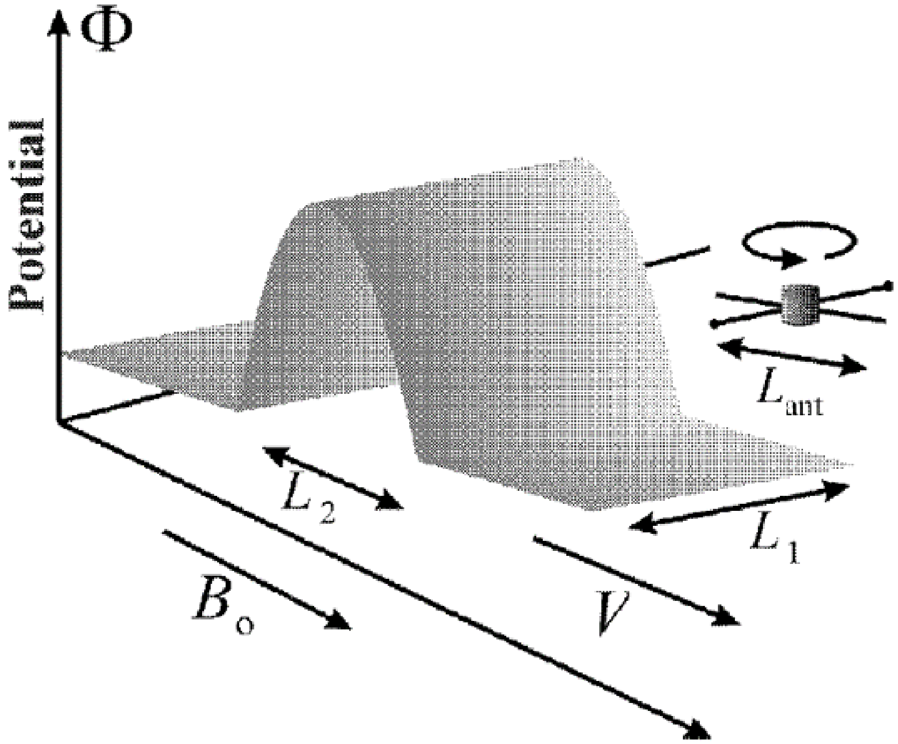

Figure 1.3: Suggested spatial structure of the potential[14]

observed.

1.3.3 Electrostatic electron cyclotron harmonic waves

Electron Cyclotron Harmonics (ECH) waves are one of the plasma waves observed in the magnetosphere. These waves are characterized by a harmonic structure with peaks between integer multiples of the electron cyclotron frequency f_{ce}. ECH waves are electrostatic. The wave vector is approximately perpendicular to the background magnetic field and the electric field oscillations are parallel to the wave vector. ECH wave was first observed by the OGO-5 satellite[20] and has been observed in the magnetosphere of the Earth and other planets and satellites[21, 22, 23, 24]. ECH wave has been reported to have large amplitudes[20, 25], suggesting that it affects the plasma environment. ECH wave has been shown to cause pitch angle scattering[26, 27], which generates diffuse auroras[28]. Since the dispersion relation of ECH waves strongly depends on the parameters of cold electrons, it is possible to estimate the plasma environment, such as the background electron temperature, from the phase velocity of ECH waves.

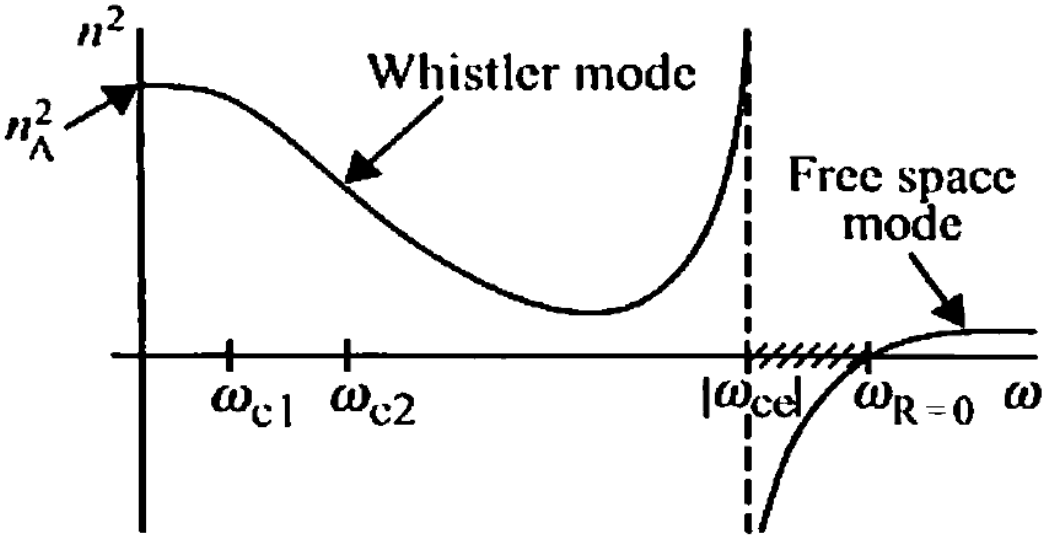

Figure 1.4: Relation between frequency and refraction index for $n^2 = R$ mode [18]

1.4 Outline of this thesis

The remains of this thesis are composed of the following chapters.

- **Chapter 2: Instruments and method for interferometry observation**

  This chapter primarily explains the observation instruments of the Arase satellite, including the PWE, which operates the interferometry observations, as well as the analysis methods for these interferometry observations. Since the Arase satellite observes instantaneously in only one-dimensional direction, the analysis method for waves involves calculating the true wave vector direction from the phase velocity in the one-dimensional direction and the inclination of the wave vector. In the analysis of ESW, the solitary potential is assumed to be a one-dimensional Gaussian. By considering the model waveform of ESW and using the time difference obtained from the interferometry observations along with the electric field waveform, the spatial scale of the solitary potential is calculated.

- **Chapter 3: Application in isolated potential structures: Electrostatic solitary waves**

  We conduct an analysis of ESW. The relative velocity of ESW is high, resulting in small time differences that cannot be sufficiently captured using the method of cross-correlation by shifting the waveforms. On the other hand, the bipolar model waveform created from a Gaussian sometimes does not fit well enough. In this study, we combined these two methods to calculate the spatial scale from the observations. Furthermore, for waveforms that could not be sufficiently fitted, we explained the trends using a model that assumes a two-dimensional Gaussian.

- **Chapter 4: Application in electromagnetic waves: Whistler-mode chorus waves**

  We conducted an analysis of Whistler-mode chorus waves. For chorus waves, periodic variations in phase difference were observed in sync with the satellite's rotation. However, due to the relationship between the propagation direction and the oscillation direction, there was a problem where it was impossible to receive signals when the phase difference was at its maximum. Consequently, we could not estimate the phase velocity from the small phase differences, but we did examine the sampling period and the observable phase differences.

- **Chapter 5: Application in electrostatic waves: Electron cyclotron harmonic waves**

  We conducted an analysis of Electrostatic electron cyclotron harmonic(ECH) waves. The phase velocities for each frequency within the harmonic structure of the ECH waves varied significantly, and in some cases, the two peaks within the same frequency band had different propagation directions. A statistical investigation of the satellite's spin dependency revealed two distinct trends, both of which were reproduced using model waveforms.

- **Chapter 6: Estimation of cold electron temperatures through the dispersion of electron cyclotron harmonic waves**

  Using the model waveforms proposed in Chapter 5, we estimated the wave vector direction. From this, we calculated the phase velocity for each frequency and obtained the dispersion relation. By referencing known particle detector data and comparing the dispersion curves while sweeping through the unknown low-energy electron temperature, we successfully estimated the low-energy electron temperature.

- **Chapter 7: Summary and conclusion**

  Summarize the results obtained in each chapter and present future prospects for measuring the plasma environment in the magnetosphere.

Chapter 2

Instruments and method for interferometry observation

2.1 Instruments

The Arase satellite is in an elliptical orbit with a perigee altitude of ~ 460 km and an apogee altitude of 32,110 km. The satellite is spin-stabilized, with a spin period of approximately 8 seconds, and the spin axis points roughly towards the Sun. Figure 2.1[29] shows the overview of the Arase satellite.

We utilized the data obtained by the Plasma Wave Experiment (PWE)[29], Magnetic Field Experiment (MGF)[30], and Low-energy particle experiments-electron analyzer (LEP-e) onboard the Arase satellite. Four wire probe antennas (WPT)[31] are deployed in the spin plane,

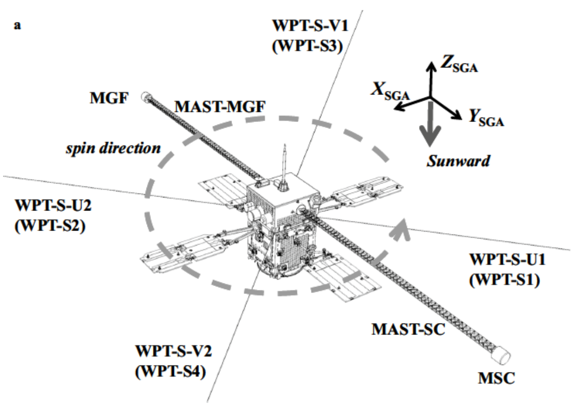

Figure 2.1: Overview of the Arase satellite[29]

forming two pairs of dipole antennas. The four WPT antennas are named U1, U2, V1, and V2, respectively. During nominal operations, the antenna pairs of U1-U2 and V1-V2 function as dipole antennas. During interferometry observations, the internal circuit switches are adjusted to measure the potential differences of V1-U_{sc} and V2-U_{sc}, where U_{sc} is the spacecraft potential. U1 and U2 are not utilized during interferometry observations. The electric field waveforms are computed using this potential difference and a physical antenna length of 15.6 m. Electric field observations made by WPT are processed at sampling frequencies of 65 kHz by Onboard frequency Analyzer (OFA)/Waveform Capture (WFC)[32], covering the frequency range from a few Hz to 20 kHz. Magnetic Search Coils[33] enabling the observation of three-dimensional wave magnetic fields. The waveform data of the three magnetic fields and two electric fields are obtained in burst mode due to their large data size. The electric field spectra observed by both OFA and High Frequency Analyzer (HFA)[34] were utilized to determine the UHR frequency.

MGF observes the three-dimensional background magnetic field and is used to determine the satellite's spin angle relative to the background magnetic field direction. It also enables us to calculate the intensity of the background magnetic field and determine the electron cyclotron frequency.

LEP-e observes electrons in the energy range of approximately 19 eV to 19 keV. The Field of view (FOV) spans 270 degrees parallel to the satellite body. The FOV is divided into 22 directions, with channels 1 to 5 and 18 to 22 having angles spaced at 22.5 degrees intervals, while channels 6 to 17 have fine channels spaced at 3.75 degrees intervals. These FOVs rotate with the satellite's spin, allowing the observation of a three-dimensional distribution function with a time cadence of $\sim$8 seconds. The data is used to compute the density and temperature of electrons in the LEP-e energy range.

2.2 Method for calculating phase velocity and dispersion relations for waves

The dispersion relation of waves is derived from the phase velocity estimated from the interferometry observation performed by the Arase satellite. The electric fields obtained from antennas V1 and V2 during interferometry observations are denoted as E_{V1} and E_{V2}, respectively. The phase velocities are calculated from E_{V1} and E_{V2} using the following procedure:

1. We compute the phase difference $\Delta\theta$ for each frequency using Fourier transform.

$$W_1 = |W_1| \exp(-j\theta_1) \tag{2.1}$$

$$W_2 = |W_2| \exp(-j\theta_2) \tag{2.2}$$

where θ_1 and θ_2 represent the phase of two electric fields respectively. When using the complex conjugate $W_2^* = |W_2| \exp(j\theta_2)$, it can be formulated as in Equation 2.3.

$$W_1 W_2^* = |W_1||W_2| \exp(-j(\theta_1 - \theta_2)) \tag{2.3}$$

The angle of $W_1 W_2^*$ represents the phase difference $\Delta\theta = \theta_1 - \theta_2$. $\arctan W_1 W_2^*$ indicates the phase difference. Thus the phase difference can be calculated as follows.

$$W_i(f) = \mathscr{F}[E_{Vi}(t)] \quad (i = 1, 2), \tag{2.4}$$

$$\Delta\theta = \arctan\langle W_1 W_2^* \rangle, \tag{2.5}$$

where W_1 and W_2 represent the Fourier transforms of E_{V1} and E_{V2}, respectively, and the asterisk denotes complex conjugate. Angle brackets indicate ensemble averaging.

2. We calculate the apparent phase velocity v'_{ph} from the phase difference,

$$v'_{\mathrm{ph}} = \frac{2\pi l f}{\Delta\theta}, \tag{2.6}$$

where l represents the distance between observation points at which electric fields are detected. Assuming the wave electric fields are detected at the midpoint of the wire antennas, l is computed as 15.6 m. Since E_{V1} and E_{V2} represent electric fields within the spin plane, v'_{ph} is the phase velocity projected onto the spin plane.

3. We derive the true phase velocity v_{ph} of the wave from v'_{ph} and the wave vector direction,

$$v_{\mathrm{ph}} = \frac{v'_{\mathrm{ph}}}{\cos\beta}, \tag{2.7}$$

where the angle β represents the angle between the wave vector and the spin plane. The method for computing β is shown in the numerical calculations in Appendix.

We calculated the angular frequency and wavenumber from the phase velocity for each frequency,

$$\omega = 2\pi f, \tag{2.8}$$

$$k(\omega) = \frac{v_{ph}}{\omega}. \tag{2.9}$$

Using the ω and $k(\omega)$ obtained from Equation 2.8 and Equation 2.9, the dispersion relations of observed waves are derived.

2.3 Method for calculating the relative velocity and spatial scale of the isolated electrostatic potential

We show the method for calculating the relative velocity and spatial scale of the isolated electrostatic potential with respect to the satellite. It is assumed that the isolated electrostatic potential is represented by a one-dimensional Gaussian. The electric field waveform is expressed by the Equation 2.11.

$$\phi(x) = \frac{A}{2\pi\lambda^2}\exp\left(-\frac{(x-\nu)^2}{2\lambda^2}\right) \tag{2.10}$$

$$\begin{aligned} E(t) &= \frac{A}{2\pi\lambda^2}\frac{\nu(t-\mu)}{\lambda^2}\exp\left(-\frac{\nu^2(t-\mu)^2}{2\lambda^2}\right) \\ &= \frac{A}{2\pi\sigma^2}\frac{t-\mu}{\nu\sigma^2}\exp\left(-\frac{(t-\mu)^2}{2\sigma^2}\right), \end{aligned} \tag{2.11}$$

where A corresponds to the electric field at the peak and σ to the pulse time width. ν corresponds to the position of the potential, and μ represents the time between the maxima and minima of the pulse waveform. The two observed waveforms are fitted using the function in Equation 2.11, and the values corresponding to the three parameters A, σ, and μ are calculated. The Levenberg-Marquardt least squares method was used for fitting. We denote each parameter obtained from waveform E_{V1} as A_1, σ_1, μ_1, and each parameter obtained from waveform E_{V2} as A_2, σ_2, μ_2, respectively. The time δt taken for the potential to travel between the antennas is equal to $\mu_2 - \mu_1$. The time difference was set to be positive if the waveform appeared earlier in E_{V1} than in E_{V2}. Using this time difference δt, the relative velocity v'_{p} of the potential to the satellite in the direction of the antenna is multiplied as in Equation 2.12.

$$v'_{\mathrm{p}} = \frac{l}{\Delta t} \tag{2.12}$$

where l is the distance between the antennas. $l = 16.2$ m is used as the distance between the antenna midpoints. Let the pulse time width be tau, which is nothing but the time for the potential to pass through the satellite. Since the potential is considered to have passed through the observation point in time with relative velocity v'_{p}, the potential width S' in the direction of the antenna is expressed by Equation 2.13.

$$S' = v'_{\mathrm{p}}\tau \tag{2.13}$$

In order to quantitatively evaluate τ the transit time of the isolated potential structure, the spatial scale of the potential was set to three segments for the potential structure shown in Equation 2.10. Figure 2.2 shows the relationship between the observed waveforms shown in Equation 2.10 and Equation 2.11 and the corresponding potentials. The electric field $E(\mu \pm 3\sigma)$ at both ends of the potential $t = \mu \pm 3\sigma$ is less than 1/90 of the electric field intensity maximum of $E(\mu \pm \sigma)$. Therefore, since the observed electric field is sufficiently small compared to the peak, the this interval is defined as the spatial scale of the potential in this study. From the above, the pulse time width of the observed waveform can be expressed as in Equation 2.14.

$$\tau = 3 \times \Delta T_{\mathrm{pp}} \tag{2.14}$$

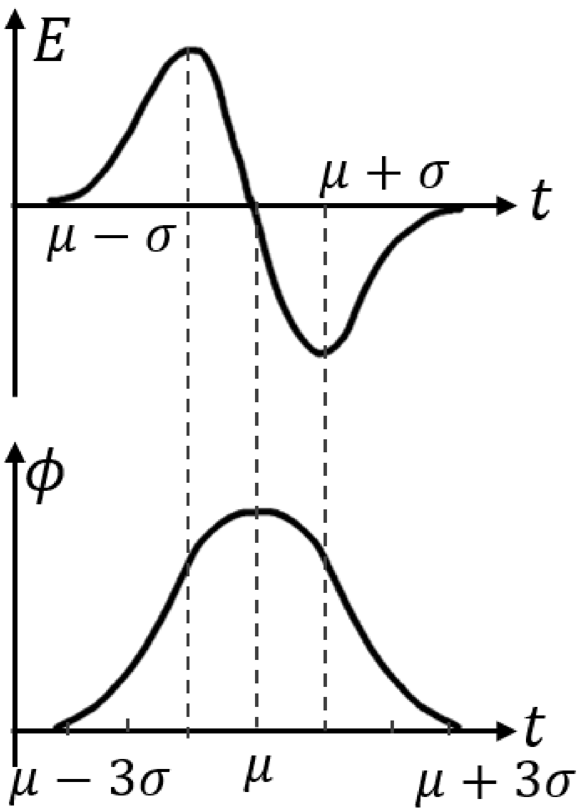

Figure 2.2: Relationship between observed waveforms (top) and corresponding potentials (bottom)

where ΔT_{pp} is the time difference between the maxima and minima of the observed waveform. This method can determine the time difference between E_{V1} and E_{V2} with higher accuracy than the WFC sampling period. This method can determine the time difference between E_{V1} and E_{V2} with a higher accuracy than the sampling period of the WFC. On the other hand, the assumed potential structure does not allow us to determine the applicable electric field waveforms. On the other hand, the assumed potential structure limits the applicable electric field waveforms to positive-negative symmetrical bipolar waveforms.

For solitary waves of other shapes, the relative velocity can also be calculated by obtaining the time difference when the cross-correlation between the two observed waveforms reaches its maximum.

Since the isolated potential is considered to travel in the direction of the background magnetic field, assuming that the direction of the isolated potential is in the direction of B_0, the spatial scale can be calculated. The potential width S' is a parameter of the observed antenna direction. Assuming the direction of travel, the scale of the potential structure can be calculated using the angle β between the antenna direction and the direction of the background magnetic field, as in Equation 2.15.

$$S = S' \cos\beta \tag{2.15}$$

Chapter 3

Application in isolated potential structures: Electrostatic solitary waves

3.1 Introduction

We perform the analysis for Electrostatic Solitary Waves. These are isolated waves characterized by electric fields observed by the satellite, resulting from isolated potentials formed by plasma density variations.

The ESW observed by the GEOTAIL satellite are correlated with electron beams [10]. Observations from the GEOTAIL satellite show that ESW move in the same direction as electron beams with high probability, leading to the assumption that the potential's movement speed is comparable to that of the electron beams. By assuming the movement speed of the potential, we can calculate the relative speed of the potential with respect to the satellite. Using this relative speed and the observed pulse duration, we can determine the spatial scale of the potential corresponding to the observed ESW.

The spatial scale of the sheet-like structure, shown in Figure 1.3, was estimated to be several tens of kilometers in width parallel to the background magnetic field. The width perpendicular to the background magnetic field is estimated to be larger than the parallel width of several tens of kilometers. This is because, in many ESW observed by the GEOTAIL satellite, the electric field waveform does not appear perpendicular to the background magnetic field. Therefore, it is considered that the edges of the potential were not captured within the observation time.

The ESW observed by the GEOTAIL satellite repeatedly showed waveforms of the same shape. The amplitude values of the waveforms are determined by the angle between the antenna and the background magnetic field, which is due to sheet-like structures parallel to the background magnetic field being aligned in parallel. Additionally, Omura et al. [35] conducted computer simulations on the generation of potential structures in the GEOTAIL observation region. The simulation results also show the high stability of one-dimensional ESW. One-dimensional ESW correspond to potential structures where there is a potential change parallel to the magnetic field, and equipotential surfaces in the perpendicular plane.

It was reported that ESW were observed in the Earth's inner magnetosphere[36, 37, 38, 11, 39, 40].

Interferometric observations of ESW by multiple satellites include the Cluster and MMS satellites. On the cluster satellites, the time difference in ESW could be calculated by comparing the electric field waveforms between SC3 and SC4[40].

Mozer et al. [41] calculated the time difference in ESW seen between MMS1 and MMS4, 29.3 km apart, to estimate the speed of ESW.

ESW were observed also by the RBSP satellite is shown in Figure 3.1. The electric field waveform observed by the RBSP satellite has a positive-negative asymmetric shape and is followed by pulse waves with different shapes. The positive-negative asymmetry suggests that it may contribute to the acceleration of electrons subjected to that electric field[11, 12]. Here, a potential structure is considered, in which a potential difference exists before and after the pulse, and is called a double layer[36]. The relative velocity of this potential is estimated to be $20,000 \pm 10,000$ km/s, which has a large error[42].

3.2 Event analysis

Figure 3.2 shows the ESW observed by interferometry observation mode of the Arase satellite. Both positive-negative symmetric bipolar waveforms and positive-negative asymmetric waveforms are observed, indicating that waveforms of different shapes are continuously observed. Furthermore, some of the cross-correlations between the two waveforms are low. The field oscillations from 05.683 seconds to 05.684 seconds in the figure have both E_{V1} and E_{V2} with bipolar waveforms. The second waveform from 05.685 seconds to 05.686 seconds is positive-negative asymmetric for both E_{V1} and E_{V2} , but has a different shape. The third waveform at 05.687 seconds is positive-negative asymmetric for E_{V1} and bipolar for E_{V2} . The square wave-like fluctuation seen at 05.682 seconds does not appear in the waveforms obtained by adding E_{V1} and E_{V2} , indicating that this is common-mode noise.

Among these, the bipolar waveforms with high correlation and positive-negative symmetry were used for the analysis to calculate the ESW time difference. Sixteen samples of waveforms were selected for analysis. The observed time of each waveform is shown in the Table 3.1.

Cross-correlation was used to calculate the time difference. From the cross-correlation anal-

Table 3.1: observed time of each waveform selected

Sample number	Observation date and time
1	2018-10-07/13:02:05.683
2	2018-10-07/13:02:06.258
3	2018-10-07/13:02:06.264
4	2018-10-07/13:02:06.365
5	2018-10-07/13:02:06.402
6	2018-10-07/13:02:06.443
7	2018-10-07/13:02:06.487
8	2018-10-07/13:02:06.581
9	2018-10-07/13:02:07.429
10	2018-10-07/13:02:07.593
11	2018-10-07/13:02:07.900
12	2018-10-07/13:03:21.064
13	2018-10-07/13:03:21.161
14	2018-10-07/13:03:21.650
15	2018-10-07/13:03:21.676
16	2018-10-07/13:03:21.682

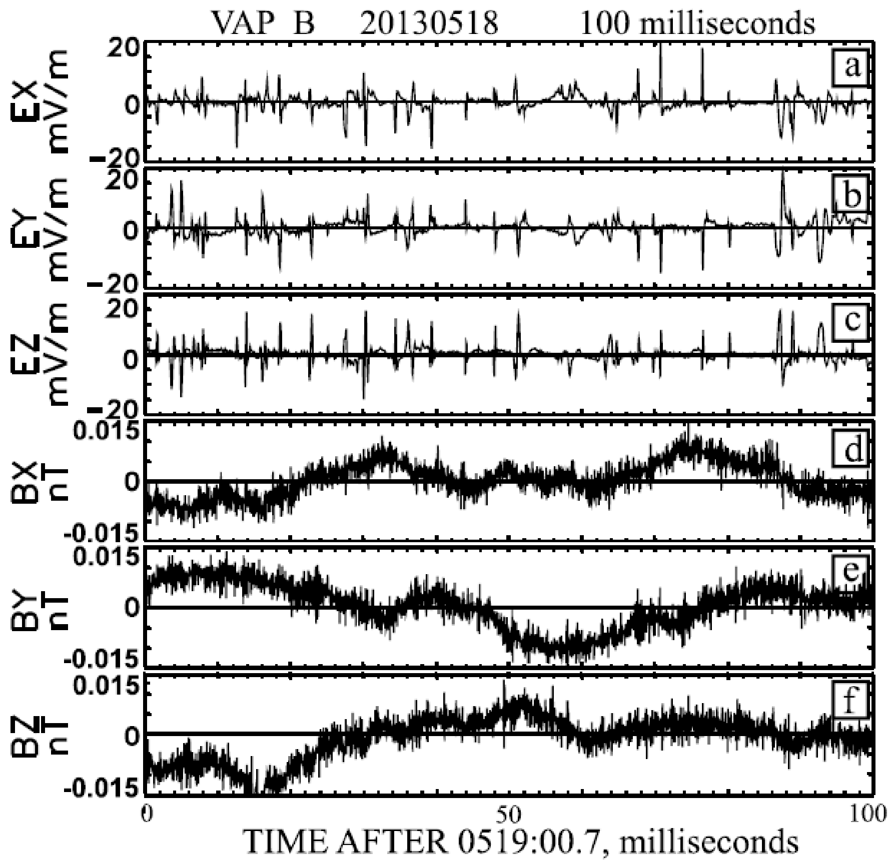

Figure 3.1: Electric field waveforms observed by interferometry observation mode of the RBSP satellite in the magnetosphere[39]

ysis of the two interferometry waveforms E_{V1} and E_{V2} , we show how to calculate the relative velocity of the potential structure to the satellite and the spatial scale. Although the time resolution is limited by the sampling period, this method has the advantage that the analysis can be performed without assuming a potential structure.

First, the cross-correlation coefficients between E_{V1} and E_{V2} are calculated, and the time difference at which the correlation coefficient reaches its maximum is calculated. In this case, the time difference when the waveform appears earlier in E_{V1} than in E_{V2} is set to be positive. The time difference Δt at which the correlation reaches its maximum corresponds to the time taken for the potential to travel between the antennas, and the relative velocity v_{p}' of the potential structure in the direction of the antenna to the satellite can be calculated using Equation 2.12. The results are shown in the Table 3.2. In this result, $15.2\,\mu$s is one sampling frequency of WFC. This means that most of the ESW time differences are considered to be less than one sampling.

As an example of the results of the fitting process, the results for sample number 13 are

Table 3.2: Time difference, relative velocity, and spatial scale in antenna direction obtained from cross-correlation for each waveform

Sample number	Time difference Δt [μs]	Relative velocity v'_{p} [km/s]	Spatial scale in the antenna direction S' [m]
1	15.2	1065	829
2	15.2	1065	634
3	0	-	-
4	15.2	1065	732
5	0	-	-
6	0	-	-
7	0	-	-
8	0	-	-
9	-15.2	-1065	439
10	0	-	-
11	0	-	-
12	0	-	-
13	0	-	-
14	0	-	-
15	0	-	-
16	15.2	-1065	683

shown in Figure 3.3. This fitting result shows good agreement. On the other hand, if we refer to the waveform of sample number 9 shown in Figure 3.4, we can see that the observed waveform has a different shape compared to the fitting function. Although the observed waveform is bipolar, it is not positive-negative asymmetric, and the absolute value of the electric field intensity at the minimum value of the electric field is larger than the maximum value. The pulse width is also smaller in the positive electric field region and larger in the negative field region. Such waveforms existed in 14 of the 16 cases. In this case, the results are not significant because the fitting function is not appropriate. Furthermore, in one of the remaining two cases, the signal intensity of the bipolar waveform was not large enough for the noise and was not suitable for fitting. Therefore, sample number 13 is the only one that is represented by Equation 2.11 and is considered to have obtained a significant time difference. For bipolar waveforms with positive-negative symmetry, this method enabled the calculation of time differences with a higher resolution than that of the sampling period.

The spatial scale was calculated for the samples for which time differences were obtained, as shown in the Table 3.3.

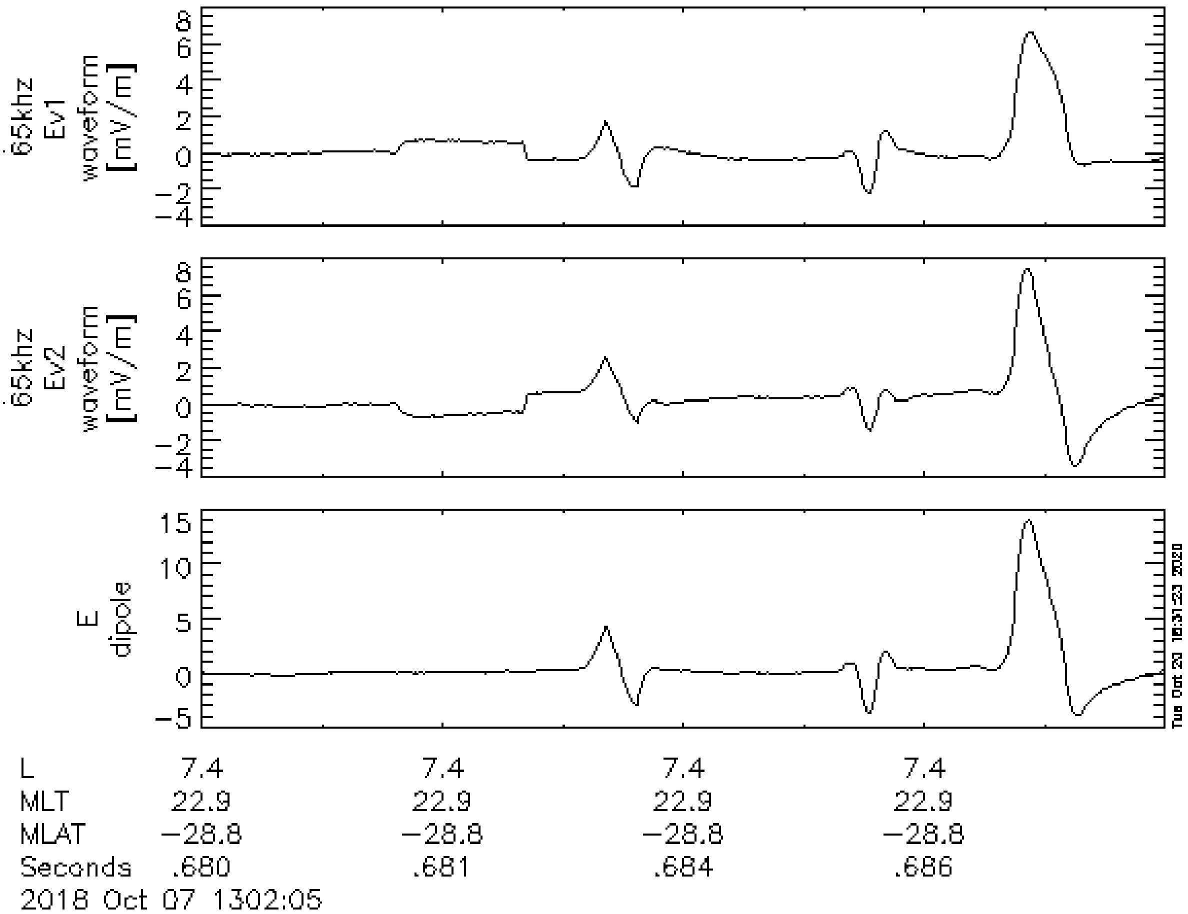

Figure 3.2: Two electric field waveforms observed by interferometry observation mode of the Arase satellite and their summed waveforms

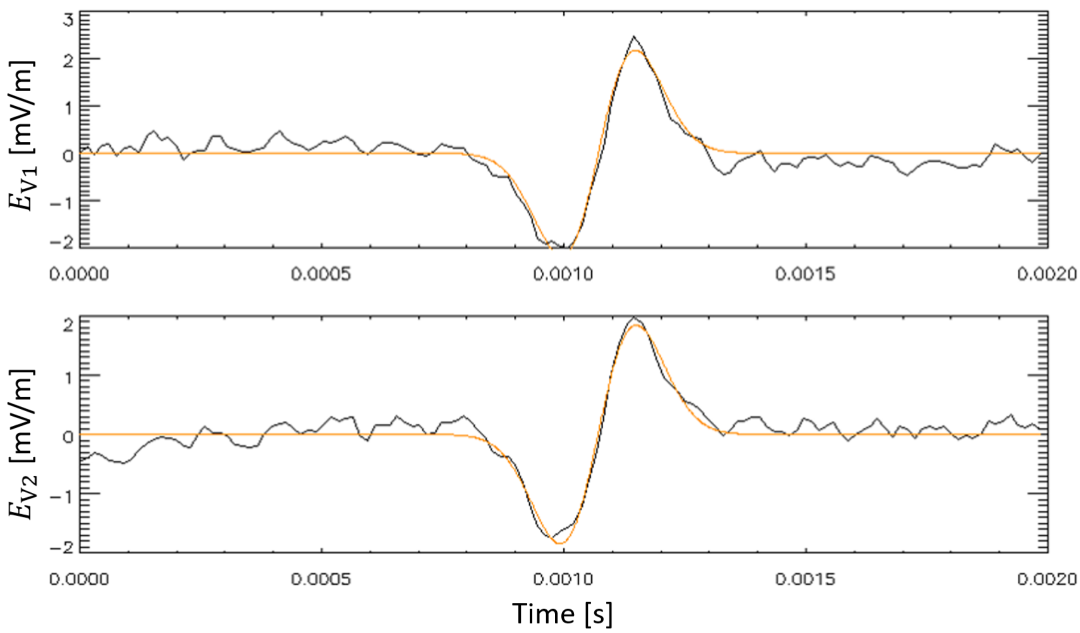

Figure 3.3: ESW observed by the Arase satellite at 2018-10-07/13:03:21.161 and labeled with sample number 13. Black lines show the observed electric field waveforms and orange lines show the fitted waveforms

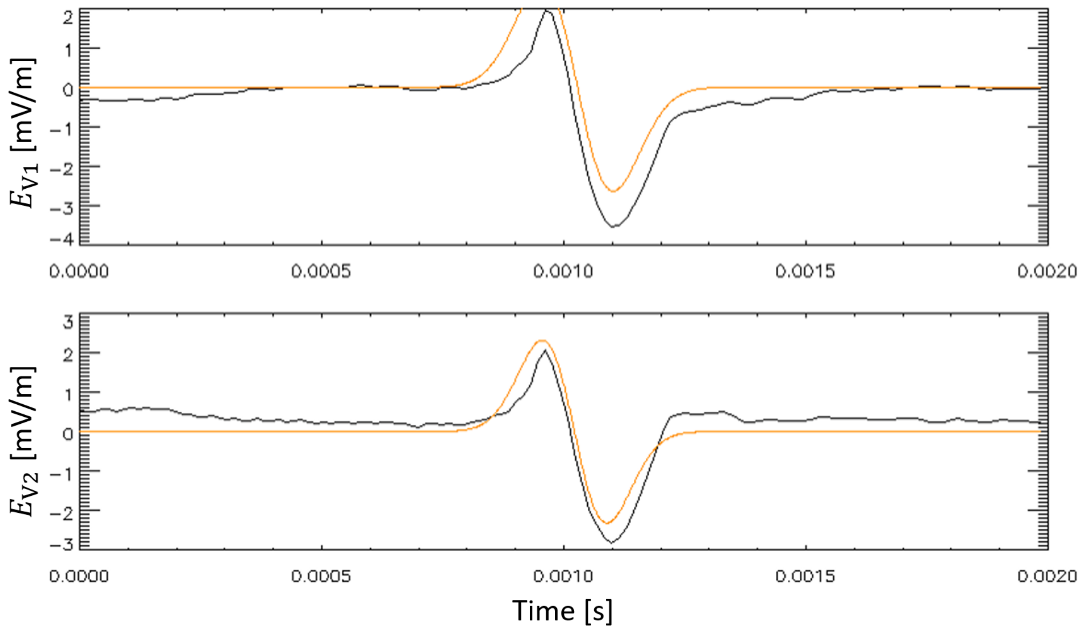

Figure 3.4: ESW observed by the Arase satellite at 2018-10-07/13:02:07.429 and labeled with sample number 9. Black lines show the observed electric field waveforms and orange lines show the fitted waveforms

Table 3.3: Calculated time difference, relative velocity, spatial scale in antenna direction, and the method used for each waveform

Sample number	Time difference Δt [μs]	Spatial scale in antenna direction S' [km]	Spatial scale S [km]	Methods used
1	15.2	0.829	0.48	Cross-correlation
2	15.2	0.634	0.54	Cross-correlation
4	15.2	0.732	0.66	Cross-correlation
9	-15.2	0.439	0.38	Cross-correlation
13	-0.64	13.896	3.6	Fitting
16	15.2	0.683	0.43	Cross-correlation

3.3 Numerical calculation

3.3.1 Calculation method

On a 2D plane with a side length of 1500 m, we consider a potential represented by a 2D Gaussian as shown in Equation 3.1.

$$\phi(x) = -\frac{1}{2\pi\sigma^2}\exp\left(-\frac{(x-\mu)^2}{2\sigma^2}\right)\exp\left(-\frac{(y-\nu)^2}{2\sigma^2}\right) \tag{3.1}$$

Based on the data analysis results of the Arase satellite, the estimated spatial scale of the potential ranged from several hundred meters to several kilometers. To ensure a 3σ interval of 1000 m, we set $\sigma = 166$. The computational space for numerical experiments is divided into a 6000×6000 grid.

In the numerical experiments, we determine the potential at three points: the center of the satellite and two observation points located at an antenna length away from the center. This allows us to reproduce the electric field observed in interferometry observations.

Assuming the satellite's center moves with a velocity v along the X-axis, denoted by $[x_{\mathrm{sat}}, y_{\mathrm{sat}}]$, the coordinates of the two observation points, $[x_1, y_1]$ and $[x_2, y_2]$, are given by Equation 3.2, Equation 3.3, and Equation 3.4.

$$[x_1, y_1] = [x_{\mathrm{sat}} - L_{\mathrm{a}}\cos\theta, y_{\mathrm{sat}} - L_{\mathrm{a}}\sin\theta] \tag{3.2}$$
$$[x_2, y_2] = [x_{\mathrm{sat}} + L_{\mathrm{a}}\cos\theta, y_{\mathrm{sat}} + L_{\mathrm{a}}\sin\theta] \tag{3.3}$$
$$[x_{\mathrm{sat}}, y_{\mathrm{sat}}] = [x_0 + vt, y_0] \tag{3.4}$$

Here, L_{a} is the antenna length, set to 10 m for simplicity, and θ is the angle the antenna forms with the direction the potential passes through. When $\theta = 0$, the vector from observation point $[x_1, y_1]$ to $[x_2, y_2]$ aligns with the direction of motion. The Arase satellite is a spin satellite, and as a result, the angle of the antenna with respect to the direction of the potential changes over time. However, since the spin period of the Arase satellite is 8 seconds, which is sufficiently large compared to the few milliseconds it takes for the satellite to pass through the potential, the effect of the satellite's rotation can be ignored. Therefore, in this calculation, θ is given as a constant.

Let the potential at the center point of the satellite $[x_{\mathrm{sat}}, y_{\mathrm{sat}}]$ be P_{sat}, and the potentials at the observation points $[x_1, y_1]$ and $[x_2, y_2]$ be P_1 and P_2 respectively. The observed electric field is determined by Equation 3.5 and Equation 3.6.

$$E_1 = \frac{P_1 - P_{\text{sat}}}{L_{\text{a}}} = \frac{\phi(x_1, y_1) - \phi(x_{\text{sat}}, y_{\text{sat}})}{L_{\text{a}}} \tag{3.5}$$

$$E_2 = -\frac{P_{\text{sat}} - P_2}{L_{\text{a}}} = -\frac{\phi(x_2, y_2) - \phi(x_{\text{sat}}, y_{\text{sat}})}{L_{\text{a}}} \tag{3.6}$$

At this point, the positive direction of the observed electric field is determined with respect to the Arase satellite. In other words, E_1 is positive in the direction from observation point 1 towards the satellite, and E_2 is positive in the direction from the satellite towards observation point 2.

By providing parameters $[x_0, y_0]$, v, and θ, the positions of potential crossings and the angles with the antenna were investigated, resulting in the observed electric fields E_1 and E_2.

The initial position of the satellite $[x_0, y_0]$ was set by default to the coordinates $[-740, 0]$ (equivalent to $[\alpha, \beta]$). This location represents the left end in the X-axis direction and the center in the Y-axis direction on a plane with sides of 1500 m. Taking this as the initial position, the satellite moves in the positive direction along the X-axis relative to the circular potential structure centered at the point $[0, 0]$.

Furthermore, the sampling period was set to $T_{\text{s}} = 1$ for all cases.

3.3.2 Calculation results

Waveforms when the Satellite Center Passes through the Potential Center

First, the differences in observed waveforms due to the passage of a small potential were calculated. The velocity was set to $v = 2$ for all cases. For the satellite with the initial position $[x_0, y_0] = [\alpha, \beta]$ and antenna angle $\theta = 0$ degrees, the observed waveform is shown in Figure 3.5(1). In this case, no change in the electric field in the Y-axis direction is expected. Thus, a waveform similar to that of a one-dimensional Gaussian is anticipated. Indeed, from the waveform, it was evident that a symmetrical bipolar waveform was observed.

While maintaining the satellite's initial position at $[x_0, y_0] = [\alpha, \beta]$, the antenna angle θ was varied from 0 to 360 degrees in increments of 10 degrees. Except for $\theta = 90$ and 270 degrees, a bipolar type is maintained, but the amplitudes in the positive and negative directions are asymmetric.

The waveform observed when $\theta = 90$ degrees is shown in Figure 3.5(3). At this point, the antenna is aligned parallel to the Y-axis, and the coordinates of the two observation points are symmetrical with respect to the center of the potential. E_1 obtains an electric field in the Y-axis negative direction, and E_2 obtains an electric field in the Y-axis positive direction. In other words, considering the antenna polarities shown in Equation 3.5 and Equation 3.6, only positive electric field for E_1 and only negative electric field for E_2 are observed. Additionally, the shapes of the two waveforms are represented by one-dimensional Gaussians. A similar trend is observed when the antenna angle is 270 degrees.

For antenna angles θ other than 0, 90, 180, and 270 degrees, waveforms are observed that are bipolar and have different magnitudes of positive and negative electric field strengths. For example, the waveform at $\theta = 80$ degrees is shown in Figure 3.5(2). For E_1, the absolute value of the negative peak is larger than the positive peak value, and for E_2, the positive peak value is larger than the absolute value of the negative peak. In this case, at the two observation points, only the electric field in the antenna direction is observed. In other words, as the surrounding electric field direction approaches the antenna direction θ, the observed electric field becomes larger, and as the surrounding electric field direction approaches $\theta + 90$ degrees, the observed electric field tends to become smaller.

When E_1 takes the minimum value of the electric field, observation point 1 passes through the third quadrant on the plane. At this time, the difference between the surrounding electric field direction and the antenna direction is less than 45 degrees, and most of the surrounding electric field is observed. On the other hand, at the same time, observation point 2 passes through the second quadrant. The angle between the potential gradient and the antenna direction is in the range of 90 ± 45 degrees. Conversely, when observation point 2 passes through the maximum value, the difference between the surrounding electric field and the antenna direction is small, but at observation point 1, the difference is large. As a result, in E_1, the minimum value is larger in absolute value than the maximum value, and in E_2, the maximum value is larger than the minimum value.

Observation when the Potential Deviates from the Satellite Center

Next, consider the case where the direction of the satellite center deviates from the center of the potential. The initial position of the satellite was set to $[x_0, y_0] = [\alpha, \beta - 20]$, and calculations were performed. In this case, only negative electric field in the Y-axis direction is applied throughout the entire observation time. The velocity was set to $v = 2$ for all cases. In the case of the antenna angle $\theta = 0$ degrees, the observed waveform is shown in Figure 3.6(1). It can be seen that it is a symmetrical bipolar waveform. For $\theta = 0$ degrees, there is no observed change in the Y-axis direction of the electric potential, so the potential on the line $y = -20$ is observed. Since the potential on the line $y = -20$ is represented by a one-dimensional Gaussian, a symmetrical bipolar waveform is observed.

While maintaining the satellite's initial position, the antenna angle θ was varied from 0 to 360 degrees in increments of 10 degrees.

For angles θ other than 0, 90, 180, and 270 degrees, the observed waveforms are asymmetrical bipolar types. The waveform observed at $\theta = 80$ degrees is shown in Figure 3.6(2). At this time, both E_1 and E_2 have absolute values of the minimum peaks larger than the maximum peaks. Additionally, the negative region of the pulse width is wider than the positive region. In other words, in the waveform obtained in this case, which is asymmetrical bipolar, one of the regions separated by positive and negative has a larger electric field strength and pulse width at the peak compared to the other region. This characteristic is common to both observed waveforms, as represented by the second waveform in Figure 3.2 in actual Arase satellite interferometry observations.

Asymmetrical bipolar waveforms like the one shown in Figure 3.6(2) have a lower maximum correlation when taking the correlation between the two observed waveforms. For the symmetrical bipolar waveform shown in Figure 3.5(1), the maximum correlation of the cross-correlation coefficient is 1. On the other hand, for the waveform shown in Figure 3.6(2), the maximum cross-correlation coefficient is around 0.95. Even for waveforms obtained through numerical experiments, the maximum correlation is not 1, and it is expected that the maximum correlation in actual measured waveforms, including noise, will be even smaller. Therefore, among actual measured waveforms, waveforms with low correlation between E_{V1} and E_{V2} , represented by the second waveform in Figure 3.2, may be due to the passage of isolated potential structures with small spatial scales perpendicular to the magnetic field lines.

The waveform observed when $\theta = 90$ degrees is shown in Figure 3.6(3). Both observation points move in the region where $y \leq 0$. In other words, only negative electric field is applied in the Y-axis direction. In addition, since the antenna direction coincides with the Y-axis direction, no electric field in the X-axis direction is observed. In this case, considering the antenna polarities shown in Equation 3.5 and Equation 3.6, both E_1 and E_2 have only positive electric field. Moreover, the shapes of the two waveforms are represented by Gaussians.

From the results so far, it is evident that if it is a two-dimensional Gaussian, both the symmetrical bipolar waveform shown in Figure 3.3 and the asymmetrical bipolar waveform shown in Figure 3.4 can be observed. The former is observed when the antenna angle coincides with the direction of potential passage, and the latter is observed when the antenna angle has an angle other than 90 and 270 degrees with respect to the direction of potential passage and does not pass through the center of the potential. It is trivial that the proportion of cases where the former condition is satisfied is smaller than the proportion of cases where the latter condition is satisfied. The observation of many asymmetrical bipolar waveforms is matched with the results of this numerical experiment.

This suggests that the isolated potential structures observed by the Arase satellite can be

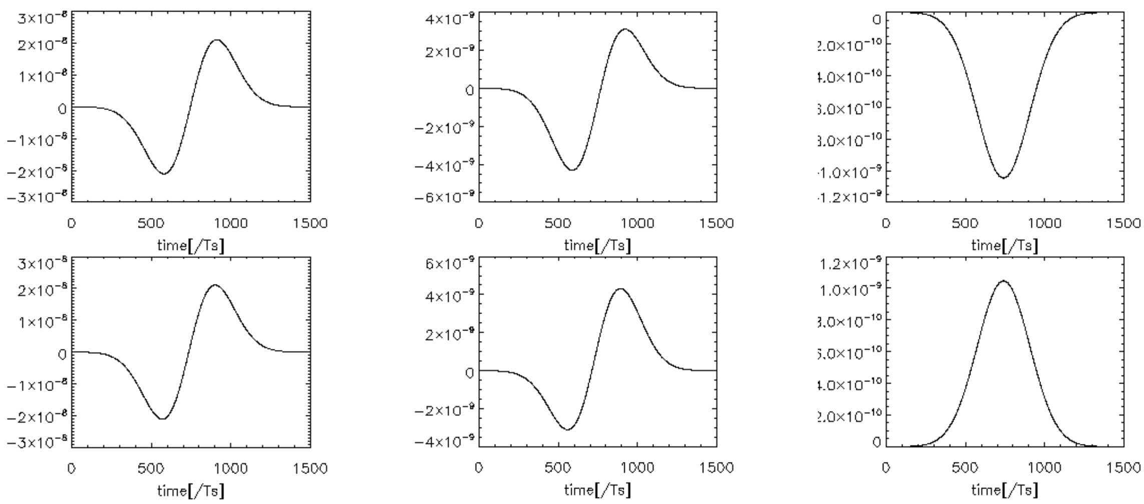

(1)Observed waveform for $v = 2$, $[x_0, y_0] = [\alpha, \beta]$, $\theta = 0$ degrees

(2)Observed waveform for $v = 2$, $[x_0, y_0] = [\alpha, \beta]$, $\theta = 80$ degrees

(1)Observed waveform for $v = 2$, $[x_0, y_0] = [\alpha, \beta]$, $\theta = 90$ degrees

Figure 3.5: Observed waveform when the satellite center overlaps the center of the potential structure

represented by a two-dimensional Gaussian.

3.4 Derivation of isolated potential polarity

we describe the analysis method for determining the polarity of the potential. In past satellite observations, such as those by the GEOTAIL, Polar, and RBSP satellites, the origin of the potential—whether it was electron-derived or ion-derived—was primarily considered based on scales like relative velocity and waveform shape. For instance, in the case of the Polar satellite, a group of waveforms with different time scales were observed in a single observation. The shorter time-scale waveforms were considered to be electron-derived potentials, while the longer time-scale ones were thought to be ion-derived potentials[37, 38]. In the GEOTAIL satellite, the direction of propagation was also studied assuming that the isolated potential was derived from electrons[43]. However, the plasma's velocity depends on its energy and the surrounding magnetic field strength, allowing only relative consideration. To determine the polarity of the potential based on the change from positive to negative in waveform using dipole

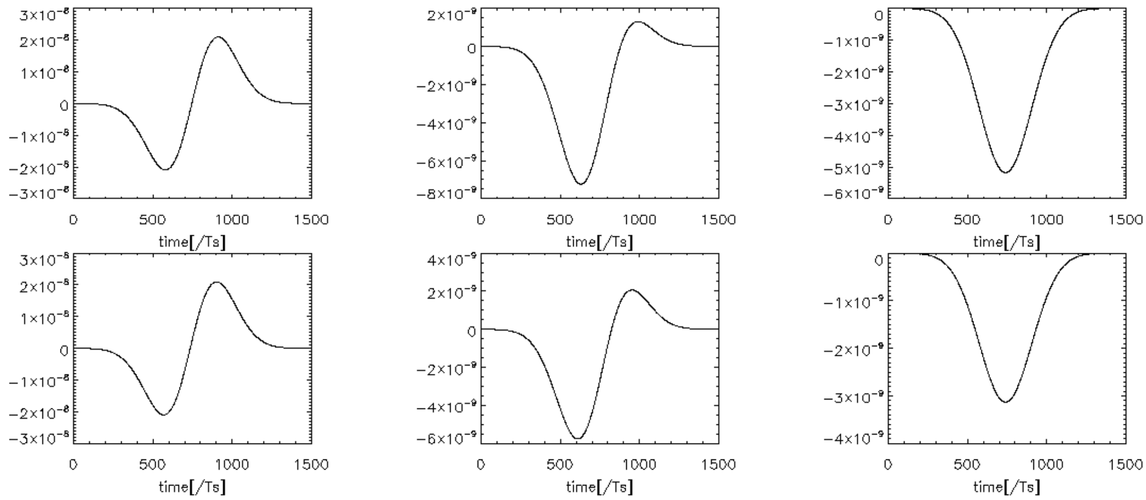

(1)Observed waveform for $v = 2$, $[x_0, y_0] = [\alpha, \beta - 20]$, $\theta = 0$ degrees

(2)Observed waveform for $v = 2$, $[x_0, y_0] = [\alpha, \beta - 20]$, $\theta = 80$ degrees

(3)Observed waveform for $v = 2$, $[x_0, y_0] = [\alpha, \beta - 20]$, $\theta = 90$ degrees

Figure 3.6: Observation when the satellite center is off the center of potential structure

observations, one must assume the direction of passage, and there are no examples of determining the polarity from the observation itself. However, by using the results of monopole mode observations, it is possible to understand the direction of passage of the potential. This could enable a more certain determination of polarity. In this section, we determine the polarity of the potential from the analysis of monopole observations by the Arase satellite.

3.4.1 Method

In monopole observations, the polarity of the potential can be determined by considering the waveform shape, the polarity of the antenna, and the direction of the potential's passage relative to the antenna. Suppose a bipolar waveform that changes from positive to negative is observed on antennas V1 and V2. If V1 detects the waveform earlier than V2, it can be inferred that the potential moves from V1 to V2. In the Arase satellite, the polarity of the antennas in monopole observation mode is set so that the direction toward the satellite body is positive for antenna V1, and the direction away from the satellite body is positive for antenna V2. Thus, in the waveform being considered, the electric field is observed initially from V1 to V2 and then from V2 to V1. Such a change in the direction of the electric field, when considering the direction of passage relative to the antennas, occurs if a potential structure with positive polarity passes through. A positive-to-negative changing electric field waveform can also be observed when a potential with negative polarity passes, but in the case of the Arase satellite, this would occur if the potential passed from V2 to V1. In this manner, by using waveforms obtained from monopole observations, it is possible to derive the polarity of the potential.

3.4.2 Results

Determination of Potential Polarity for the Data on October 7, 2018, at 13:00 The polarity of the potential was determined for the data on October 7, 2018, at 13:00. From the 16 sample waveforms obtained in Section 3.1.2, those with a defined sign for the time difference were selected. Specifically, the analysis focused on 6 samples with determined time differences in Section 3.1.2. Additionally, to increase the number of samples, the selection criteria for the waveforms were reconsidered. While previously only waveforms with a correlation of 0.75 or higher between E_{V1} and E_{V2} were used, Section 3.1.3 demonstrated that bipolar waveforms with asymmetric positive and negative peaks could have lower correlations. Therefore, bipolar waveforms from the monopole observation data on October 7, 2018, with a cross-correlation coefficient of 0.6 or higher, were also included. Among these, 4 samples had time differences determined by the method using cross-correlation. These 4 samples were designated as sample numbers 17 to 20. The polarity of the potential obtained for each sample is shown in Table 3.4.

Among the 6 waveforms with a maximum correlation of 0.75 or higher, positive and negative potentials were observed in roughly equal proportions. In contrast, for the 4 waveforms with a maximum correlation of 0.6 or higher, more positive potentials were observed than negative ones. It has been generally thought that positive potentials are present in the magnetosphere. This assumption is based on two points. First, electric field waveforms observed by satellites such as GEOTAIL and FAST have short time scales, suggesting they are of electron origin. Second, computer simulations have demonstrated the formation mechanisms of positive potentials. However, the current results suggest that both positive and negative potentials can be observed within the inner magnetosphere. That said, only 10 samples had their potential polarity determined, which is insufficient to statistically indicate the distribution trends of potential polarity along the Arase satellite's orbit. Furthermore, the current analysis estimated the potential polarity based on the one-dimensional electric field changes in the satellite's direction of travel. However, since many of the analyzed waveforms are asymmetric ESW, considering two-dimensional isolated potentials, including the direction perpendicular to the background magnetic field, is necessary. Thus, if two-dimensional simultaneous interferometry observations could be conducted, it is expected that the potential distribution could be estimated more accurately.

Table 3.4: Results of potential polarity determination

Sample Number	Obtained Time Difference	Electric Field Change Direction	Potential Polarity
1	plus	positive to negative	positive
2	plus	negative to positive	negative
4	plus	positive to negative	positive
9	plus	positive to negative	negative
13	minus	negative to positive	positive
16	plus	negative to positive	negative
17	plus	positive to negative	positive
18	plus	positive to negative	positive
19	plus	positive to negative	positive
20	plus	negative to positive	negative

Chapter 4

Application in electromagnetic waves: Whistler-mode chorus waves

4.1 Event analysis

The chorus wave observed on September 1, 2019 from 5:00 p.m. to 6:00 p.m. is shown in Figure 4.1. Figure 4.1 shows the spectrum of electric and magnetic fields observed by the Arase satellite OFA. The red line in the figure is the electron cyclotron frequency and the white line is the half value of the electron cyclotron frequency. Electromagnetic waves are observed in the upper and lower frequency bands around $0.5 f_{\mathrm{ce}}$, respectively.

Interferometry observations were performed during the 1-minute period beginning at 17:33:20 of this chorus waveform. The results of the analysis of the interferometry observation waveforms are shown in Figure 4.2. Figure 4.2(a) shows the spectrum of the electric field observed by antenna V1 and Figure 4.2(b) shows the spectrum of the magnetic field observed in the beta direction of the MSC. Figure 4.2(c) shows the coherence between E_{V1} and E_{V2} calculated by Equation 4.1.

$$Coh(f) = \sqrt{\frac{|\langle W_1(f) W_2^*(f) \rangle|^2}{\langle |W_1| \rangle \langle |W_2| \rangle}} \tag{4.1}$$

Figure 4.2(d) shows the phase difference between E_{V1} and E_{V2} . Calculations were performed only for parts with coherence greater than 0.9 and field intensity greater than 7×10^{-3} mV/m. Figure 4.2(e) represents the angle between the background magnetic field projected onto the spin plane and the direction of antenna V1. This parameter is denoted as γ_B. Figure 4.2(f) represents the elevation angle of the background magnetic field with respect to the spin plane.

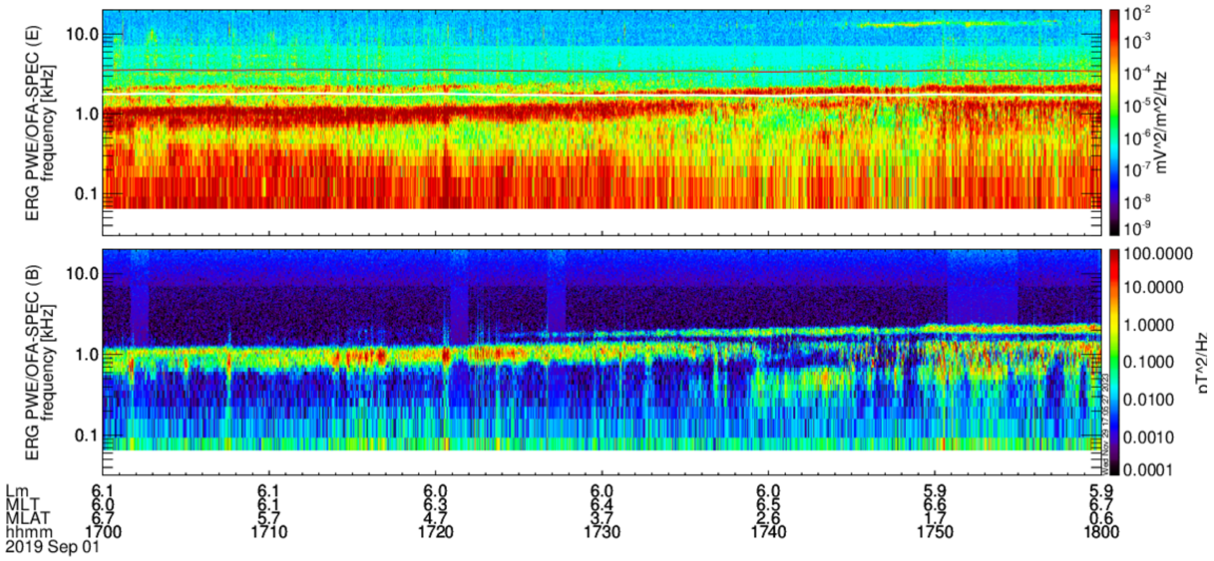

Figure 4.1: The electric field and magnetic field spectra of chorus waves observed by the Arase satellite OFA. Red line represents the electron cyclotron frequency and white line represents the half of the electron cyclotron frequency

It is shown that the phase difference is spin-dependent. To understand the dependence of the phase difference on γ_B, we evaluated average profiles of the phase difference as a function of γ_B. Figure 4.3 shows the average of the phase difference was calculated every 5 degrees of γ_B. Error bars indicate standard deviation.

The phase difference remains almost small and shows a very large scatter at the spin angle of 0 degrees and 180 degrees. This is because at a spin angle of ± 90 degrees, the antenna is perpendicular to the projected background magnetic field. The wave vector direction is considered to exist in the vertical plane to the antenna. In this case, the electric field oscillates in a direction parallel to the antenna. Thus, it is observed to have a minimum phase difference and a maximum intensity. Conversely, at 0 and 180 degrees, the projected background magnetic field is parallel to the antenna. In this case, the wave vector has a component parallel to the antenna. On the other hand, the electric field oscillate perpendicular to the background magnetic field. Since the spin axis of the Arase satellite is almost oriented toward the sun, the elevation angle of the background magnetic field to the spin plane is about 10 degrees. Thus, the field oscillations are almost perpendicular to the spin plane, and the observed field intensity is at most 0.17 times the maximum intensity, which is very small. At spin angles of 0 and 180 degrees, the Signal Noise ratio deteriorates and the phase difference dispersion worsens.

The phase velocity of chorus waves is known to be very fast, generally on the order of

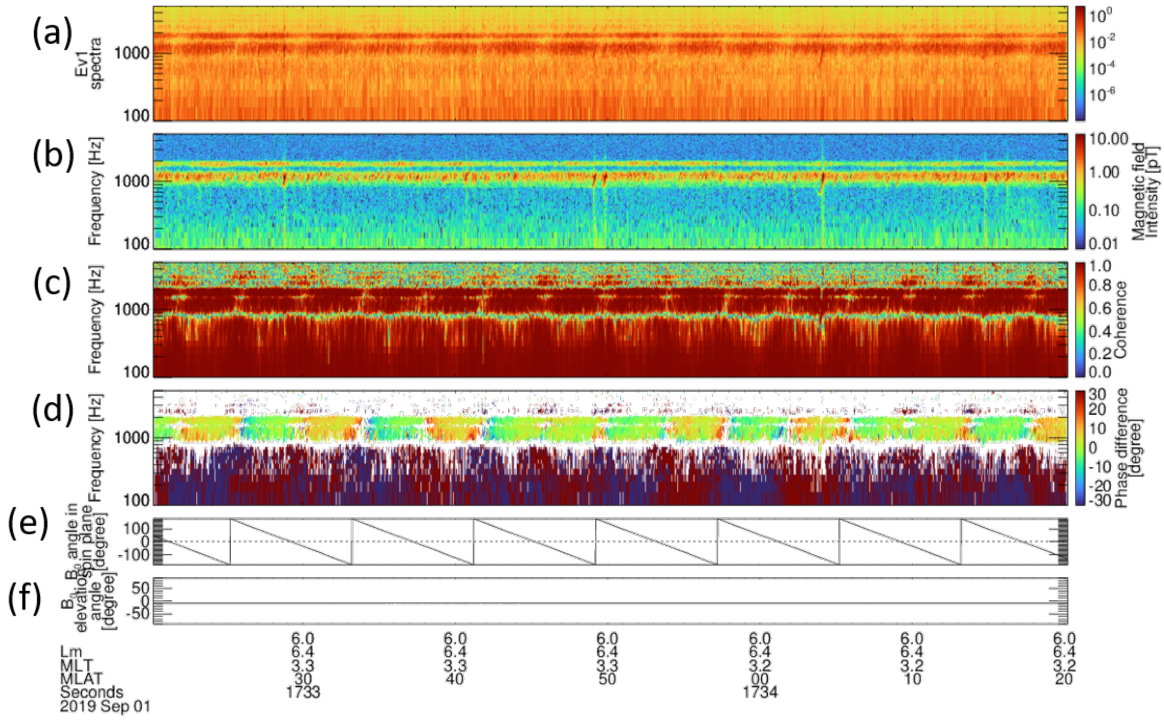

Figure 4.2: The phase difference of this chorus wave calculated by the method described in Chapter 2 (a) Spectrum of the electric field observed by antenna V1 (b) Spectrum of the magnetic field observed in the beta direction of the MSC (c) Coherence between E_{V1} and E_{V2} (d) Phase difference between E_{V1} and E_{V2} (e) Angle between the background magnetic field projected onto the spin plane and the direction of antenna V1 (f) Elevation angle of the background magnetic field with respect to the spin plane

10^7 m/s, so the phase difference is considered to be about 0 degrees even at the spin angle of 0 degrees and 180 degrees. On the other hand, the sampling frequency of the Arase satellite PWE is almost 65 kHz, and when a chorus of 3000 Hz is observed, the resolution of the phase difference will be about 5 degrees. In reality, smaller phase difference can be calculated by using the Fourier transform method, but it is difficult to accurately calculate the phase velocity by interferometry observation.

4.2 Numerical calculation

We show a numerical model for the Chorus waves observed by the interferometry observation mode of the Arase satellite. The electric field representing the Chorus wave is expressed by the following equation[44].

$$E(\boldsymbol{r}_{B1}, t) = A\cos(\boldsymbol{k}\cdot\boldsymbol{r}_{B1} - \omega t), \tag{4.2}$$

$$\boldsymbol{k} = k(\cos\psi\cos\phi, \cos\psi\sin\phi, \sin\psi) \tag{4.3}$$

Since the source region of chorus waves is significantly larger than the distance between observation points[45], it was assumed as a plane wave. In this event, only rising tone chorus was targeted for observation. It is known that the wave normal angle of rising tone chorus is mostly below 10 persent, and the majority are below 20 persent[46, 47]. Therefore, in this study, the wave vector direction was assumed to be aligned with the background magnetic field. This electric field oscillation is in the plane perpendicular to the background magnetic field direction. The schematic diagram is shown in Figure 4.4.

$$A = \sqrt{1 - ip^2}, \tag{4.4}$$

where ip means the inner product of antenna direction vector and background field direction vector. Since the antenna direction vector is represented by $(\cos\gamma, \sin\gamma, 0)$ and the background magnetic field direction vector by $(\sin\psi\cos\phi, \sin\psi\sin\phi, \cos\psi)$, ip is expressed as

$$ip = \cos\gamma\sin\psi\cos\phi + \sin\gamma\sin\psi\sin\phi. \tag{4.5}$$

Since the two observation points are represented by $(0.5l\cos\gamma, 0.5l\sin\gamma, 0)$ and $(-0.5l\cos\gamma, -0.5l\sin\gamma, 0)$. The calculated waveform of E_{V1} is shown in Figure 4.5 (a) and the phase difference in Figure 4.5 (b).

In this experiment, we successfully replicated the relationship between phase difference and amplitude. At this time, the maximum phase difference within one spin was approximately 0.2 degrees, and it is considered challenging to observe the phase difference of chorus waves due to noise occurring during observations.

Next, we consider the upper and lower limits of observable phase velocities by the Arase satellite. We contemplate waves that change phase velocity at the same frequency. The observed lower limit of phase velocity is determined by the condition that the maximum observed phase difference is less than 2π. If the phase difference becomes 2π or more, it becomes $\theta \pm 2n\pi$, making it impossible to determine the true phase difference from the observation. Therefore, the observed lower limit of phase velocity is $v_{\mathrm{ph\_min}} = 2\pi L_f/2\pi$ and $v_{\mathrm{ph\_min}} = L_f$.

On the other hand, the observed upper limit depends on the smallest value of the phase difference that the satellite can observe. Therefore, the minimum value of the phase difference is theoretically expressed as $\theta_{\mathrm{min}} = 2\pi f / f_s$. This implies that the observed upper limit is $v_{\mathrm{ph\_max}} = 2\pi L_f / \theta_{\mathrm{min}} = L_f f_s$.

As a result, we found that the maximum observable phase velocity by the Arase satellite is approximately 10^6 m/s.

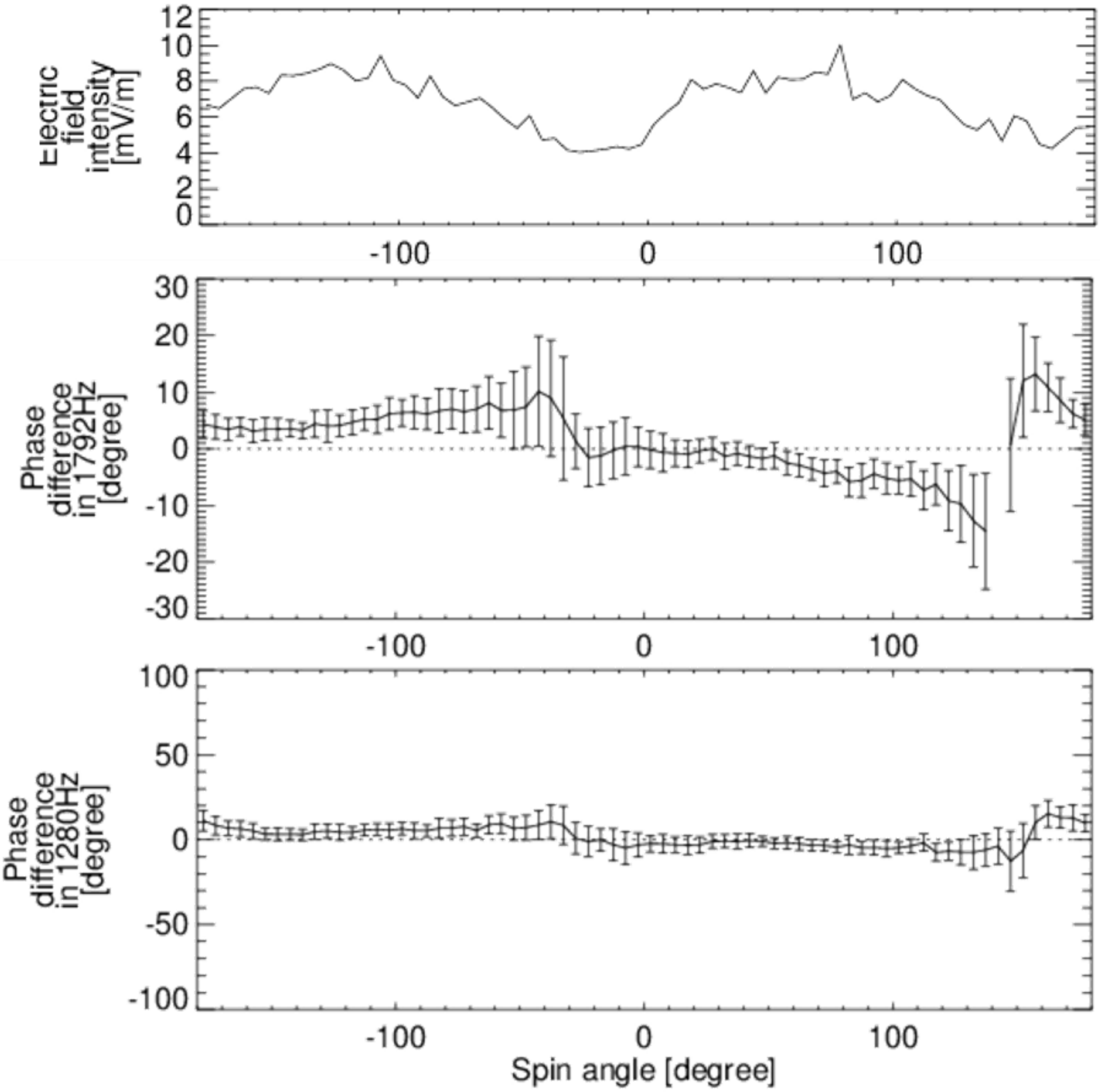

Figure 4.3: Electric field intensity at the frequency with the maximum intensity and average profiles of the phase difference as a function of γ_B.

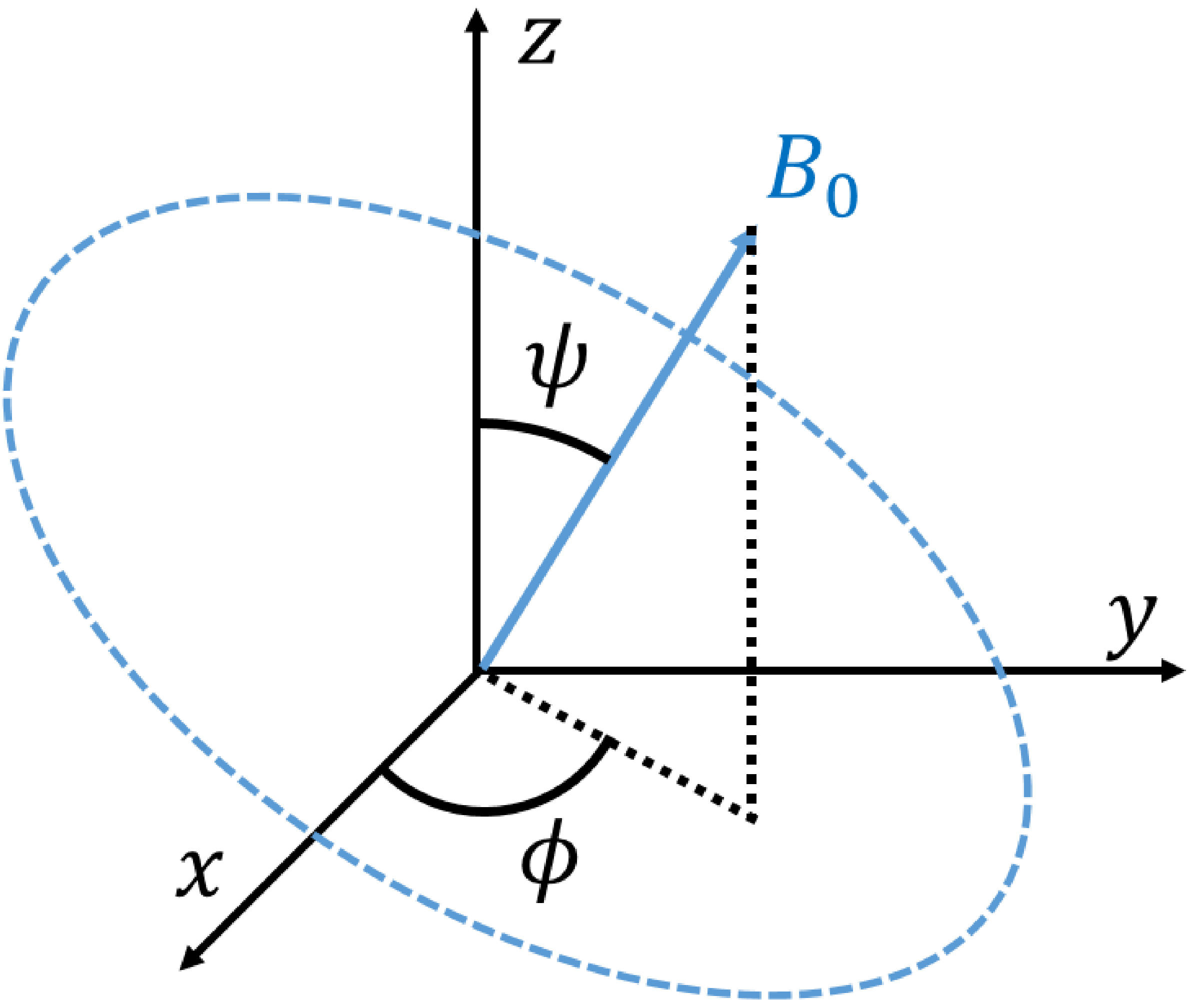

Figure 4.4: The schematic diagram of numerical calculation

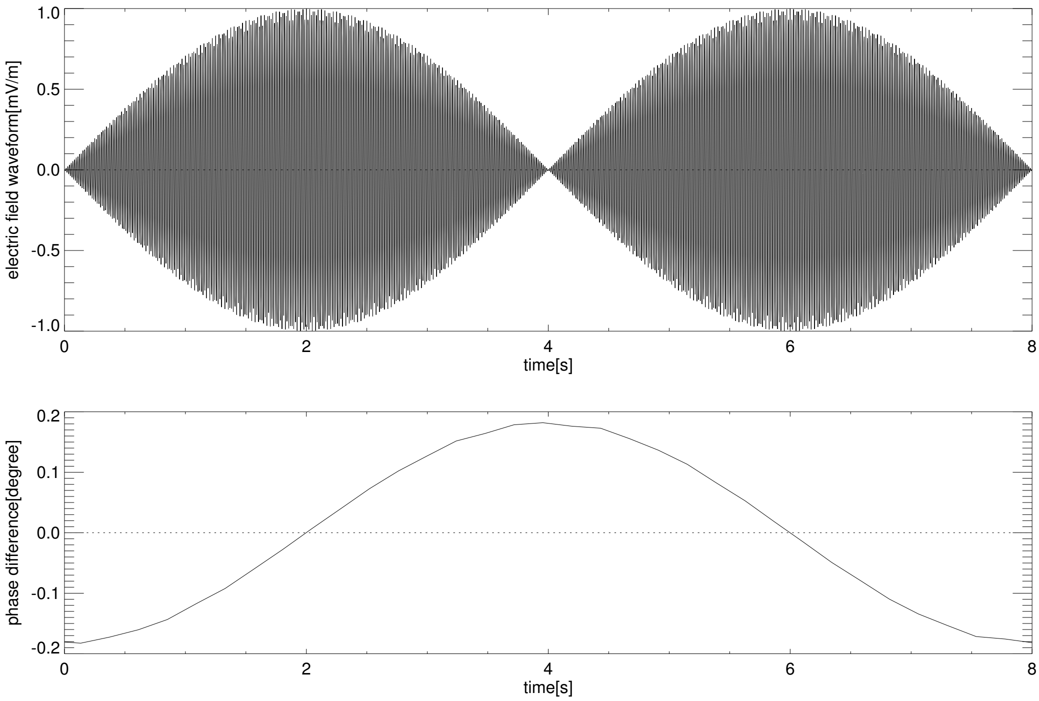

Figure 4.5: (a)Outline of the observed model wave of Chorus wave in the spin period (b)Calculated phase difference

Chapter 5

Application in electrostatic waves: Electron cyclotron harmonic waves

5.1 Introduction

Electrostatic Electron Cyclotron Harmonic (ECH) waves are one type of plasma waves observed in the magnetosphere. These waves exhibit frequency harmonic structures close to $(n+1/2)$ times of the electron cyclotron frequency, f_{ce}. Strong emissions are also observed near the Upper Hybrid Resonance (UHR) frequency. ECH waves are electrostatic in nature, with a wave vector nearly perpendicular to the ambient magnetic field. The electric field oscillation of ECH waves is parallel to the wave vector due to their electrostatic properties. ECH waves were first discovered by the OGO-5 satellite [20]. They are excited by a loss cone distribution of hot electrons coexisting with a cold core electron population [48]. ECH waves have been observed by various satellites in the Earth's magnetosphere, and are frequently observed near the magnetic equator[49, 22]. ECH waves are also observed in the magnetosphere of Jupiter and Saturn [23, and references therein].

ECH waves have been reported to have large amplitudes on the order of approximately 10 mV/m [20, 25], suggesting their significant impact on the plasma environment. ECH waves are known to cause electron pitch angle scattering, leading to diffuse aurora [19, 50, 51]. THEMIS observations have shown evidence of pitch angle scattering of several keV-level electrons due to ECH waves [26, 27]. Simultaneous observations with the Arase satellite and ground-based optical imagers have revealed a correlation between the intensity of ECH waves and pulsating auroras, suggesting the possibility that electrons scattered by ECH waves in the loss cone contribute to the generation of diffuse auroras [28].

ECH waves have been analyzed for diagnosing plasma properties. Hubbard and Birmingham [52] classified the frequency structure of ECH waves observed by the ISEE satellite into several categories. In order to understand the excitation conditions of ECH waves in each category, calculations of the linear growth rate were also performed by varying the plasma properties. Hubbard and Birmingham [52] proposed that the frequency structure of ECH waves can be used to diagnose the density and temperature of cold electrons, and this method was utilized in Hubbard et al. [53]. Moncuquet et al. [24] experimentally derived the dispersion relation of ECH waves through a comparison between spin modulation of the observed waves by the Ulysses spacecraft and theoretically predicted waves. The experimental dispersion curve was fitted to the theoretical curve, enabling the determination of the density and temperature of cold electrons.

By using interferometry techniques to estimate the wavelength of waves from satellite measurements, it is possible to experimentally derive the dispersion relation [e.g. 54]. The Arase satellite Miyoshi et al. [55] has the capability to perform interferometry observations, allowing for the determination of the dispersion relation of observed ECH waves. To evaluate the wavelength of waves from the interferometry observation, it is essential to derive the phase difference of the waves from the observation. In this study, events in which ECH waves are observed during interferometric measurements by the Arase satellite are investigated. This study shows that the phase difference of ECH waves obtained from the interferometry observation by the Arase satellite can be categorized into two groups, which are followed by simple numerical experiments to explain the phase difference of ECH waves observed by the Arase satellite.

5.2 Event analysis

The analysis was performed for the ECH waves observed near 00:00 UT on September 8, 2019. An overview of the electric field spectra observed by OFA is shown in Figure 5.1. The electron cyclotron frequency f_{ce} calculated using the MGF background field data is indicated by the red line in the figure, and its half and integer multiples are indicated by the white lines. There is a harmonic structure with peaks between integer multiples in the frequency range above f_{ce}. The burst mode operation of interferometry observations was performed continuously for 60 seconds starting at 00:00:10 UT. The time of operation of interferometry observation is arrowed in Figure 5.1. The magnetic local time at this time is 5.7 MLT, the radial distance is 5.9 Re, and the magnetic latitude is -0.8 degrees. Figure 5.1 shows that there are multiple peaks in the electric field spectrum in the frequency band between f_{ce} and $2f_{\mathrm{ce}}$, especially around 00:00 UT on September 8.

The waveforms from 00:00:40.647 UT during 1 ms are shown in Figure 5.2. At this time, the elevation angle from the spin plane in the direction of the background magnetic field was 4 degrees, and the angle that the background magnetic field projected onto the spin plane made with the antenna E_{V1} was -85 degrees. At this time, the electric field waveforms with an amplitude of about 40 mV/m were seen in both E_{V1} and E_{V2} . The wave vector direction, which coincides with the direction of oscillation of the electric field, is considered to have a component parallel to the antenna. Figure 5.2 shows bandpass-filtered electric field waveforms in the harmonic bands of the ECH wave. The black and red line in each figure shows the bandpass-filtered E_{V1} and E_{V2} waveform, respectively. It can be seen that the two lines do not overlap and a phase difference is obtained. The phase difference was calculated by Fourier transform using 1024 points so that the peaks of these frequencies are visible. The frequency resolution is 64 Hz. The Hanning window was used to perform the Fourier transform, which is expressed as

$$w(k) = \alpha - (1-\alpha)\cos\left(\frac{2\pi k}{N}\right) \quad (0 \leq k \leq N-1). \tag{5.1}$$

We used $\alpha = 0.5$. The time used was approximately 15.6 ms centered at 00:00:40.647 UT. The frequency and amplitude, and frequency and phase difference are shown in Figure 5.3. The vertical axis is normalized by f_{ce}. The phase difference at each frequency is calculated if the wave amplitude in the band exceeds 0.005 mV/m to remove the fluctuations of the phase difference caused by the low intensity waves and noises. From the left panel of Figure 5.3, we can see that the intensity peaks in the harmonic bands of the ECH waves are greater than 0.1 mV/m. Among the intensity peaks, low intensity waves or noises are present with the intensity below 0.005 mV/m. Thus we selected the threshold value of 0.005 mV/m to discriminate the ECH waves and noises. Figure 5.3 shows that multiple peaks are included between integer multiples of the cyclotron frequency. The multiple peaks at f_{ce} to $2f_{\mathrm{ce}}$ were remarkable, but the other frequency bands also contain multiple peaks with gaps rather than a single peak.

Figure 5.3 shows that the signs of the phase difference may be different even though the frequencies are close. For example, at 4672 Hz (1.052 f_{ce}), the phase difference was 20.08 degrees, and at 5312 Hz (1.196 f_{ce}), the phase difference was -13.01 degrees. Since these phase differences are expressed in the range of -180 degrees to 180 degrees, the actual phase differences are shown as follows:

$$\Delta\theta = \Delta\theta_{\mathrm{observed}} + 2n\pi \tag{5.2}$$

where n is an integer, $\Delta\theta$ is the true phase difference between the two observation points, and $\Delta\theta_{\mathrm{observed}}$ is the phase difference calculated from the observed waveform. There are other frequency bands with positive and negative phase differences at close frequencies. At 15040 Hz ($3.39 f_{\mathrm{ce}}$) the phase difference is -3.58 degrees and E_{V1} is later than E_{V2} , while at 14848 Hz

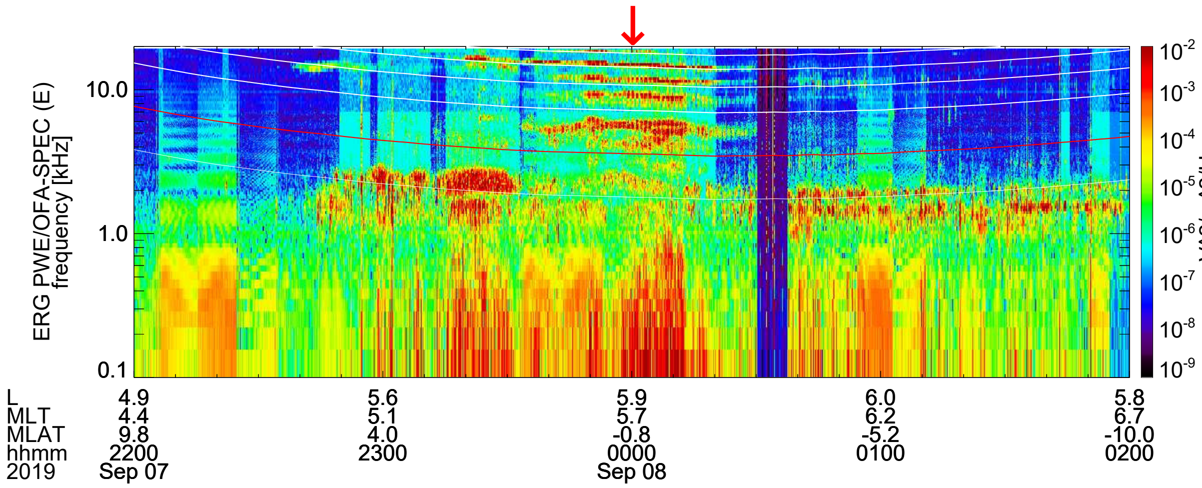

Figure 5.1: Overview of the electric field spectrum observed by OFA from 22:00 UT on September 7, 2019, to 2:00 UT on September 8, 2019

($3.34 f_{ce}$) the phase difference is 0.270 degrees and E_{V1} is earlier than E_{V2} . As shown in equation (4), the true phase difference has ambiguity, but it is difficult to argue that the phase velocity differs significantly at close frequencies, considering that they follow the same dispersion curve. Therefore, this difference in phase difference may be due to a difference in the direction of the wave vector. In this case, it is suggested that the wave vector may be different for each frequency. There may be multiple small-scale source regions distributed around the Arase satellite. Another cause may be the mixing of multiple ECH waves with different peak frequencies. In the harmonic structure shown in Figure 5.1, the fundamental appears to have a single peak in the early part of the event before 00:00 UT on September 8, and peaks in multiple frequency bands with gaps in between in the latter half of the event. It is quite difficult to determine from the spectral changes whether the ECH waves seen in this event are a single wave or a mixture of multiple ECH waves.

Calculation of the phase difference for each of these peaks indicated that the phase differences were different even at close frequencies. Even though the phase differences obtained from the observations have an ambiguity of $2n\pi$, it is difficult to argue that the phase velocity change that much at close frequencies. It is thereby possible that the wave vector direction is different at each frequency.

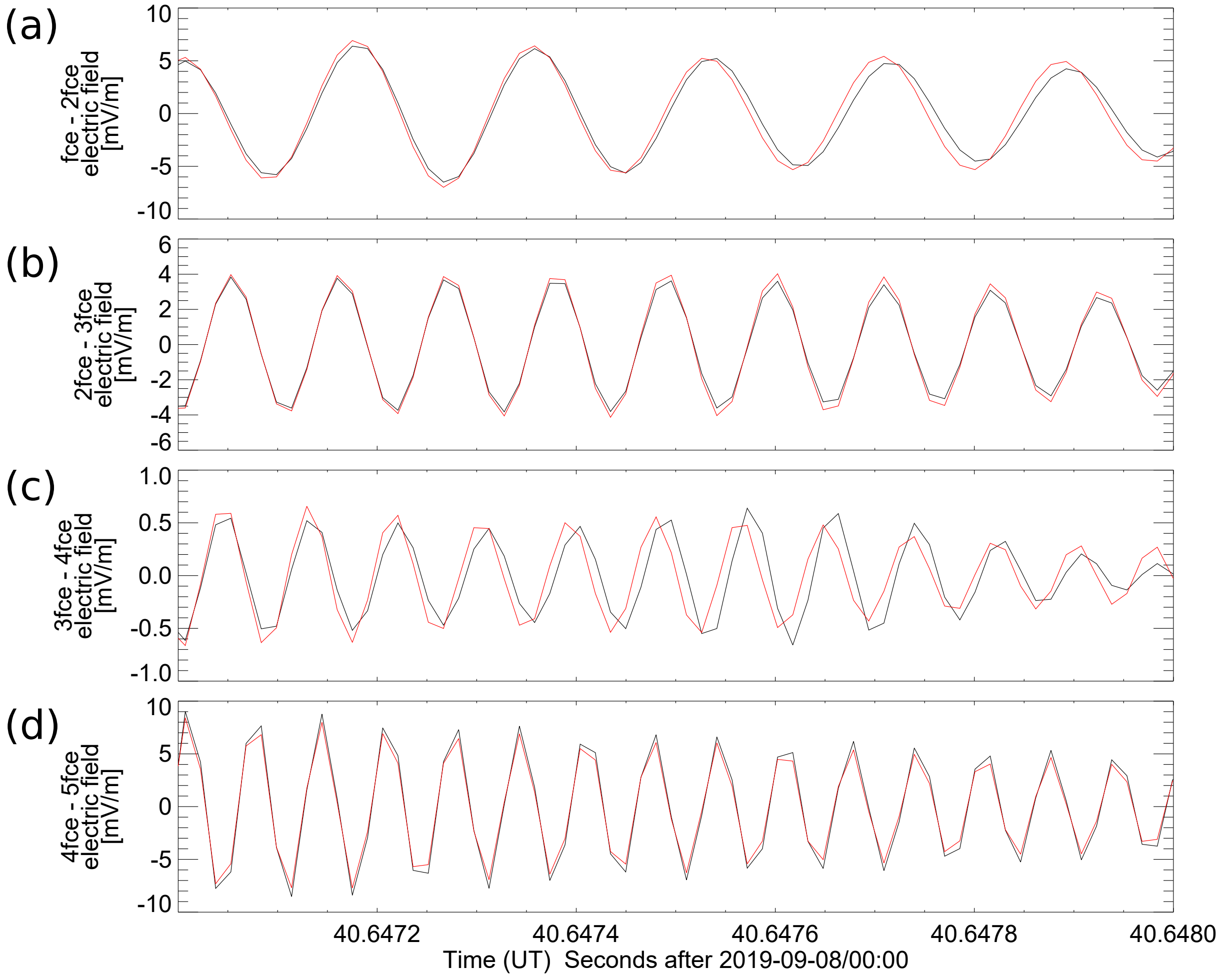

Figure 5.2: Electric field waveforms observed from 00:00:40.647 UT for 1 ms, which are bandpass-filtered in the frequency of (a)f_{ce} to $2f_{ce}$, (b)$2f_{ce}$ to $3f_{ce}$, (c)$3f_{ce}$ to $4f_{ce}$, and (d)$4f_{ce}$ to $5f_{ce}$, respectively

5.3 Numerical calculation

We show three examples of ECH waves observed by the interferometry observation mode of the Arase satellite. The first event is shown in Figure 5.4, which starts at 00:00:10 on 8 September 2019 with a duration of 60 seconds. The Arase satellite was located at a radial distance of 5.9 Re, a magnetic latitude of -0.8 degrees, and a magnetic local time of 5.7 MLT. The f_{ce} of this event is 3585 Hz. Figure 5.4(a) and (b) show frequency-time spectrograms computed from electric and magnetic field waveforms observed by antenna V1 and one of the magnetic search coil sensors, B_β, respectively. The multiple harmonic emissions are only seen in the spectrogram of the electric field, which corresponds to the ECH waves. Electromagnetic waves, which appear below the electron gyrofrequency shown in Figure 5.4(a), correspond to whistler mode waves. Figure 5.4(c) represents the coherence between E_{V1} and E_{V2}, which is calculated using the following equation:

$$Coh(f) = \sqrt{\frac{|\langle W_1(f) W_2^*(f) \rangle|^2}{\langle |W_1| \rangle \langle |W_2| \rangle}} \tag{5.3}$$

The ensemble average is calculated using a total of 3 and 3 points in the time and frequency domain, respectively. The coherence is used as a confidence indicator of results obtained from the interferometry technique. The coherence threshold of 0.9 is used to discriminate valid signals from unreliable ones. In addition, we removed data points with spectral intensities less than 2.0×10^{-3} mV/m from the analysis. The frequency-time spectrogram of the phase differences is shown in Figure 5.4(d). It can be seen that the phase difference is larger at low frequencies and smaller at high frequencies in each frequency band of the harmonic structure of the ECH waves. This tendency is clear, especially in the frequency range from f_{ce} to $2f_{\mathrm{ce}}$. Figure 5.4(e) shows the angle γ_B between the V1 antenna and the ambient magnetic field projected on the spin plane and Figure 5.4(f) shows the elevation angle of the background magnetic field from the spin plane. It is found that the phase difference between the two antennas is maximized at the timing of γ_B close to ± 90 degrees, which corresponds to the timing that the amplitude of the ECH waves is maximized during the satellite spin. These analyses are applied to the other events.

To understand the dependence of the phase difference on γ_B in detail, average profiles of the phase difference as a function of γ_B are evaluated using the data shown in Figure 5.4(d). The wave amplitude of ECH waves as a function of frequency is averaged over the time interval shown in Figure 5.4 and the frequency bin with the maximum amplitude in each harmonic band of the ECH waves is chosen to analyze the γ_B dependence of the phase difference. For the event shown in Figure 5.4, five frequency bins of 5696 Hz, 9024 Hz, 11776 Hz, 15040 Hz, and 18304 Hz are selected.

The average profiles of the phase differences at the selected frequency bands are shown in Figure 5.5 together with standard deviations. The averages and standard deviations are computed every 5 degrees of γ_B. It is found that the phase difference tends to have large deviations when γ_B is close to 0 degrees and ± 180 degrees, and the phase difference formed two peaks with γ_B around ± 90 degrees.

In an ideal case of ECH wave observation, when γ_B is 0 degrees and ± 180 degrees, the antenna is nearly perpendicular to both the wave vector and electric field of ECH waves. Since the electric field is hardly picked up by the antennas in this configuration, it is expected that the phase difference computed in this case would be dominated by noises and does not represent the true phase difference of ECH waves. When γ_B is ± 90 degrees, the antennas lie in the plane where the electric field fluctuations are present. This allows us to obtain the phase difference with maximum intensity and good signal-to-noise ratio. It is also important to note that the distance between wavefronts measured by two antennas can be the largest when γ_B is ± 90 degrees, which results in a large phase difference between antenna V1 and V2.

The second event is shown in Figure 5.6, which starts at 23:52:35 on 7 September 2019 with a duration of 60 seconds. The Arase satellite was located at a radial distance of 5.9 Re, a magnetic latitude of -0.2 degrees, and a magnetic local time of 5.6 MLT. The f_{ce} of this event is 3633 Hz. The analysis method applied to the first event is used for the second event. Applying the same procedure as in the analysis of the first event, the average profile of the phase difference as a function of γ_B was obtained at frequencies of 5632 Hz, 9344 Hz, 11712 Hz, 15360 Hz and 18688 Hz. The results are shown in Figure 5.7. At 9344 Hz, 11712 Hz, 15360 Hz, and 18688 Hz, the phase difference is close to zero and independent of γ_B. On the other hand, at the 5632 Hz, the same sinusoidal shape as shown in Figure 5.5 was observed.

The third event is shown in Figure 5.8, which starts at 23:29:50 on 7 September 2019 with a duration of 60 seconds. The Arase satellite was located at a radial distance of 5.8 Re, a magnetic latitude of 1.5 degrees, and a magnetic local time of 5.4 MLT. The f_{ce} of this event is 3823 Hz. The analysis method applied to the first event is used for the third event. Applying the same procedure as in the analysis of the first event, the average profile of the phase difference as a function of γ_B was obtained at frequencies of 4096 Hz, 9856 Hz, 14592 Hz, 15872 Hz and 22848 Hz. The results are shown in Figure 5.9. There is no intense signal in the fundamental frequency band, and waves are observed in the higher frequency bands. In all frequency bands where waves are observed, the phase difference is close to zero regardless of γ_B.

From the event studies of the phase difference of the ECH waves computed from the interferometry observation performed by the Arase satellite, two patterns are seen in the dependence of the averaged phase difference on γ_B. To understand the generality of the patterns, we performed a statistical analysis of the γ_B dependence of the averaged phase difference of ECH waves using the interferometry observation by the Arase satellite from August to September 2019. During this period, ECH waves were the target of the interferometry observation by the Arase satellite. A total of 160 interferometry observation events were acquired during the period.

We first selected the interferometry observation events during which ECH waves were observed. The phase difference of ECH waves between two antennas is analyzed by using the same method as shown in the previous section. The average profiles of phase difference as a function of γ_B are computed in each harmonic band of the ECH waves. Of the 160 events, we find 84 interferometry observations of ECH waves.

We classified the 84 observed ECH events into four types based on their trends. Of the observed ECH events, 47 events show the γ_B dependence of the averaged phase difference similar to the event shown in Figure 5.5. There are 24 events with no γ_B dependence of the phase differences in the entire ECH frequency band. In these cases, the calcurated phase differences are close to zero. Most events with this characteristic have waves in the high frequency band rather than the fundermental frequency band, as shown in Figure 5.9. 9 events show a mixture of the ECH frequency bands with γ_B-dependent phase difference and the phase difference close to zero in all γ_B as shown in Figure 5.7. At last, there are 4 events in which the phase difference fluctuates and shows no trend related to γ_B.

We construct a simple model to understand the results from the interferometry observation performed by the Arase satellite. In the model, the properties of ECH waves are considered to construct model waves.

Numerical calculations are performed in the Despun Sun sector Inertia(DSI) coordinate system used on the Arase satellite. The Z-axis of the DSI coordinate system is parallel to the spin axis, and the X-axis is defined with respect to the sun direction determined by the sun sensor onboard the Arase satellite. The Y-axis in DSI is defined to complete the right-hand coordinate system. In the DSI coordinate system, the two antennas V1 and V2 rotate in the XY plane with a period of 8 seconds according to the satellite spin. As shown in Figure 5.10, γ is the angle between the antenna V1 and the DSI-X axis, and γ is expressed as $\gamma = 2\pi t/8$. Assuming that the midpoint of each antenna is the observation point, the coordinates of the two observation points r_1 and r_2 are respectively expressed as $(0.5l\cos\gamma, 0.5l\sin\gamma, 0)$ and $(-0.5l\cos\gamma, -0.5l\sin\gamma, 0)$ in the DSI coordinate system. As shown in Figure 5.11, we define the angle between the DSI-Z axis and the background magnetic field as ψ, and the angle between the background magnetic field projected in the DSI-XY plane and the X axis as ϕ.

ECH waves are longitudinal waves oscillating almost perpendicular to the background magnetic field. We set the coordinate system $X_BY_BZ_B$ shown in Figure 5.11, where the Z_B axis is the direction of the background magnetic field. The Y_B direction is the outer product of the Z direction and the B_0 direction projected in the XY plane. The cross product of the Y_B and Z_B axes is the X_B axis.

The DSI-XYZ can be converted into $X_BY_BZ_B$ coordinate system using the transformation matrix T.

$$T = \begin{pmatrix} \cos\psi\cos\phi & \cos\psi\sin\phi & -\sin\psi \\ -\sin\phi & \cos\phi & 0 \\ \sin\psi\cos\phi & \sin\psi\sin\phi & \cos\psi \end{pmatrix}. \tag{5.4}$$

In this numerical calculation, the propagation direction of the ECH wave is perpendicular to the ambient magnetic field for simplicity. The wave vector is represented as $\boldsymbol{k} = k(\cos\alpha, \sin\alpha, 0)$ in the $X_BY_BZ_B$ coordinate system, where k is the absolute value of $\boldsymbol{k}$ and α is the angle between the wave vector and the X_B axis in the X_BY_B plane.

Using this, the electric field of ECH waves at the observation point $\boldsymbol{r_1}$ can be expressed as

$$E(\boldsymbol{r}_{B1}, t) = A\cos(\boldsymbol{k}\cdot\boldsymbol{r}_{B1} - \omega t), \tag{5.5}$$

where A represents the electric field amplitude, which was calculated as 1 and $\boldsymbol{r}_{B1}$ is the observation point $\boldsymbol{r_1}$ in the $X_BY_BZ_B$ coordinate, and it is obtained as

$$\boldsymbol{r}_{B1} = T\boldsymbol{r_1}. \tag{5.6}$$

We assumed the phase velocity of ECH waves v_{ph} of 990 km/s at frequency f of 5570 Hz, which gives $k \sim 0.03$. These parameters are quite similar to those of ECH waves observed in the inner magnetosphere[56]. Due to the directivity of the antenna, only the electric field in the direction of the antenna is received. The observed waveform E_1 is expressed as

$$E_1(t) = T^{-1}\frac{\boldsymbol{k}}{k}\cdot\begin{pmatrix}\cos\gamma\\ \sin\gamma\\ 0\end{pmatrix}E(\boldsymbol{r}_{B1},t). \tag{5.7}$$

The observed amplitude in Equation 5.5 is computed from the inner product of the wave vector $\boldsymbol{k}$ and the antenna direction.

Figure 5.12(a) shows the waveforms obtained from the calculation with $\psi = 90$ degrees, $\phi = 0$ degrees and $\alpha = 90$ degrees. Figure 5.12(b) shows the phase difference between E_1 and E_2.

In this case, the antenna direction is perpendicular to the wave vector of the ECH wave at the initial timing ($t = 0$ seconds) and 4 seconds. As the antenna rotates, the antenna direction is parallel to the wave vector at $t = 2$ seconds, and anti-parallel to the wave vector at $t = 6$ seconds.

The amplitude of observed waveforms depends on the angle between the antenna and electric field fluctuations. The amplitude becomes the maximum when the antenna is parallel to the electric field fluctuations which is parallel to the wave vector. When the wave vector is parallel or anti-parallel to the antenna direction ($t = 2$ seconds and 6 seconds), the amplitude is maximum due to the directivity of the antenna, and the absolute value of phase difference between E_1 and E_2 is also maximum. At $t = 0$ seconds and 4 seconds, when the antenna direction is perpendicular to the wave vector, the observed amplitude is zero and the phase difference is zero because the antenna direction is parallel to the wavefront at these timings.

Next, the phase difference between E_1 and E_2 is examined by changing the direction of the ambient magnetic field which corresponds to the change in the direction of the wave vector. The Arase satellite observes most ECH waves at low latitudes, where the angle between the background magnetic field and the observation plane is about 0 degrees to 15 degrees, and accordingly this numerical calculation is also performed for the case where ψ is close to 90 degrees.

Figure 5.13 shows the calculated phase difference for $\psi = 90$ degrees. The horizontal axis is the angle γ_B between the antenna and the background magnetic field in the spin plane, and the vertical axis shows the phase difference. γ_B is calculated as $\gamma - \phi$. Comparing three cases with $\alpha = 90$ degrees and ϕ of 0, 45, and 90 degrees, the dependence of the phase difference on γ_B remains unchanged when ϕ is changed. This means that ϕ varying in the range of 0 degrees to 360 degrees does not cause any change in phase difference when $\psi = 90$ degrees. Next, comparing the six cases where $\phi = 0$ and α is varied from 0 degrees to 90 degrees every 15 degrees, the maximum phase difference becomes smaller as α becomes smaller. When $\alpha = 90$ degrees, both the wave vector and the amplitude of the electric field are in the $Y_B(=Y)$ direction. As α becomes smaller, the wave vector rotates to the $X_B(=-Z)$ direction, so the component perpendicular to the observation plane increases. At $\alpha = 0$ degrees, the wave vector is perfectly perpendicular to the observation plane in the $-Z$ axis direction in the DSI coordinate system, and the amplitude of the observed waveform is zero. The α varies in the range from 0 degrees to 360 degrees, which affects the maximum phase difference in one satellite spin.

Figure 5.14 shows the results for $\psi = 80$ degrees. In this case, both the maximum value of the phase difference and its timing change when ϕ and α change, respectively. When α changes, the maximum value of the phase difference changes as in the case of $\psi = 90$ degrees and γ_B with the maximum phase difference also changes. At $\psi = 80$ degrees, the change by ϕ is small, and the change α is relatively large. For any value of α, the phase difference is consistently expressed as a sine function, and the magnitude of the phase difference becomes 0 and the maximum value occurs every 90 degrees.

We reproduced the observed phase difference of the ECH waves using this numerical model. In the case of the phase difference of ECH wave at 5696 Hz shown in Figure 5.5, the maximum phase difference is 9.89 degrees at γ_B =82.5 degrees. The black line with error bars in Figure 5.15 shows the phase difference at 5696 Hz in Figure 5.5. Since the mean of phase differences is calculated every 5 degrees, there is an error of ±2.5 degrees in γ_B which takes the maximum value. The standard deviation of the phase difference is 0.75 degrees at the maximum. The red line in Figure 5.15 is the phase difference reproduced by this numerical model. The used parameters are ψ =83.1 degrees, ϕ =0 degrees, α =222 degrees, f =5696 Hz and v_{ph} =2309 km/s. The maximum phase difference of 9.89 degrees appears at $\gamma_B = 82.3$ degrees in our numerical model. Table 1 lists the parameters to reproduce for the remaining four frequencies in Figure 5.5 and one frequency shown in Figure 5.7 for which the phase difference has a sinusoidal shape. Our model can be used to estimate possible parameters of ECH wave vectors by comparison of the observed phase difference with the numerical model.

5.4 Discussion and conclusions

We calculated the phase difference of the ECH waves observed by the Arase satellite and found that the majority of them had a sine-shape phase difference depending on the spin period. The sine-type phase difference is also shown in the numerical results, and 47 events, including the event shown in Figure 5.4, can be explained by the numerical results. The analyzed phase difference represented by the sine function has a maximum value around $\gamma_B = 90$ degrees and 270 degrees. From the numerical calculations in the previous section, γ_B at the peak will differ from 90 degrees or 270 degrees in the case that the wave vector has a large component perpendicular to the observation plane. Assuming that the ECH waves are plane waves propagating in one direction, the wave vector of observed ECH waves is approximately in the observation plane. If γ_B values that take the peak can be calculated accurately, it is possible to correctly obtain the ECH wave vector from a single dimensional electric field waveform observation.

The events where the phase difference was 0 for any γ_B are the second most frequently observed. This result can also be explained by the numerical experiments. The numerical calculations show that the phase difference becomes zero when the ECH wavefront coincides with the antenna. In this case, the observed amplitude is also zero, which differs from the Arase satellite observations showing that significant ECH wave intensity is observed. However, even when the antenna and wavefront do not perfectly coincide, the observed phase difference might be near zero if the apparent phase velocity is very fast.

According to this numerical calculation, there are two possible reasons why two different phase difference trends are observed in one event, as shown in Figure 5.7. One is the possibility that the phase velocity is different at each frequency, and the other is the possibility that the wave vector direction is different at each frequency. Since the growth rate of ECH waves depends on frequency and wave normal angle, it is theoretically possible for ECH waves to have different wave vector directions in different frequency bands[57, 58].

The statistical investigation shows that the spin-dependent phase difference with the sinusoidal shape is more often observed compared with the phase difference close to zero without spin dependence. Numerical calculations show that changing the value of α does not result in a linear change in the amplitude of the phase difference. When α is small in the range of 0 to 90 degrees, both the amplitude and the γ_B of the peak phase difference change significantly, whereas when α is larger than 45 degrees, this change is small. Figure 5.16 shows the phase difference for α and γ_B at $\psi = 80$ degrees. γ_B with the largest phase difference for each α is indicated by the black line and γ_B with the smallest phase difference for each α is indicated by the red line. In many α, the peak in the phase difference is close to $\gamma_B = 90$ degrees. In the case of α near 0 and 180 degrees, the peak changes greatly and the amplitude of the phase difference become small. Almost all of the events used in the statistical analysis have a peak phase difference with $\gamma_B \sim 90$ degrees, and this result is consistent with the numerical results for $\psi = 80$ degrees.

Although we constructed numerical model to compute the phase difference, the analytic expression of the phase difference is also derived. The waveforms at the observaion point $\boldsymbol{r}_1$

and $\boldsymbol{r_2}$ can be expressed as:

$$E_j(t) = A' \cos\left(\boldsymbol{k} \cdot \boldsymbol{T}\boldsymbol{r_j} - \omega t\right) \ (j = 1, 2), \tag{5.8}$$

where A' represents the amplitude that takes into account the direction difference between the antennas and electric field vector. The phase difference between the observed points can be expressed as:

$$\Delta\theta = \boldsymbol{k} \cdot \boldsymbol{T}\boldsymbol{r_1} - \boldsymbol{k} \cdot \boldsymbol{T}\boldsymbol{r_2}. \tag{5.9}$$

Substituting $\boldsymbol{k}$, $\boldsymbol{T}$, $\boldsymbol{r_1}$, and $\boldsymbol{r_2}$ in Equation 5.9, $\Delta\theta$ is given as:

$$\Delta\theta = 2k \times 0.5l\,(\cos\alpha, \sin\alpha, 0) \cdot \begin{pmatrix} \cos\psi\cos\phi & \cos\psi\sin\phi & -\sin\psi \\ -\sin\phi & \cos\phi & 0 \\ \sin\psi\cos\phi & \sin\psi\sin\phi & \cos\psi \end{pmatrix} \begin{pmatrix} \cos\gamma \\ \sin\gamma \\ 0 \end{pmatrix}, \tag{5.10}$$

$$\Delta\theta = kl\,(\cos\psi\cos\phi\cos\gamma\cos\alpha + \cos\psi\sin\phi\sin\gamma\cos\alpha - \sin\phi\cos\gamma\sin\alpha + \cos\phi\sin\gamma\sin\alpha) \tag{5.11}$$

From the relationship of $\gamma_B = \gamma - \phi$, following equations are avaiable:

$$\sin\gamma_B = \sin\gamma\cos\phi - \cos\gamma\sin\phi, \tag{5.12}$$

$$\cos\gamma_B = \cos\gamma\cos\phi + \sin\gamma\sin\phi. \tag{5.13}$$

Thus, $\Delta\theta$ is expressed by the function of k, ψ, α, and γ_B as:

$$\Delta\theta = kl(\cos\psi\cos\alpha\cos\gamma_B + \sin\alpha\sin\gamma_B). \tag{5.14}$$

The wave vector can be estimated from the γ_B that takes the peak of the phase difference. The Arase satellite acquires only a one-dimensional electric field when it performs the interferometry observation. In such a case, it is very difficult to estimate wave vector direction because of the lack of complete electric field vector information. However, if γ_B at the peak of the phase difference can be accurately determined from the interferometry observation, it is expected that the accuracy of the wave vector direction improves. We will attempt to accurately estimate wave vectors in future work, which is important to understand the excitation and propagation of ECH waves and their effects on the plasma environment.

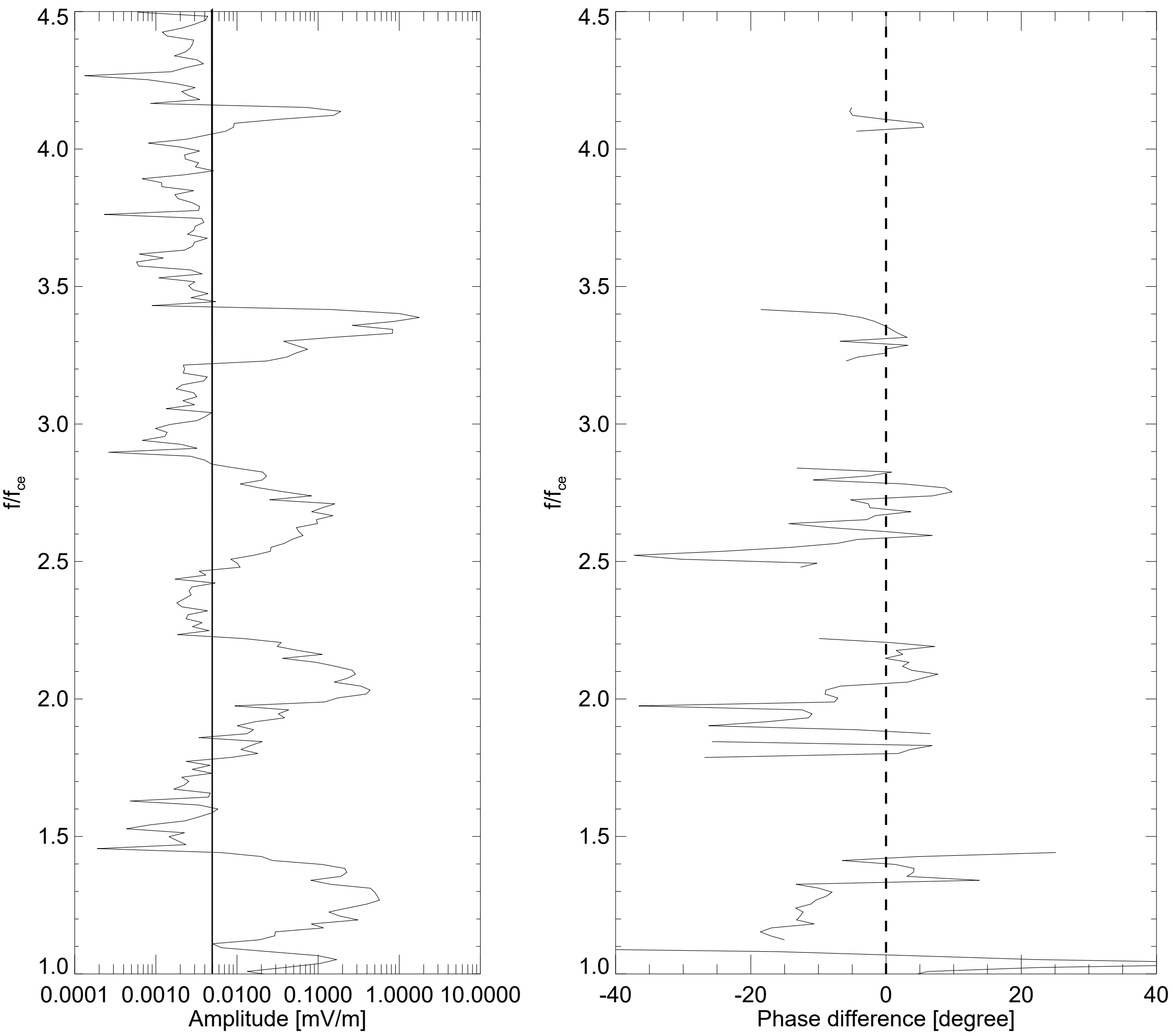

Figure 5.3: (Left) Amplitude and (right) phase difference between E_{V1} and E_{V2} derived from the PWE/WFC observation at 00:00:40.647 UT on 8 September as a function of normalized frequency by f_{ce}. The vertical line in the left figure indicates the threshold value of 0.005 mV/m.

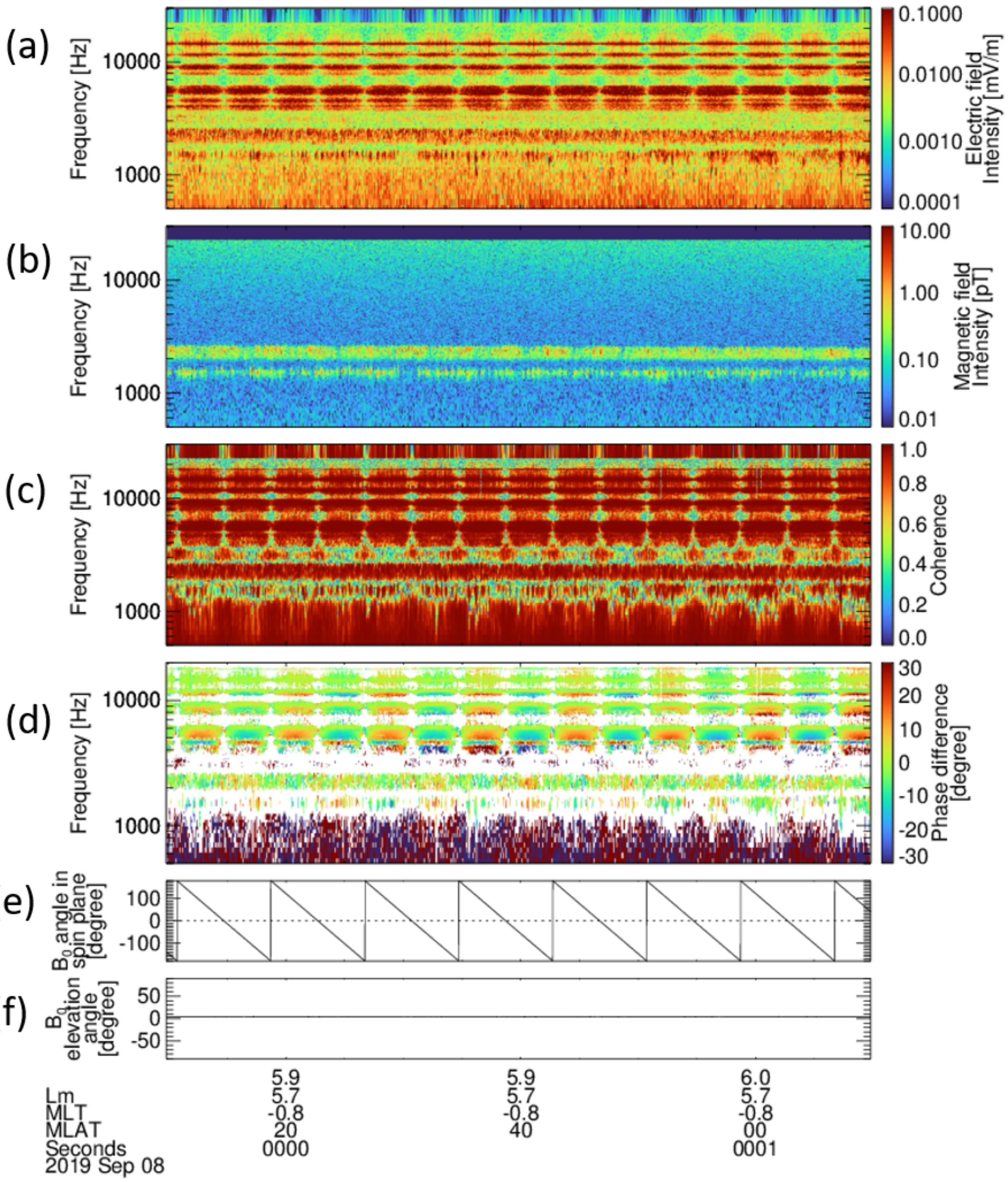

Figure 5.4: ECH events near 00:00:20 on September 8, 2019; For each part, from top left: (a)spectral intensity of E_{V1} at each angular frequency, where the red line represents the cyclotron frequency and the white lines represent half and integer multiples of the cyclotron frequency, (b)spectral intensity of the magnetic field in the β direction, (c)coherence between E_{V1} and E_{V2}, (d)phase difference between E_{V1} and E_{V2} at times and frequencies with high coherence, (e)angle between the background magnetic field and antenna V1 when projected onto the spin plane, (f)elevation angle of background magnetic field relative to the spin plane

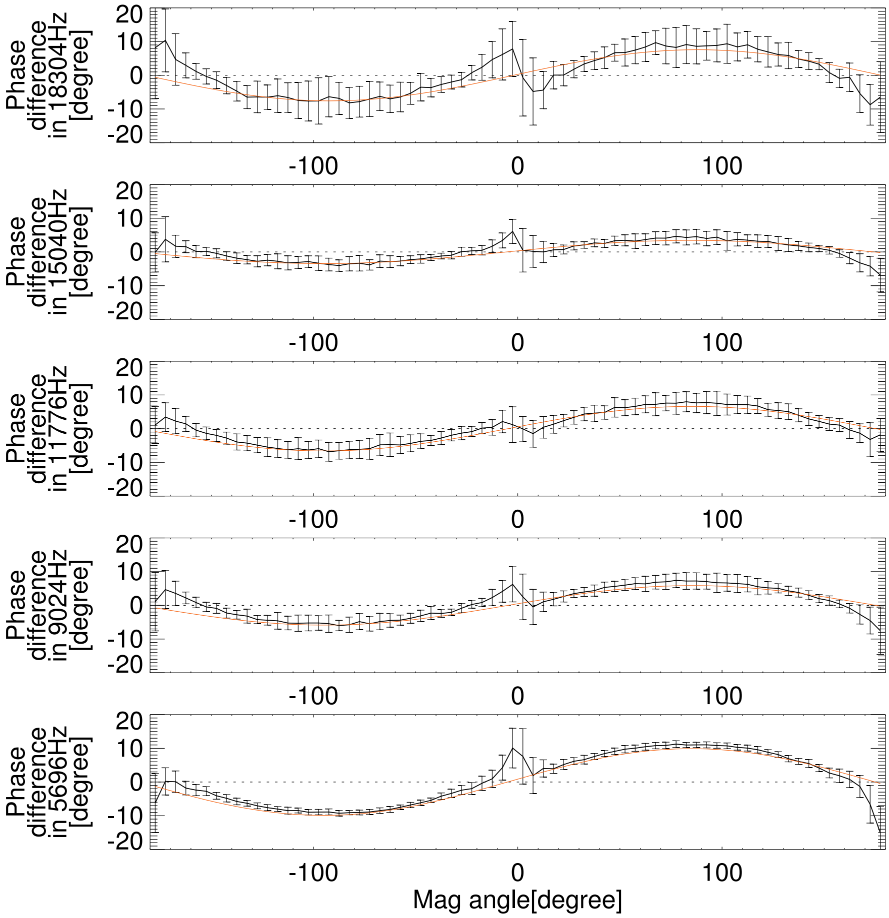

Figure 5.5: Phase difference at the events near 00:00:20 on September 8, 2019; Phase difference between E_{V1} and E_{V2} relative to the spin angle γ_B at the chosen frequencies between integer multiples of the cyclotron frequency. The orange line represents the result fitted with a sine function. Phase difference has a sinusoidal shape

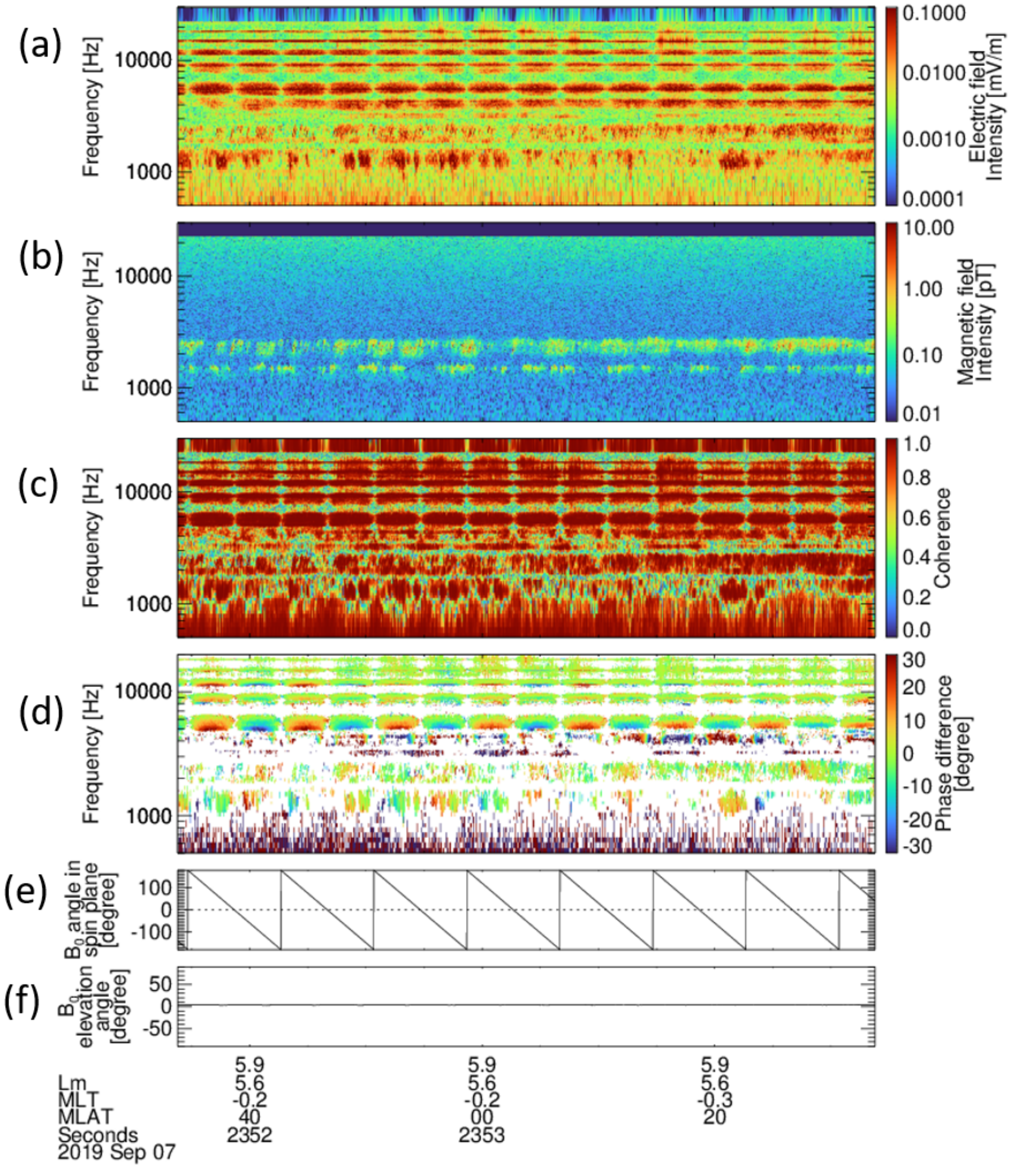

Figure 5.6: ECH event near 06:02:00 on September 22, 2019; Each item in the figure represents the same parameters as those shown in Figure 5.4

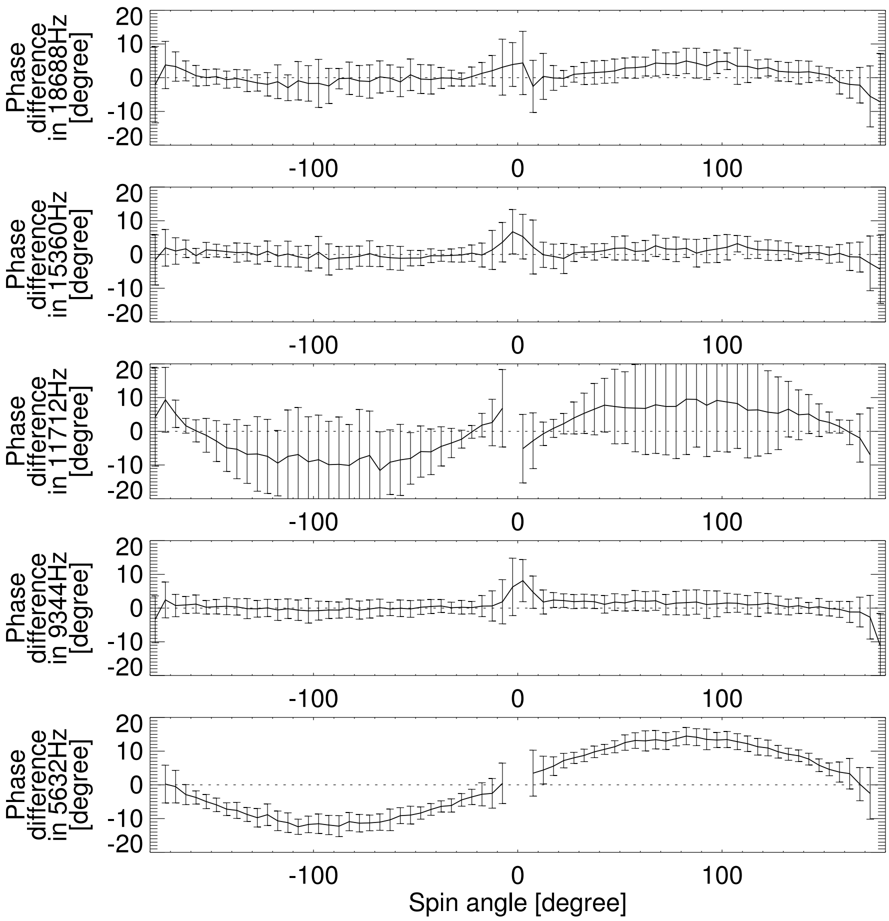

Figure 5.7: Phase difference at the event near 06:02:00 on September 22, 2019; Phase difference between E_{V1} and E_{V2} relative to the spin angle γ_B at the chosen frequencies between integer multiples of the cyclotron frequency. Phase difference is almost constant around 0

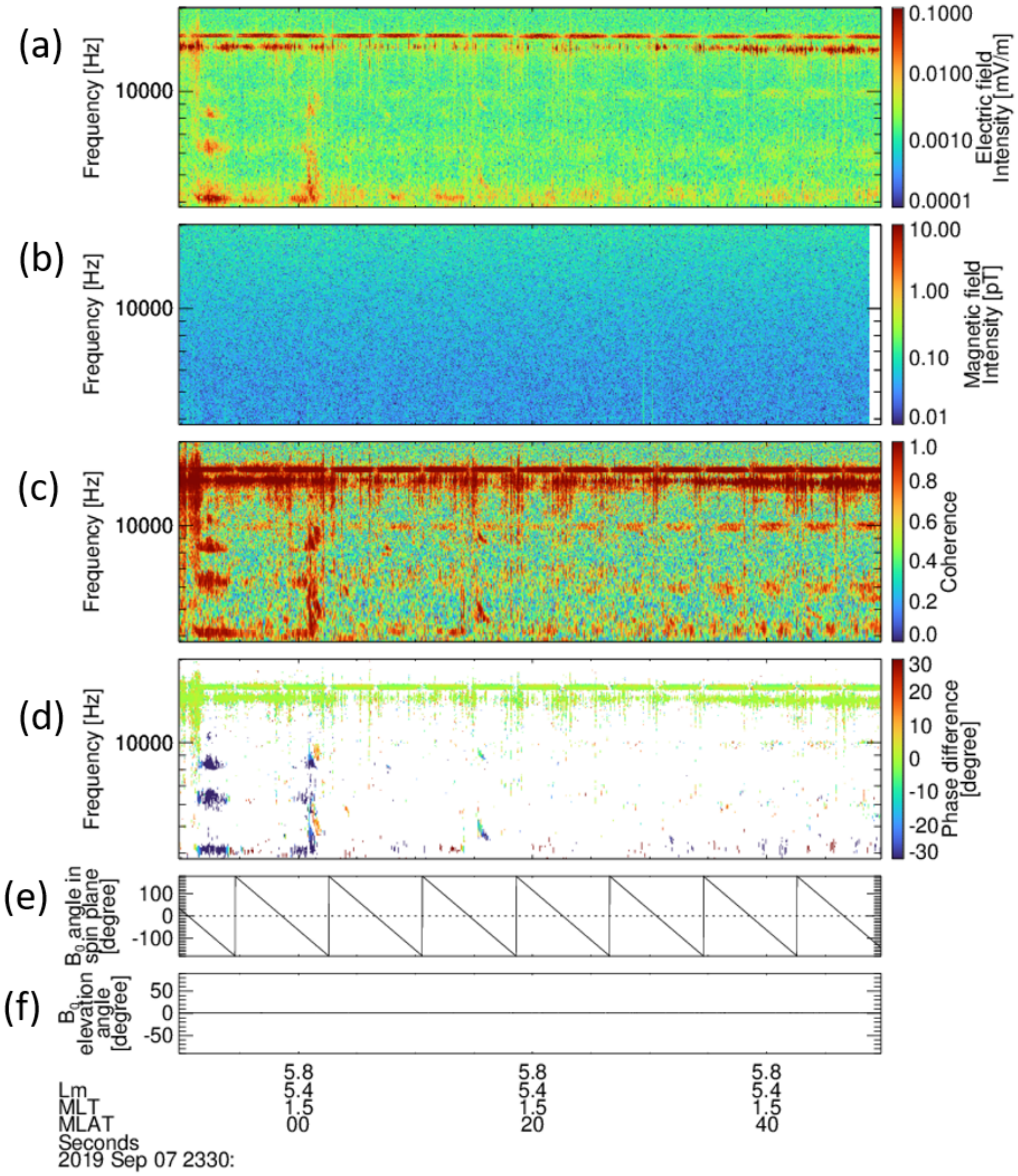

Figure 5.8: Parameter γ set to represent the rotation of the antenna in DSI coordinate system, and the spin angle γ_B with respect to the background magnetic field projected onto the spin plane

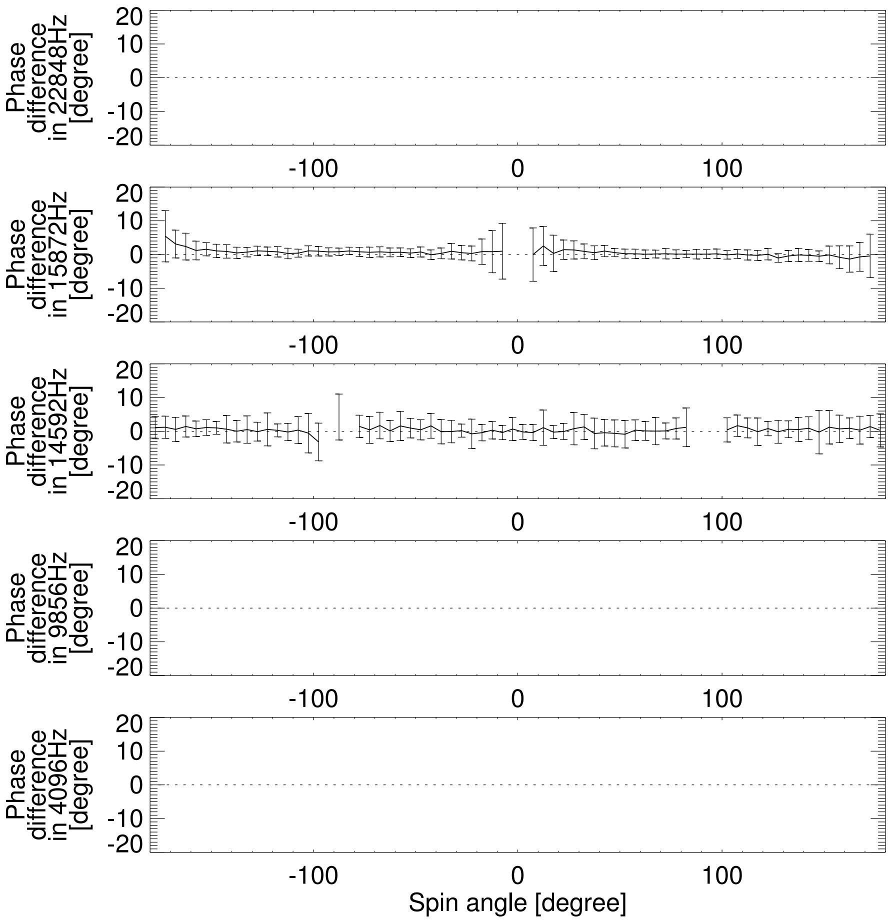

Figure 5.9: The direction of the background magnetic field, denoted by the zenith angle ψ and azimuth angle ϕ, and the k vector, denoted by the angle α from X_B in the coordinate system along the magnetic field

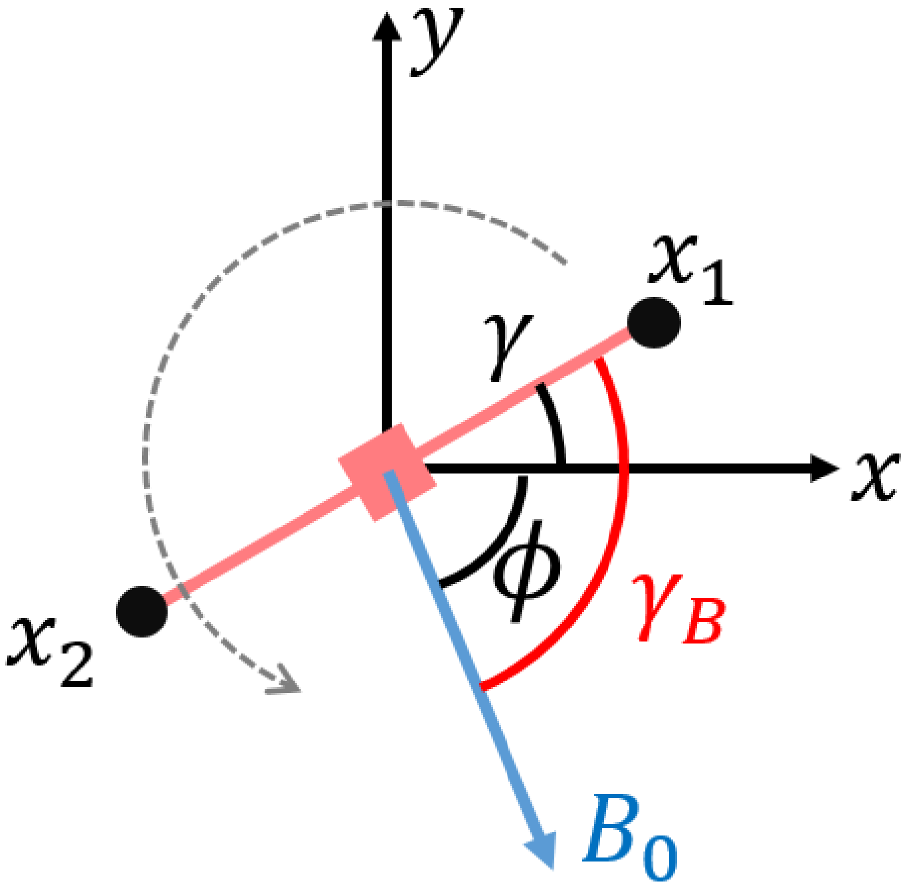

Figure 5.10: (a)Outline of the observed model wave of ECH in the spin period (b)Calculated phase difference

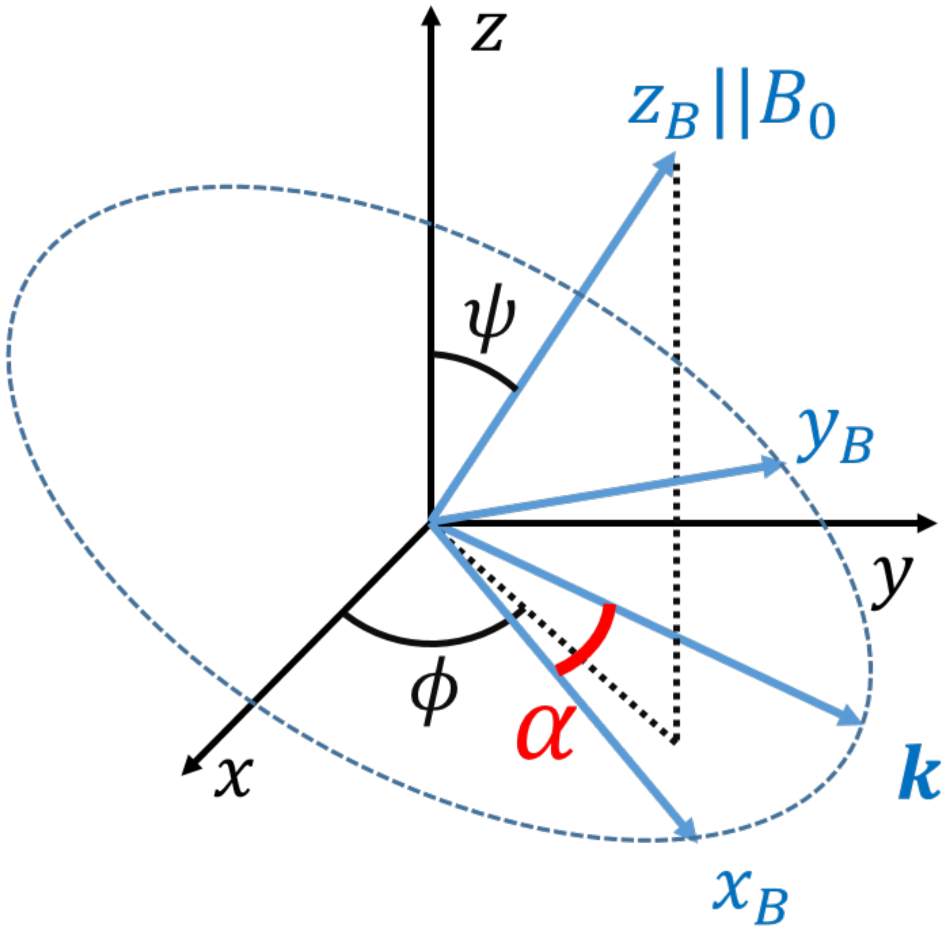

Figure 5.11: Phase difference of the ECH waves with respect to the angle γ_B, which represents the satellite spin, when $\psi = 90$ degrees and ϕ and α are varied, respectively

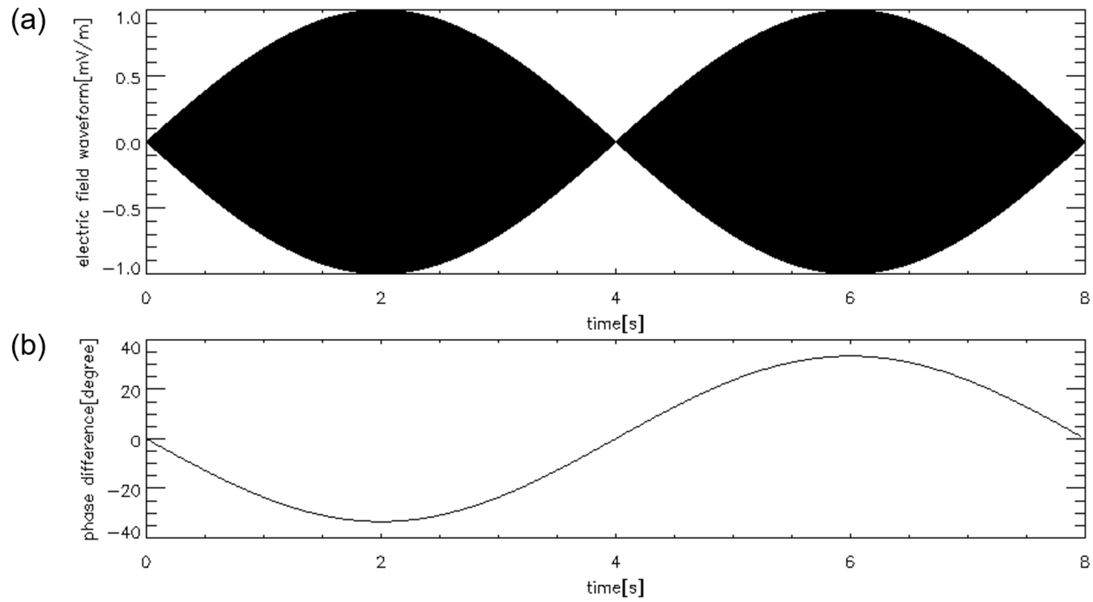

Figure 5.12: Phase difference of the ECH waves with respect to the angle γ_B, which represents the satellite spin, when $\psi = 80$ degrees and ϕ and α are varied, respectively

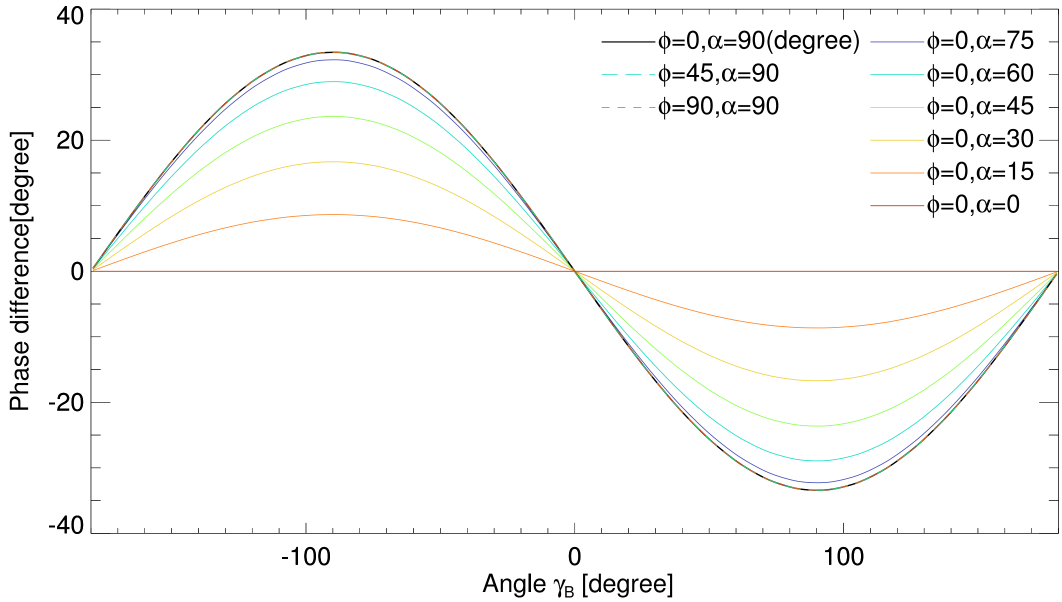

Figure 5.13: Phase difference relative to α and γ_B at $\psi = 80$ degrees and $\phi = 0$ degrees where the black dots indicate γ_B with the largest phase difference in each α and the red dots indicate γ_B with the smallest phase difference

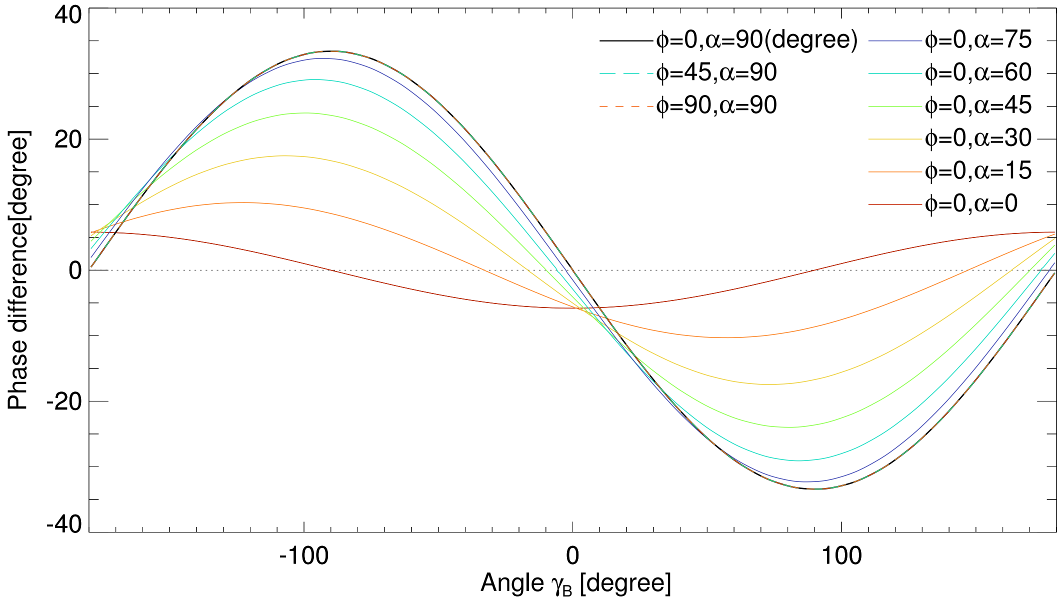

Figure 5.14: Phase difference of the ECH waves with respect to the angle γ_B, which represents the satellite spin, when $\psi = 80$ degrees and ϕ and α are varied, respectively

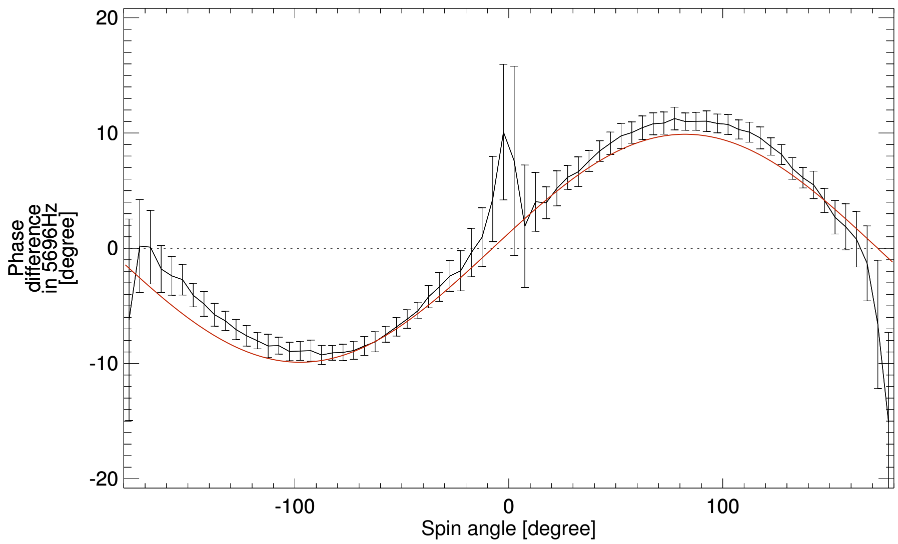

Figure 5.15: The black line shows the phase difference relative to γ_B at 5696 Hz in Figure 2, and the red line is the phase difference reproduced by this numerical model at $\psi = 83.1$ degrees, $\phi = 0$ degrees, $\alpha = 222$ degrees, $f = 5696$ Hz and $v_{\mathrm{ph}} = 2309$ km/s.

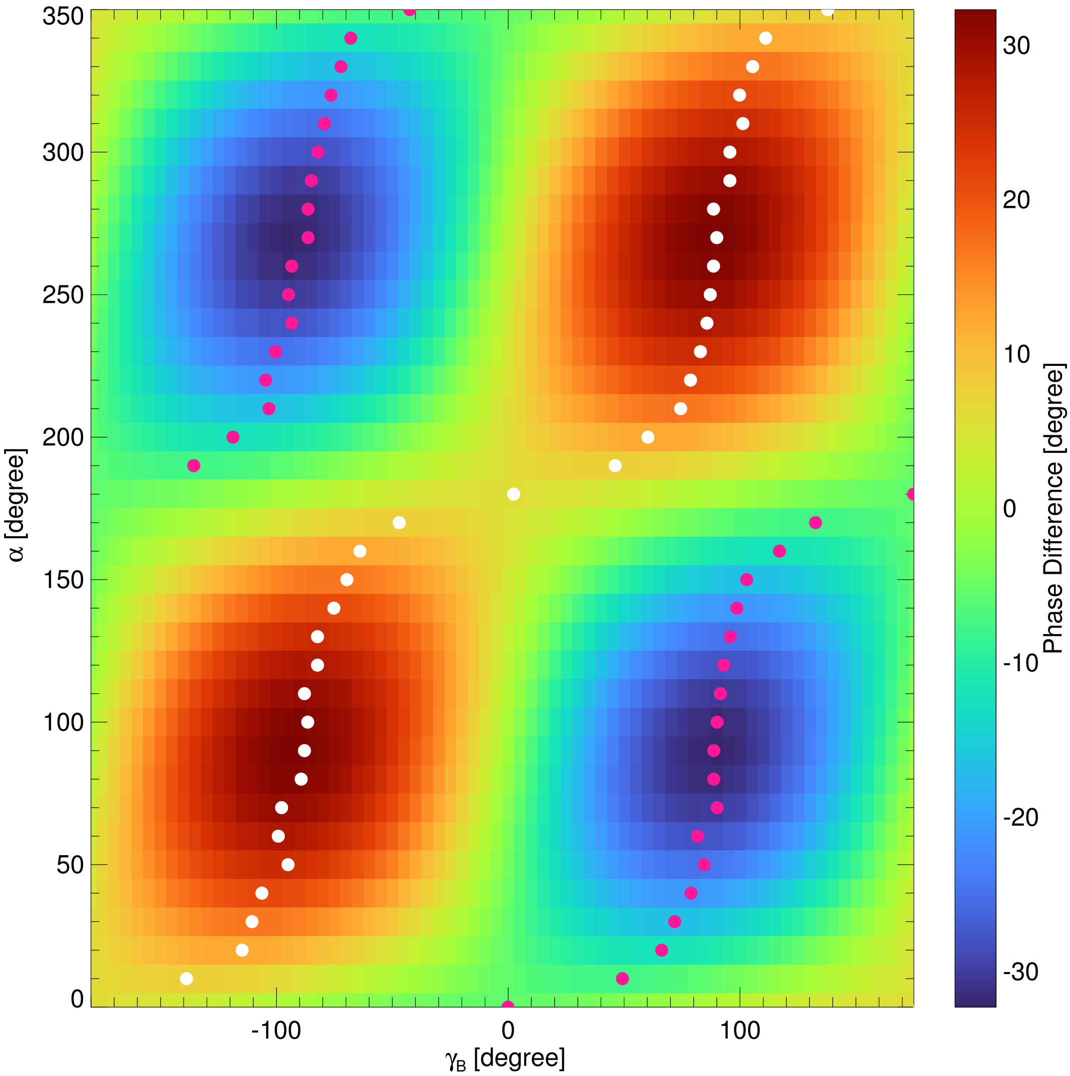

Figure 5.16: Phase difference relative to α and γ_B at $\psi = 80$ degrees and $\phi = 0$ degrees where the black dots indicate γ_B with the largest phase difference in each α and the red dots indicate γ_B with the smallest phase difference

Chapter 6

Estimation of cold electron temperatures through the dispersion of electron cyclotron harmonic waves

6.1 Introduction

The Earth's magnetosphere is filled with plasma particles in a wide energy range. It is known that the plasmasphere is filled with low-temperature and high-density plasma. This is supported by estimates of the plasmasphere's extent through the observation of ion temperatures and densities[59]. It has been known that plasma density and temperature change in the magnetosphere at different altitudes[60, 61].

High-energy particles are detected by the various types of particle instruments onboard the satellites. There is the lowest energy limit of particles detected by particle instruments depending on their measurement principles. For instance, in the case of LEP-e onboard the Arase satellite, the measurable lowest energy is around 16 eV[62]. The spacecraft charging is also a significant factor in limiting the energy range of particles measurable since the particles with energies below charging voltage cannot reach particle detectors[63][64, and therein]. It is necessary to take into account that the plasma is accelerated or decelerated by the satellite potential. Thus, the distribution of very low energy particles below a few eV in the magnetosphere remains to be discovered.

The total electron density n_e can be estimated from observation of Upper Hybrid Resonance (UHR) frequency[e.g. 65]. Despite uncertainties in the determination of UHR frequency, n_e obtained through this method often exceeds the electron density determined from the particle instruments, suggesting the presence of a substantial population of low-energy plasma below the measurable energy limit of the particle instrument[66].

Electrostatic Electron Cyclotron Harmonic (ECH) waves have been analyzed to diagnose plasma properties. ECH waves are plasma waves observed within the magnetosphere. They exhibit a harmonic structure with intensity peaks at frequencies close to (n+1/2) times of the electron cyclotron frequency f_{ce}. Strong radiation occurs near the UHR frequency. ECH waves have wave normal angles nearly perpendicular to the background magnetic field. ECH waves are characterized as electrostatic waves. ECH waves were first observed by the OGO-5 satellite [20] and have been observed by various satellites within Earth's magnetosphere, frequently in low magnetic latitudes [49, 22]. They are known to be excited by the coexistence of a cold core electron distribution and hot electrons with a loss cone [67, 48, 68, 69].

Hubbard and Birmingham [52] classified the frequency structure of observed ECH waves into several categories. To understand the excitation conditions of ECH waves in each category, calculations of linear growth rates were performed by changing plasma properties. [52] proposed that the frequency structure of ECH waves could be used to diagnose the density and temperature of cold electrons.The hot electron density and temperature affect the dispersion curve, and when the cold electron density is dominant, narrow band emission occurs near the plasma frequency. In this case, the dispersion relation of the ECH wave depends on the temperature of the cold electrons. Moncuquet et al. [24] estimated the wavelength of the ECH waves from the spin modulation of the electric field amplitude observed by the Ulysses spacecraft and the theoretical relationship between wavelength and antenna response. The experimental dispersion curve fit the theoretical curve and allowed for the determination of cold electron density and temperature.

We have estimated the cold electron temperature in the Earth's inner magnetosphere using the interferometry observations of ECH waves on the Arase satellite. Interferometry observations are used to estimate phase velocities of waves[e.g. 54], enabling us to determine the dispersion relation. In this study, we perform the estimation of the phase velocity of ECH waves based on the interferometry observation by the Arase satellite, and the dispersion relations of ECH waves are derived. The dispersion relation from the observation is compared with the theoretical dispersion curved computed by Kyoto University Plasma Dispersion Analysis Package (KUPDAP)[70], and the temperature of cold electrons are estimated.

6.2 Estimation method of wave vector direction for ECH waves

We show a method to infer wave vectors from numerical calculations using the spin dependence of the phase difference of ECH waves.

Two observation points of the Arase satellite's interferometry observation, which spins in 8 seconds, are expressed as

$$\boldsymbol{r_1} = 0.5l(\cos\gamma, \sin\gamma, 0), \tag{6.1}$$

$$\boldsymbol{r_2} = -0.5l(\cos\gamma, \sin\gamma, 0), \tag{6.2}$$

in the DSI coordinates, respectively. In the DSI coordinate system, the Z-axis is parallel to the spin axis, the X-axis is defined with respect to the sun direction, and the Y-axis is in the direction of the outer product of the Z-and X-axes.

We consider another coordinate system $X_BY_BZ_B$ along the background magnetic field. Z_B axis coincides with the direction of the background magnetic field The DSI-XYZ can be converted into $X_BY_BZ_B$ coordinate system using the transformation matrix T.

$$T = \begin{pmatrix} \cos\psi\cos\phi & \cos\psi\sin\phi & -\sin\psi \\ -\sin\phi & \cos\phi & 0 \\ \sin\psi\cos\phi & \sin\psi\sin\phi & \cos\psi \end{pmatrix}. \tag{6.3}$$

The electric field of the ECH wave in $X_BY_BZ_B$ coordinate is expressed as

$$E(r_B, t) = A\cos(\boldsymbol{k}\cdot\boldsymbol{r_B} - \omega t), \tag{6.4}$$

$$\boldsymbol{k} = k\left(\cos\alpha\sin\zeta, \sin\alpha\sin\zeta, \cos\zeta\right), \tag{6.5}$$

where A represents the amplitude of the wave and ζ represents the wave normal angle. α is a variable that can take values from 0 degrees to 360 degrees. In the DSI coordinate system, the wave vector is expressed as

$$\boldsymbol{k}_{\mathrm{DSI}} = T^{-1}\boldsymbol{k}. \tag{6.6}$$

The observed electric field intensity and phase difference are the maximum when the antenna is parallel to the wave vector projected onto the spin plane. The spin angle when this happens is denoted as $\gamma_{\max}$.

$$\gamma_{\max} = \arctan\left(\frac{\boldsymbol{k}_{\mathrm{DSI},y}}{\boldsymbol{k}_{\mathrm{DSI},x}}\right), \tag{6.7}$$

This equation shows the relationship between $\gamma_{\max}$ and the two variables α and ζ, which determine the wave vector. α can take values from 0 to 360 degrees, while the wave normal angle ζ is almost 90 degrees for ECH waves. In this analysis, ζ was assumed to be 90 degrees. α was determined by calculating the spin angle $\gamma_{\max}$ that maximizes the phase difference from the observation.

6.3 Estimation of cold electron temperature

Cold electron temperature is estimated by comparison of the dispersion relation derived from the above procedure and the theoretical one. To derive the theoretical dispersion relation of ECH waves, density, temperature, and anisotropy of cold and hot electron populations are required. We estimated the parameters of hot electrons from the electron populations in the energy range from 67 eV to 1 keV observed by LEP-e. To avoid the influence of photoelectrons and satellite charge-up, lower energy data were omitted and electron data above 67 eV were used in the fitting process. We calculate phase space density from the LEP-e observation and fit them to the bi-Maxwellian distribution function represented as

$$F = n\frac{m_e}{2\pi k_B T_\perp}\sqrt{\frac{m_e}{2\pi k_B T_\parallel}}\exp\left(-\frac{K_\perp}{k_B T_\perp}\right)\exp\left(-\frac{K_\parallel}{k_B T_\parallel}\right), \tag{6.8}$$

where n represents the observed hot electron density and m_e represents the electron rest mass. $T_\perp$ and $T_\parallel$ are the temperatures perpendicular and parallel to the background magnetic field, respectively. $K_\perp$ and $K_\parallel$ denote kinetic energy in the perpendicular and parallel directions. k_B is the Boltzmann constant. We determine $T_\perp$, $T_\parallel$, and n through fitting using the least-squares method, which allows us to estimate the electron density and temperature within the LEP-e observation range.

Subsequently, we estimate the density of cold electrons whose energy is lower than the lowest energy limit of LEP-e as follows:

$$n_{\mathrm{cold}} = n_e - n, \tag{6.9}$$

where n_{cold} is the density of cold electrons, n_e is total electron density determined from the UHR frequency. We assume that the temperature of cold electrons is isotropic. The temperature of cold electrons T_{cold} is expressed as:

$$T_{\mathrm{cold}\perp} = T_{\mathrm{cold}\parallel} = \frac{1}{\sqrt{2}}T_{\mathrm{cold}}. \tag{6.10}$$

T_{cold} is estimated from the comparison of the dispersion relation derived from the Arase observation with the theoretical one obtained by changing T_{cold}.

6.4 Analysis

We analyzed the event which started at 07:09:30 on 7 September 2019 with a duration of 60 seconds. At this event, the Arase satellite was positioned at a radial distance of 5.6 R_E (where

R_E represents Earth's radius), magnetic latitudes ranging from -0.9 to -1.0 degrees, and a magnetic local time of 6.8 MLT.

Figure 6.1(a) shows frequency-time spectrograms of the electric field. The electric field was observed using Antenna V1. Figure 6.1(b) illustrates the phase difference between E_{V1} and E_{V2}, while Figure 6.1(c) shows the apparent phase velocity v'_{ph} calculated from the phase difference shown in (b). The phase difference and v'_{ph} are positive when E_{V1} is followed by E_{V2}. It's important to note that the calculations for (b) and (c) were performed only when the electric field intensity exceeded 2×10^{-3} mV/m, and the coherence between E_{V1} and E_{V2} was greater than 0.9. The coherence is expressed as

$$Coh(f) = \sqrt{\frac{|\langle W_1(f)W_2^*(f)\rangle|^2}{\langle|W_1|\rangle\langle|W_2|\rangle}}. \tag{6.11}$$

Figure 6.1(d) represents the variations in the spin angle, which is defined as the angle between the antenna V1 and the background magnetic field direction projected on the spin plane. The elevation angle of the background magnetic field direction with respect to the spin plane was almost 11.2 degrees at this event.

Looking at the time variation of phase differences at each frequency, it is evident that they exhibit an 8-second periodicity, which is attributed to the satellite's spin.

We calculated the average profiles of the phase difference as a function of the spin angle during this period. Figure 6.2 shows the average profiles of the phase difference as a function of the spin angle at 5060 Hz, 5632 Hz, and 7936 Hz. These frequencies have local intensity peaks in the frequency range from f_{ce} to $2f_{\mathrm{ce}}$. The mean and standard deviation of the phase difference are computed every 5 degrees of the spin angle.

Around the maximum or minimum phase difference, the values are close to each other. γ_{max} tends to change due to errors in observation. Considering that the electric field sensor would be perpendicular to the wave vector projected on the spin plane at the spin angle of the minimum field intensity γ_{Emin}, and $\gamma_{\mathrm{Emin}}\pm 90$ degrees are selected as the maximum and minimum phase difference. We selected the phase difference with the smaller standard deviation among them as the representative phase difference and used it for the phase velocity calculation.

From these phase differences, the apparent phase velocity v'_{ph} is calculated. The wave vector direction is also estimated, and the angle β that the wave vector makes with the spin plane is determined. Since the spin angle is incremented in a 5-degree step, the parameter γ_{max} for estimating the wave vector direction has an error of ± 2.5 degrees, and estimating the direction of the wave vector using that value leads to an error.

In the case of this event, based on the LEP-e observation, the electron density n is $0.865\times10^6/\mathrm{m}^3$, $T_{||}$ is 158 eV, and $T_\perp$ is 299 eV. Furthermore, based on the HFA observation, the UHR frequency exists at 54.9 kHz, resulting in a total electron density n_e of $37.4\times10^6/\mathrm{m}^3$. The density of low-energy electrons outside the LEP-e observation range is dominant at this event.

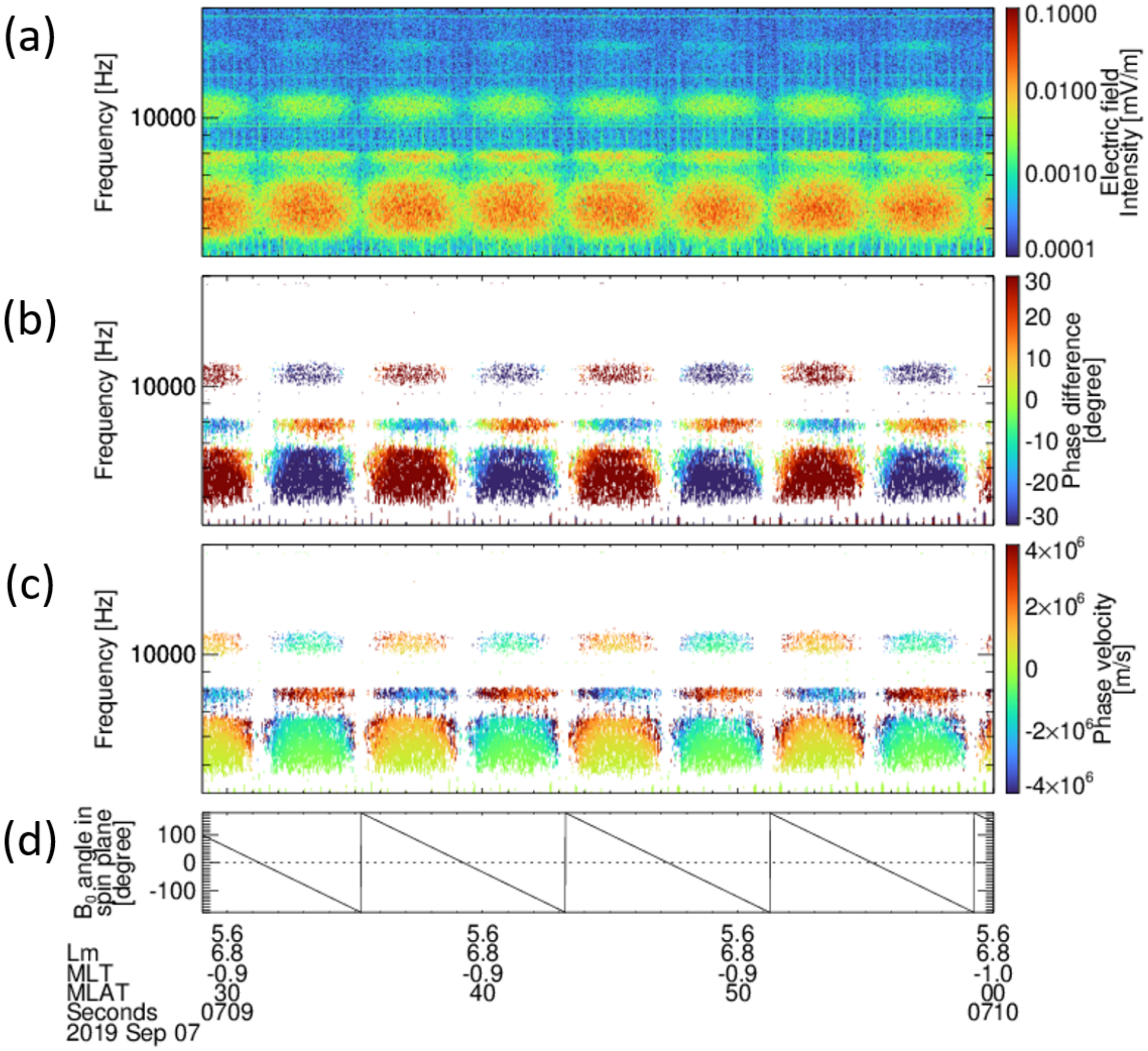

Figure 6.1: ECH events near 07:09:30 on 7 September 2019. For each part, from top: (a)dynamic spectrum of E_{V1}, (b)phase difference between E_{V1} and E_{V2} at times and frequencies with high coherence, (c)the calculated apparent phase velocity v'_{ph}, (d)angle between the antenna V1 and the background magnetic field projected onto the spin plane

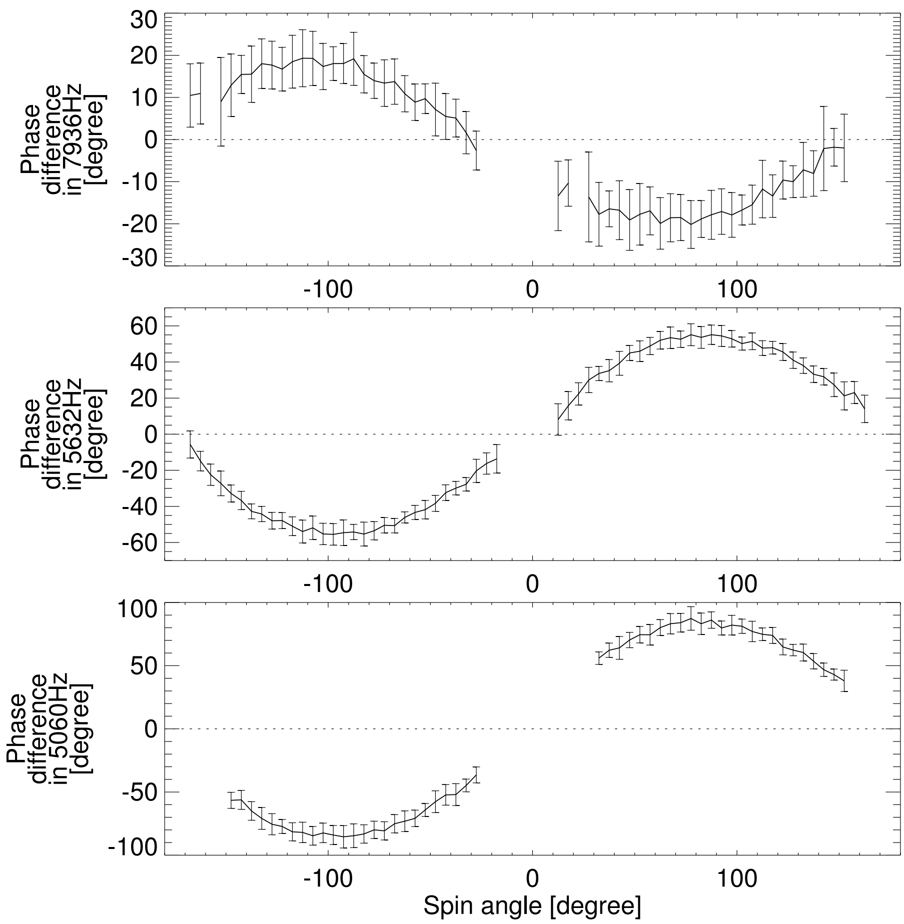

Figure 6.2: Mean of phase difference with respect to spin angle at 5060 Hz, 5632 Hz and 7936 Hz. Error bars indicate standard deviation

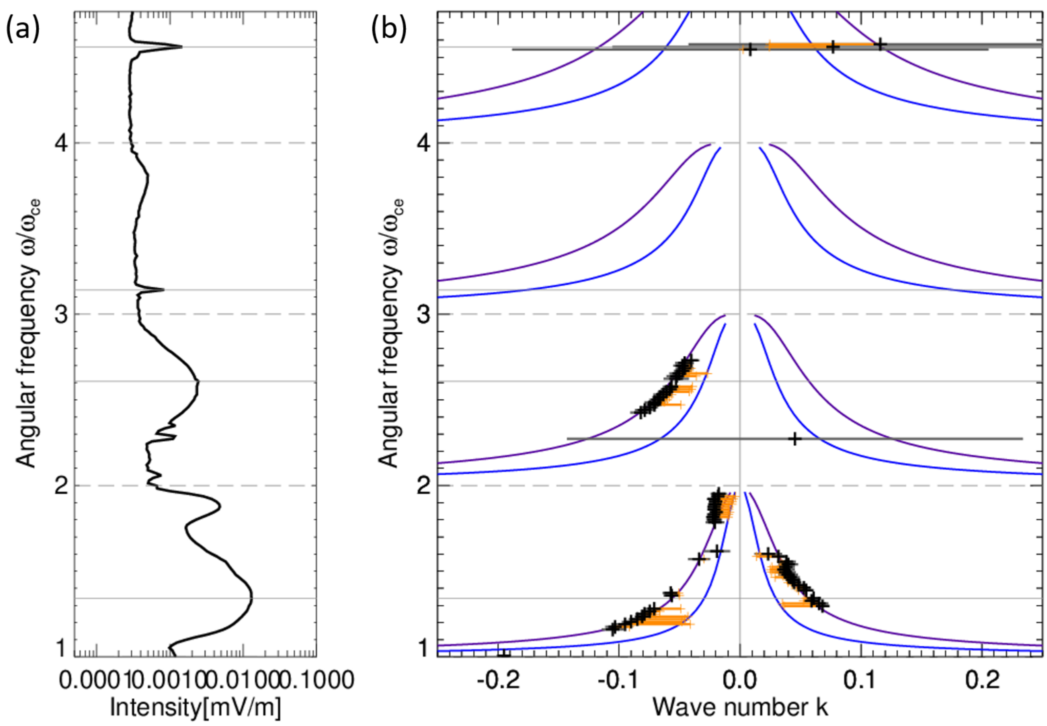

Figure 6.3: (a)The electric field intensity versus the normalized angular frequency, (b)Purple lines show the dispersion relation of ECH waves derived from KUPDAP using the parameters listed in Table 1. The blue line is the dispersion relation derived by changing the parameters in Table 1 to $T_{\mathrm{cold}\perp} = T_{\mathrm{cold}\|} = 7/\sqrt{2}\,\mathrm{eV}$. Plus symbols are dispersion relation derived from the interferometry observation

Table 6.1: Parameters used for computation of dispersion curves by KUPDAP

Particles	density($10^6/\mathrm{m}^3$)	$T_{\parallel}$(eV)	$T_{\perp}$(eV)
e	0.865	158	299
e_{cold}	37.3	$1.9/\sqrt{2}$	$1.9/\sqrt{2}$
H^+	37.4	$1/\sqrt{2}$	$1/\sqrt{2}$

The derived $\omega - k$ relationship is shown in Figure 6.3. Figure 6.3(a) shows the intensity for each angular frequency. The vertical axis indicates the angular frequency normalized by the cyclotron angular frequency and the horizontal axis represents the electric field intensity. Figure 6.3(b) shows the wavenumber for each angular frequency. The wavenumber at each angular frequency has the error arising from the determination of the wave vector direction using $\gamma_{\max}$. The black and orange plus symbols represent the largest and smallest wavenumber cases, respectively, considering the error in the wave vector direction. The gray error bars result from the standard deviation of the phase differences, but this error is too small to recognize in Figure 6.3(b). The orange error bars come from the uncertainty in the wave vector direction. The purple line in the figure represents the dispersion curve obtained from KUPDAP using the parameters listed in Table 6.1. We consider that each distribution is represented by a bi-Maxwellian distribution without loss cone since the change in loss cone parameters does not modify the real frequency and wave number of ECH waves.

In the case of the cold electron temperature of 1.9 eV, the dispersion curve obtained from KUPDAP (purple lines in Figure 6.3) falls within the range of the error bar at each frequency. The dispersion curves derived from KUPDAP assuming the cold electron temperature of 7 eV (blue lines in Figure 6.3) are in some agreement with the observed dispersion curves for the smallest wavenumbers (orange plus symbols appears in Figure 3). Considering the fact that the dispersion curves derived from KUPDAP assuming the cold electron temperature of 1.9 eV follow well with the datapoints with smaller error bars, the cold electron temperature during this event is estimated as 1.9 eV.

The same procedure is applied to other five cases of interferometry observation of ECH waves. The temperature that coincides with the smaller wavenumbers was determined as the maximum temperature. The temperature that matched the data at the greatest number of frequencies was defined as the estimated temperature. The results of the estimated cold electron temperature for five events are presented in Table 6.2. The table includes the date and time of the events, the radial distance, the magnetic local time (MLT), and the magnetic latitude, respectively.

Table 6.2: Cold electron temperatures estimated from the method proposed in this study

Event Date and Time	Radial distance (R_E)	Magnetic local time (MLT)	Magnetic latitude (degree)	Maximum temperature (eV)	Estimated temperature (eV)
2019-09-11/04:40	6.1	6.0	0.1	5	3
2019-09-13/14:46	5.4	6.6	−0.3	10	5
2019-09-14/09:52	5.3	6.7	0.2	50	5
2019-09-15/20:52	5.9	5.1	−2.4	50	7
2019-09-16/16:50	6.0	5.5	−1.0	20	5

At the time of these events, the Arase satellite was located at an altitude of about $6R_E$, on the morning side, near the magnetic equator. Estimated temperatures at these events range from 3 eV to 7 eV, and all of them are on the order of 1 eV.

The low-energy electron temperatures were on the order of 1 eV for many of the events analyzed. The only event analyzed that differed was the event on 2019-09-09/16:37. The electric field spectrum, phase difference, apparent phase velocity, and spin angle for this event are shown in Figure 6.4. The dispersion relation is shown in Figure 6.5. The purple line in the figure is the dispersion curve calculated with the parameters shown in the Table 6.3 upper half, and the blue line is the dispersion curve for the parameters shown in the Table 6.3 lower half. The waves occurring in the frequency band of f_{ce} to $1.4f_{\text{ce}}$ are not always obtained during the observation period, and the waves do not exist continuously for one spin. The purple line in the figure was obtained by prioritizing the agreement at $1.6f_{\text{ce}}$, which is the maximum intensity, and therefore the low-energy electrons in this event were set to 30 eV. This value is about 10 times larger than the low-energy electron temperature in other events. However, if the waves are observed during the half of spin period, it is possible to estimate the wave vector direction and determine the phase velocity by fitting. The analysis is based on the condition that the wave is continuously observed for more than 1/2 spin period, and the frequency band of f_{ce} to $1.4f_{\text{ce}}$ is also observed for more than 1/2 spin period. Considering that this part of the spectrum follows the dispersion curve, the matching dispersion curve is the blue line in the figure. The estimated low-energy electron temperature is 9 eV. The low-energy electron temperature estimated here is close to the low-energy electron temperatures in other events.

Another event for which multiple background electron temperatures are similarly estimated is the event 2019-09-15/20:52. The dispersion relation obtained for the event 2019-09-15/20:52 is shown in Figure 6.6. The first condition is that the dispersion curve passes through +, which shows the dispersion relation at the intensity peak in each frequency band, and then the theoretical dispersion curve is selected to match the observations at more frequencies. Therefore, although this event is shown as 7 eV, there are angular frequencies in the f_{ce} to $2f_{\text{ce}}$, $2f_{\text{ce}}$ to $3f_{\text{ce}}$, and 4 to $5f_{\text{ce}}$ frequency bands where $k \sim 0.01$ /m exists. Considering these points along the dispersion curves, the matching dispersion curve has the parameters shown in the table, and the background electron temperature is estimated to be 50 eV.

When the wavenumbers for these events have small wavenumbers and high background electron temperatures, we find that there are simultaneously frequencies with relatively large wavenumbers. In addition, checking the electric field spectra before and after shows that peaks often arise and disappear for frequencies with small wavenumbers.

Therefore, it was inferred that this was the arrival and decay of ECH waves generated elsewhere. In these two events, it is proposed that there are two nearby regions with low-energy electron temperatures on the order of 10 eV and 1 eV, and that the ECH waves generated in

Table 6.3: Parameters used for computation of dispersion curves by KUPDAP

Particles	density($10^6/\mathrm{m}^3$)	$T_\parallel$(eV)	$T_\perp$(eV)
e	0.182	95.6	253
e_{cold}	4.28	$30/\sqrt{2}$	$30/\sqrt{2}$
H^+	4.46	$1/\sqrt{2}$	$1/\sqrt{2}$
e	0.182	95.6	253
e_{cold}	4.28	$9/\sqrt{2}$	$9/\sqrt{2}$
H^+	4.46	$1/\sqrt{2}$	$1/\sqrt{2}$

Table 6.4: Percentage of hot electron density at each event

Event Date and Time	Estimated temperature (eV)	n/n_e (%)
2019-09-09/16:37	30	4.08
2019-09-11/04:40	3	0.98
2019-09-13/14:46	5	1.71
2019-09-14/09:52	5	0.27
2019-09-15/20:52	7	2.68
2019-09-16/16:50	5	4.53

these regions arrive at the same time.

The error in the obtained low-energy electron temperatures was examined. There are three possible sources of error. The first is that the UHR frequency was roughly estimated from the electric field spectrum. If the UHR were not read correctly, the total number of electrons would change. To estimate the error, we calculated the ratio of the total electron density to the hot electron density for each event. The results are shown in the Table 6.4.

In all events, the ratio of hot electrons was less than 5 percent. In this case, since the cold electrons are dominant, only the background electron temperature has a significant effect on the dispersion curve. This suggests that the effect of errors in reading the UHR frequency is very small.

Second, the wavenumber vector direction was estimated assuming a propagation angle of 90 degrees. When the growth rate was calculated by KUPDAP, it was shown that the maximum growth rate was about 88.5 degrees. The estimated wavenumber vector direction is almost unchanged compared to the case where 90 degrees is assumed.

Finally, the effective length of the antennas is assumed to be the midpoint of each antenna. The distance between the midpoints of two antennas is taken as the distance between the antennas. When a static wave reaches the antenna, the effective length may be larger or smaller than the distance between the antennas. If we assume that the change is not so large, we can say that the temperature of low-energy electrons, which occupy more than 95 % of the inner magnetosphere, is on the order of about 1 eV.

6.5 Discussion and summary

We analyzed six events of the interferometry observation of ECH waves by the Arase satellite. The cold electron temperature from 1.9 eV to 7 eV is obtained from the analysis. At the time of these observations, the Arase satellite was at an altitude of approximately 6 R_E,

The ratio of observed to calculated total electron density during these events was at most 4.53 percent, and all others were less than 3 percent. As noted in Kurth et al. (2014), it is difficult to correctly determine the UHR frequency and there are uncertainties in the total electron density, but it is possible to remark that the low-energy electron temperature is dominant in these regions.

It is also noted that the effective length of the antenna is assumed to be the midpoint of the antenna in this analysis. There is a possibility of variations in the effective length when observing electrostatic waves[71]. Additionally, in the estimation of the wave vector, we assumed a wave normal angle of 90 degrees, although the wave normal angle for the ECH wave is most likely around 88 degrees to 89.9 degrees from the dispersion relation. However, it is considered that the error in the estimated cold electron temperature due to variations in the wave normal angle is not substantial.

In this study, the phase velocity of ECH waves was determined using the interferometry observation mode of the Arase satellite, and this allowed us to calculate the $\omega - k$ relationship. Using LEP-e, the electron temperature and electron density within the observed range were determined. From HFA and OFA observation, we detected the UHR frequencies and estimated the total electron density. We estimated the cold electron density by them and swept the temperature to find a value consistent with the observed dispersion relation. Estimations were performed for 6 events, all of which were in the order of 1 eV. The analysis assumes propagation angle and effective length and has errors in estimating the wave vector. However, the observation and dispersion curves agree at most frequencies, and this reliability is considered high.

It was found that the wavenumber may be as small as 0.01 /m in some frequency bands for a few events. There are two possibilities for these events. The first reason is that the observed region may be a combination of regions with different low-energy electron temperatures. The group velocity of ECH waves is considered to be very small because they are longitudinal waves, but it is possible that multiple waves with different origins are observed at the same time if the region is finely interpenetrated. This is also consistent with the intermittent observation of waves in frequency bands with larger wavenumbers in ECH events near 16:37:18 on 9 September 2019. Gao et al. [72] discussed the possibility of waves being excited to new frequency bands by wave-wave interaction in ECH waves. Although it is conceivable that the waves observed intermittently could be excited by wave-wave interaction, the frequency bands excited by waves in these two events, unlike the example described in Gao et al. [72], do not consist of simple sums and subtractions, and thus may not be due to wave-wave interaction. Also, since the wave vector varies with frequency, it is possible that a dispersion relationship such as the one shown in Figure 6.5 and Figure 6.6 can be read at the timing of the arrival of multiple waves.

The second possibility is that the effective length of the antenna in interferometry observations may actually differ. Since ECH waves are compressional wave, they may change the effective length of the antennas[71], but the change in effective length depends on the wavenumber of the arriving waves, and it is not clear whether the effective length changed during this event. In this study, the distance between antennas was calculated as the distance between the midpoints of the antennas. If the effective length of the antennas were shorter for some frequency bands, the wavenumber would appear smaller.

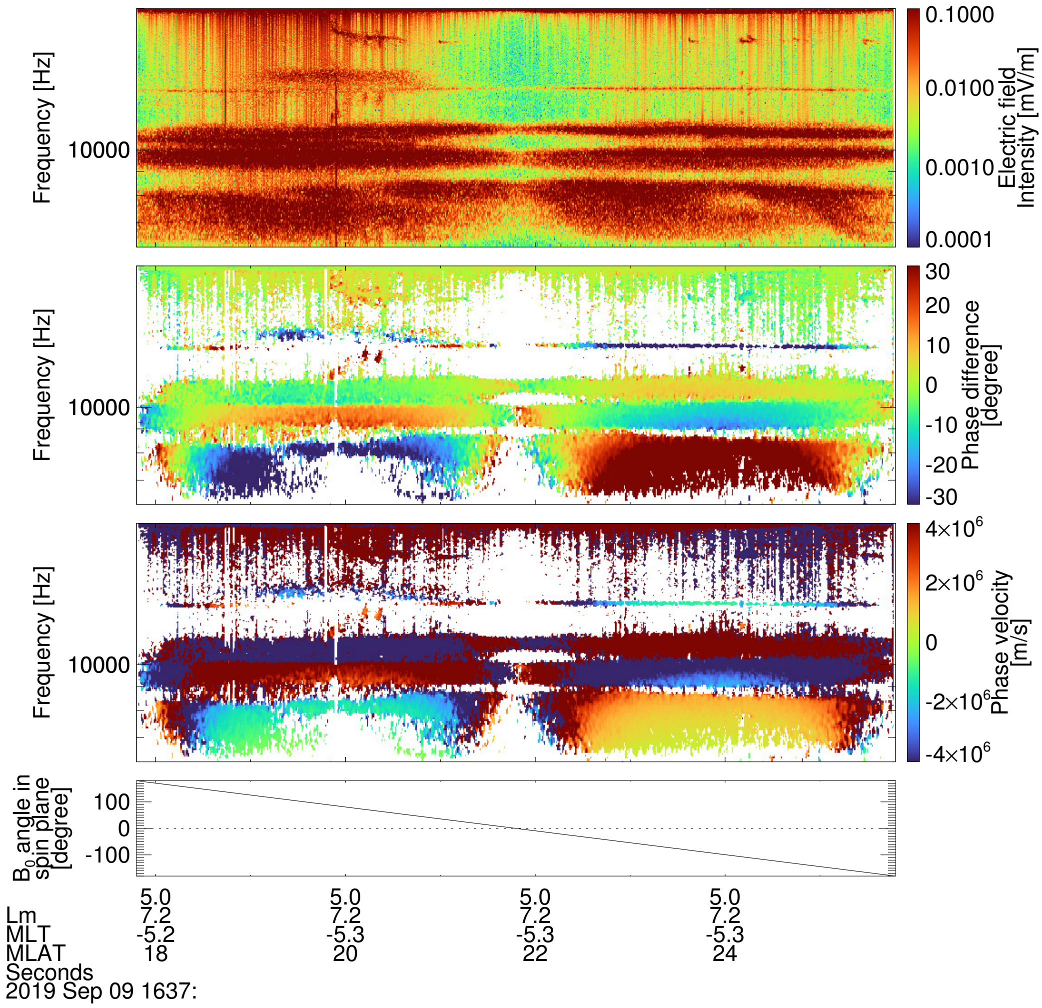

Figure 6.4: ECH events near 16:37:18 on 9 September 2019. For each part, from top: (a)dynamic spectrum of E_{V1}, (b)phase difference between E_{V1} and E_{V2} at times and frequencies with high coherence, (c)the calculated apparent phase velocity v'_{ph}, (d)angle between the antenna V1 and the background magnetic field projected onto the spin plane

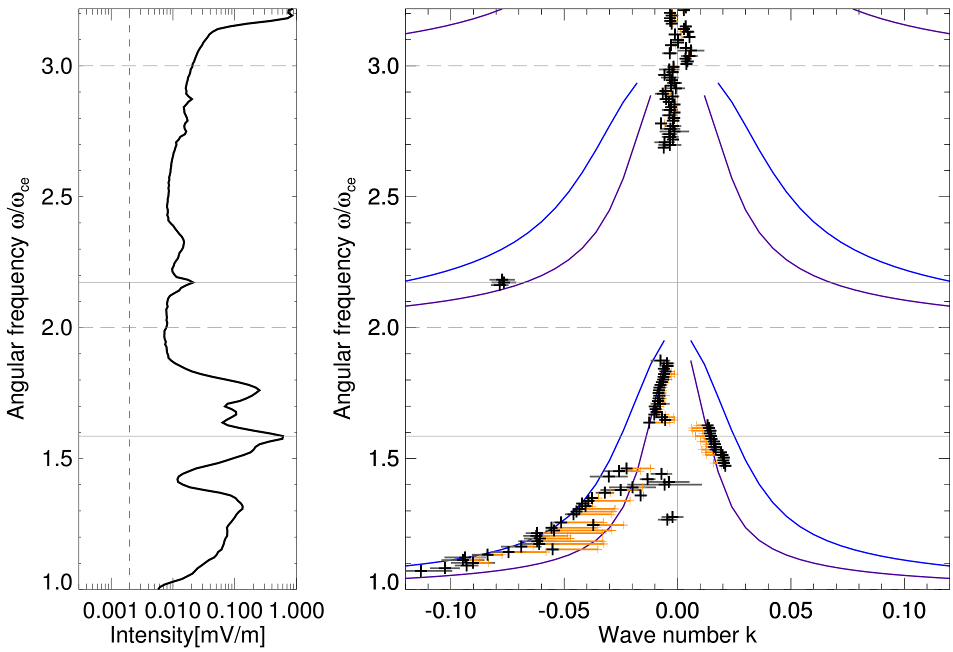

Figure 6.5: The electric field intensity and dispersion relation for ECH events near 16:37 on 9 September 2019.

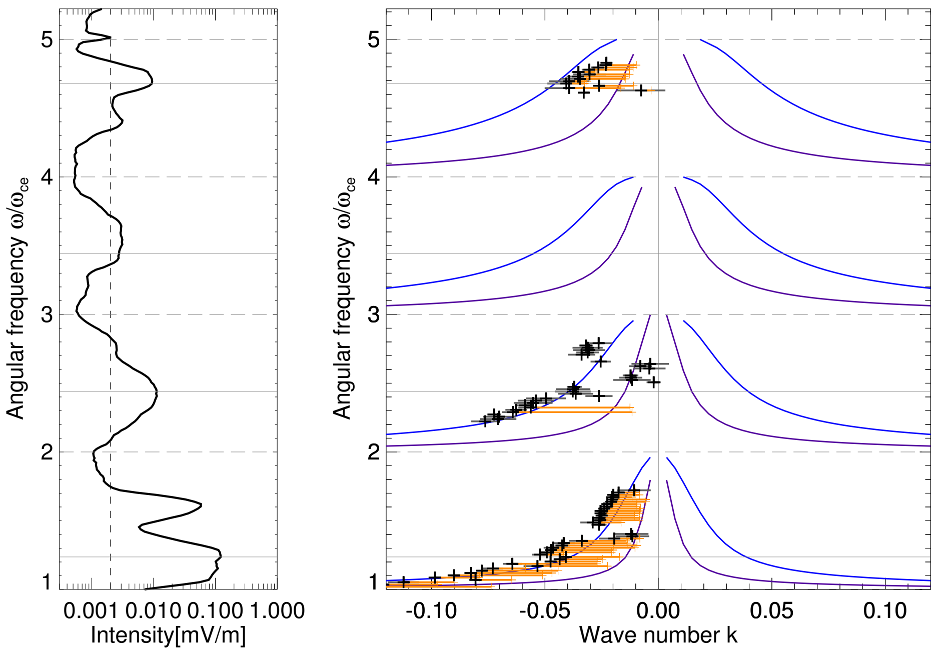

Figure 6.6: The electric field intensity and dispersion relation for ECH events near 20:52 on 15 September 2019.

Chapter 7

Summary and conclusion

7.1 Summary of this thesis

The electric field waveforms observed by interferometry on the Arase satellite are analyzed.

Chapter 1 describes the significance of satellite observations in the Earth's magnetosphere and an overview of interferometry observations. Arase satellite is a single interferometry observation satellite.

Chapter 2 describes the instruments used on the Arase satellite and the analysis method of the interferometry observation data.

In Chapter 3, the time differences were calculated by analyzing the electric field waveforms of the electrostatic solitary wave observed by the Arase satellite. The spatial scale of the corresponding isolated potential was calculated and shown to be from several hundred meters to several kilometers. Based on the characteristics of the waveform of the electrostatic solitary wave, we proposed a two-dimensional Gaussian model for the solitary potential in the inner magnetosphere, and reproduced the characteristics of the observed waveform by numerical simulation. Although a potential structure with net potential was proposed by the RBSP satellite for isolated potentials in the Earth's inner magnetosphere, the results of this study suggest that it is possible to reproduce the observed waveforms with other structures. It is expected that the scale of the potential structure will be smaller in the inner magnetosphere, where the magnetic field intensity is larger than that of the magnetotail region observed by the GEOTAIL satellite. In addition, the RBSP satellite model is interpreted as a sheet-like structure with various net potentials, but the two-dimensional Gaussian structure proposed in this study reproduces various waveforms by the passage of a single structure. Therefore, it is quite possible that these structures actually occur in the inner magnetosphere.

In Chapter 4, we analyzed the chorus waveforms observed by the Arase satellite and calculated the phase differences. The spin dependence of the obtained phase differences is explained, and an interferometry observation model of chorus waves is developed. Based on the observations of the chorus wave, the upper and lower limits of the phase velocity that can be observed by interferometry observations are presented.

In Chapter 5, we performed an analysis on ECH wave observed by the Arase satellite and calculated the phase difference and apparent phase speed. The spin dependence of the phase difference was explained and the interferometry observation model of ECH wave was developed to reproduce the spin dependence numerically. By comparing the spin dependence of the phase difference for different frequencies, we showed that the wave vector direction of ECH wave is different for different frequencies.

In Chapter 6, we proposed a method to estimate the unobserved component of the wave number vector using an observational model of ECH wave. Whereas the Arase satellite observation provides only instantaneous one-dimensional electric field waveforms, the analysis makes it possible to identify the three-dimensional direction of the ECH wave vectors. The phase velocity was calculated using the wave vector estimated by the method, and the dispersion relation was derived. It was shown that the dispersion relation obtained from the observation is consistent with the theoretical dispersion curve, and the low-energy electron temperature, which was an unknown parameter, was successfully estimated from the dispersion relation. It is shown that the low-energy electron temperature in the Earth's inner magnetosphere is on the order of 1 eV. Since low-energy electron temperatures cannot be observed with particle instruments, this study was the first to estimate low-energy electron temperatures by observing ECH waves.

7.2 Suggestions for future studies

In this study, we calculated the velocity and spatial scale of waves and solitary potentials using interferometry observations from the Arase satellite. We estimated the presence and structure of solitary electrostatic potentials, as well as the wave vector of ECH waves and the inferred low-energy electron temperature in the Arase satellite orbit. In Chapter 3, we estimated that the plasma density fluctuations exist on the order of hundreds of meters to several kilometers in scale. Such density structures observed by the GEOTAIL satellite were shown to be generated by nonlinear growth of electrostatic waves[73]. It is necessary to investigate whether similar density structures are generated on this scale.

Since the ESW provides various electric field waveforms in the parallel and perpendicular directions, it was not possible to determine the polarity of the potential from one-dimensional interferometry observations. Simultaneous parallel and perpendicular interferometry observations would allow more precise determination of the polarity of the potentials. Additionally, if interferometry observations that can obtain data in multiple directions simultaneously are conducted in the future, we can expect to clarify the detailed scales of these structures in both the perpendicular and horizontal directions relative to the background magnetic field.

The relationship between phase velocity and sampling frequency presented in Chapter 4 will be important for future satellite observations. Chapters 5 and 6 demonstrated the wave vector of ECH waves. The fact that the wave vectors at each peak frequency of ECH waves are not always consistent is a significant result. Moreover, the presence of multiple peaks in the fundamental wave suggests the possibility that ECH waves are arriving simultaneously from multiple sources. This possibility can be more thoroughly understood through longer continuous wave observations and simultaneous multi-point observations with multiple satellites.

In Chapter 6, we estimated the low-energy electron temperature from the dispersion relation of ECH waves. Low-energy electrons are difficult to observe directly with particle detectors, and the discussion in this study, which estimated low-energy electron temperature from waves, provides an important clue. On the other hand, systems that can directly observe low-energy particles are being considered through methods such as satellite charging observations or control. If observations are conducted using satellites equipped with such instruments, it is expected that a more accurate understanding of the low-energy electron temperature distribution can be obtained.

Bibliography

[1] LM Kistler, K Asamura, S Kasahara, Y Miyoshi, CG Mouikis, K Keika, SM Petrinec, ML Stevens, T Hori, S Yokota, et al. The variable source of the plasma sheet during a geomagnetic storm. Nature Communications, 14(1):6143, 2023.

[2] Vytenis M Vasyliunas. A survey of low-energy electrons in the evening sector of the magnetosphere with ogo 1 and ogo 3. Journal of Geophysical Research, 73(9):2839–2884, 1968.

[3] GP Serbu and EJR Maier. Observations from ogo 5 of the thermal ion density and temperature within the magnetosphere. Journal of Geophysical Research, 75(31):6102–6113, 1970.

[4] Kazuhiro AIKYO, Tadahiko OGAWA, and Iwao IWAMOTO. Observations of the magnetosphere and ionosphere by dynamics explorer satellite 2. brief description of dynamics explorer program. Review of the Radio Research Laboratory, 33(169):205–212, 1987.

[5] P. M. E. Décréau, S. Kougblénou, G. Lointier, J.-L. Rauch, J.-G. Trotignon, X. Vallières, P. Canu, S. Rochel Grimald, F. El-Lemdani Mazouz, and F. Darrouzet. Remote sensing of a ntc radio source from a cluster tilted spacecraft pair. Annales Geophysicae, 31(11): 2097–2121, 2013. doi: 10.5194/angeo-31-2097-2013.

[6] James L Burch and Vassilis Angelopoulos. The THEMIS mission. Springer Science & Business Media, 2009.

[7] JB Tao, RE Ergun, DL Newman, JS Halekas, L Andersson, V Angelopoulos, JW Bonnell, JP McFadden, Christopher M Cully, H-U Auster, et al. Kinetic instabilities in the lunar wake: Artemis observations. Journal of Geophysical Research: Space Physics, 117(A3), 2012.

[8] AR Poppe, JS Halekas, GT Delory, WM Farrell, V Angelopoulos, JP McFadden, JW Bonnell, and RE Ergun. A comparison of artemis observations and particle-in-cell modeling of

the lunar photoelectron sheath in the terrestrial magnetotail. Geophysical research letters, 39(1), 2012.

[9] H Matsumoto, H Kojima, T Miyatake, Y Omura, M Okada, I Nagano, and M Tsutsui. Electrostatic solitary waves (esw) in the magnetotail: Ben wave forms observed by geotail. Geophysical Research Letters, 21(25):2915–2918, 1994.

[10] H Kojima, Y Omura, H Matsumoto, K Miyaguti, and T Mukai. Characteristics of electrostatic solitary waves observed in the plasma sheet boundary: Statistical analyses. Nonlinear Processes in Geophysics, 6(3/4):179–186, 1999.

[11] FS Mozer, SD Bale, JW Bonnell, CC Chaston, I Roth, and J Wygant. Megavolt parallel potentials arising from double-layer streams in the earth's outer radiation belt. Physical review letters, 111(23):235002, 2013.

[12] AV Artemyev, OV Agapitov, F Mozer, and V Krasnoselskikh. Thermal electron acceleration by localized bursts of electric field in the radiation belts. Geophysical Research Letters, 41(16):5734–5739, 2014.

[13] Xiangrong Fu. Double layer–a particle accelerator in the magnetosphere. Technical report, Los Alamos National Lab.(LANL), Los Alamos, NM (United States), 2015.

[14] H Kojima, H Matsumoto, and Y Omura. Electrostatic solitary waves observed in the geomagnetic tail and other regions. Advances in Space Research, 23(10):1689–1697, 1999.

[15] J Bortnik, RM Thorne, and NP Meredith. Modeling the propagation characteristics of chorus using crres suprathermal electron fluxes. Journal of Geophysical Research: Space Physics, 112(A8), 2007.

[16] Yi-Kai Hsieh and Yoshiharu Omura. Nonlinear dynamics of electrons interacting with oblique whistler mode chorus in the magnetosphere. Journal of Geophysical Research: Space Physics, 122(1):675–694, 2017.

[17] Jinxing Li, Jacob Bortnik, Xin An, Wen Li, Vassilis Angelopoulos, Richard M Thorne, Christopher T Russell, Binbin Ni, Xiaochen Shen, William S Kurth, et al. Origin of two-band chorus in the radiation belt of earth. Nature communications, 10(1):4672, 2019.

[18] Donald A. Gurnett and Amitava Bhattacharjee. Introduction to Plasma Physics. Cambridge University Press, 2005.

[19] Nigel P Meredith, Richard B Horne, Richard M Thorne, and Roger R Anderson. Survey of upper band chorus and ech waves: Implications for the diffuse aurora. Journal of Geophysical Research: Space Physics, 114(A7), 2009.

[20] CF Kennel, FL Scarf, RW Fredricks, JH McGehee, and FV Coroniti. Vlf electric field observations in the magnetosphere. Journal of Geophysical Research, 75(31):6136–6152, 1970.

[21] Hiroshi Oya. Plasma flow hypothesis in the magnetosphere relating to frequency shift of electrostatic plasma waves. Journal of Geophysical Research, 80(19):2783–2789, 1975.

[22] Atsuki Shinbori, Takayuki Ono, M Iizima, A Kumamoto, S Shirai, A Hanaoka, K Okamoto, M Ohashi, and H Oya. Electrostatic electron cyclotron harmonic waves observed by the akebono satellite near the equatorial region of the plasmasphere. Earth, planets and space, 59(6):613–629, 2007.

[23] JD Menietti, YY Shprits, RB Horne, EE Woodfield, GB Hospodarsky, and DA Gurnett. Chorus, ech, and z mode emissions observed at jupiter and saturn and possible electron acceleration. Journal of Geophysical Research: Space Physics, 117(A12), 2012.

[24] Michel Moncuquet, Nicole Meyer-Vernet, and Sang Hoang. Dispersion of electrostatic waves in the io plasma torus and derived electron temperature. Journal of Geophysical Research: Space Physics, 100(A11):21697–21708, 1995.

[25] RW Fredricks and FL Scarf. Recent studies of magnetospheric electric field emissions above the electron gyrofrequency. Journal of Geophysical Research, 78(1):310–314, 1973.

[26] Satoshi Kurita, Yoshizumi Miyoshi, Christopher M Cully, Vassilis Angelopoulos, Olivier Le Contel, Mitsuru Hikishima, and Hiroaki Misawa. Observational evidence of electron pitch angle scattering driven by ech waves. Geophysical Research Letters, 41 (22):8076–8080, 2014.

[27] Xiaojia Zhang and Vassilis Angelopoulos. On the relationship of electrostatic cyclotron harmonic emissions with electron injections and dipolarization fronts. Journal of Geophysical Research: Space Physics, 119(4):2536–2549, 2014.

[28] Mizuki Fukizawa, Takeshi Sakanoi, Yoshizumi Miyoshi, Keisuke Hosokawa, Kazuo Shiokawa, Yuto Katoh, Yoichi Kazama, Atsushi Kumamoto, Fuminori Tsuchiya, Yukinaga Miyashita, et al. Electrostatic electron cyclotron harmonic waves as a candidate to cause pulsating auroras. Geophysical Research Letters, 45(23):12–661, 2018.

[29] Yoshiya Kasahara, Yasumasa Kasaba, Hirotsugu Kojima, Satoshi Yagitani, Keigo Ishisaka, Atsushi Kumamoto, Fuminori Tsuchiya, Mitsunori Ozaki, Shoya Matsuda, Tomohiko Imachi, et al. The plasma wave experiment (pwe) on board the arase (erg) satellite. Earth, Planets and Space, 70(1):1–28, 2018.

[30] Ayako Matsuoka, Mariko Teramoto, Reiko Nomura, Masahito Nosé, Akiko Fujimoto, Yoshimasa Tanaka, Manabu Shinohara, Tsutomu Nagatsuma, Kazuo Shiokawa, Yuki Obana, et al. The arase (erg) magnetic field investigation. Earth, Planets and Space, 70(1):1–16, 2018.

[31] Yasumasa Kasaba, Keigo Ishisaka, Yoshiya Kasahara, Tomohiko Imachi, Satoshi Yagitani, Hirotsugu Kojima, Shoya Matsuda, Masafumi Shoji, Satoshi Kurita, Tomoaki Hori, et al. Wire probe antenna (wpt) and electric field detector (efd) of plasma wave experiment (pwe) aboard the arase satellite: specifications and initial evaluation results. Earth, Planets and Space, 69(1):1–18, 2017.

[32] Shoya Matsuda, Yoshiya Kasahara, Hirotsugu Kojima, Yasumasa Kasaba, Satoshi Yagitani, Mitsunori Ozaki, Tomohiko Imachi, Keigo Ishisaka, Atsushi Kumamoto, Fuminori Tsuchiya, et al. Onboard software of plasma wave experiment aboard arase: Instrument management and signal processing of waveform capture/onboard frequency analyzer. Earth, Planets and Space, 70(1):1–22, 2018.

[33] Mitsunori Ozaki, Satoshi Yagitani, Yoshiya Kasahara, Hirotsugu Kojima, Yasumasa Kasaba, Atsushi Kumamoto, Fuminori Tsuchiya, Shoya Matsuda, Ayako Matsuoka, Takashi Sasaki, et al. Magnetic search coil (msc) of plasma wave experiment (pwe) aboard the arase (erg) satellite. Earth, Planets and Space, 70(1):1–13, 2018.

[34] Atsushi Kumamoto, Fuminori Tsuchiya, Yoshiya Kasahara, Yasumasa Kasaba, Hirotsugu Kojima, Satoshi Yagitani, Keigo Ishisaka, Tomohiko Imachi, Mitsunori Ozaki, Shoya Matsuda, et al. High frequency analyzer (hfa) of plasma wave experiment (pwe) onboard the arase spacecraft. Earth, Planets and Space, 70(1):1–14, 2018.

[35] Y Omura, H Kojima, and H Matsumoto. Computer simulation of electrostatic solitary waves: A nonlinear model of broadband electrostatic noise. Geophysical research letters, 21(25):2923–2926, 1994.

[36] M Temerin, K Cerny, W Lotko, and FS Mozer. Observations of double layers and solitary waves in the auroral plasma. Physical Review Letters, 48(17):1175, 1982.

[37] Scott R Bounds, Robert F Pfaff, Stephen F Knowlton, Forrest S Mozer, Michael A Temerin, and Craig A Kletzing. Solitary potential structures associated with ion and elec-

tron beams near 1re altitude. Journal of Geophysical Research: Space Physics, 104(A12): 28709–28717, 1999.

[38] J Dombeck, C Cattell, J Crumley, WK Peterson, HL Collin, and C Kletzing. Observed trends in auroral zone ion mode solitary wave structure characteristics using data from polar. Journal of Geophysical Research: Space Physics, 106(A9):19013–19021, 2001.

[39] FS Mozer, OV Agapitov, A Artemyev, JF Drake, V Krasnoselskikh, S Lejosne, and I Vasko. Time domain structures: What and where they are, what they do, and how they are made. Geophysical Research Letters, 42(10):3627–3638, 2015.

[40] JS Pickett. A review of electrostatic solitary wave research from the cluster mission. Journal of Geophysical Research: Space Physics, 126(9):e2021JA029548, 2021.

[41] FS Mozer, OA Agapitov, A Artemyev, JL Burch, RE Ergun, BL Giles, D Mourenas, RB Torbert, TD Phan, and I Vasko. Magnetospheric multiscale satellite observations of parallel electron acceleration in magnetic field reconnection by fermi reflection from time domain structures. Physical Review Letters, 116(14):145101, 2016.

[42] FS Mozer, A Artemyev, OV Agapitov, D Mourenas, and I Vasko. Near-relativistic electron acceleration by landau trapping in time domain structures. Geophysical Research Letters, 43(2):508–514, 2016.

[43] H Kojima, K Ohtsuka, H Matsumoto, Y Omura, RR Anderson, Y Saito, T Mukai, S Kokubun, and T Yamamoto. Plasma waves in slow-mode shocks observed by geotail spacecraft. Advances in Space Research, 24(1):51–54, 1999.

[44] Stephen R Mosier and Donald A Gurnett. Theory of the injun 5 very-low-frequency poynting flux measurements. Journal of Geophysical Research, 76(4):972–977, 1971.

[45] O Santolík and DA Gurnett. Transverse dimensions of chorus in the source region. Geophysical Research Letters, 30(2), 2003.

[46] Naoshin Haque, M Spasojevic, O Santolík, and US Inan. Wave normal angles of magnetospheric chorus emissions observed on the polar spacecraft. Journal of Geophysical Research: Space Physics, 115(A4), 2010.

[47] W Li, RM Thorne, J Bortnik, YY Shprits, Y Nishimura, V Angelopoulos, C Chaston, Olivier Le Contel, and JW Bonnell. Typical properties of rising and falling tone chorus waves. Geophysical Research Letters, 38(14), 2011.

[48] M Ashour-Abdalla and CF Kennel. Nonconvective and convective electron cyclotron harmonic instabilities. Journal of Geophysical Research: Space Physics, 83(A4):1531–1543, 1978.

[49] Hiroshi Oya, Akira Morioka, Kaori Kobayashi, Masahide Iizima, Takayuki Ono, Hiroshi Miyaoka, Toshimi Okada, and Takahiro Obara. Plasma wave observation and sounder experiments (pws) using the akebono (exos-d) satellite instrumentation and initial results including discovery of the high altitude equatorial plasma turbulence. Journal of geomagnetism and geoelectricity, 42(4):411–442, 1990.

[50] W Li, J Bortnik, Y Nishimura, RM Thorne, and V Angelopoulos. The origin of pulsating aurora: Modulated whistler mode chorus waves. Auroral phenomenology and magnetospheric processes: Earth and other planets, 197:379–388, 2012.

[51] Binbin Ni, Richard Thorne, Jun Liang, Vassilis Angelopoulos, Chris Cully, Wen Li, Xiaojia Zhang, Michael Hartinger, Olivier Le Contel, and Alain Roux. Global distribution of electrostatic electron cyclotron harmonic waves observed on themis. Geophysical Research Letters, 38(17), 2011.

[52] Richard F Hubbard and Thomas J Birmingham. Electrostatic emissions between electron gyroharmonics in the outer magnetosphere. Journal of Geophysical Research: Space Physics, 83(A10):4837–4850, 1978.

[53] RF Hubbard, TJ Birmingham, and EW Hones Jr. Magnetospheric electrostatic emissions and cold plasma densities. Journal of Geophysical Research: Space Physics, 84(A10): 5828–5838, 1979.

[54] Daniel B Graham, Yu V Khotyaintsev, Andris Vaivads, and Mats Andre. Electrostatic solitary waves and electrostatic waves at the magnetopause. Journal of Geophysical Research: Space Physics, 121(4):3069–3092, 2016.

[55] Yoshizumi Miyoshi, Iku Shinohara, Takeshi Takashima, Kazushi Asamura, Nana Higashio, Takefumi Mitani, Satoshi Kasahara, Shoichiro Yokota, Yoichi Kazama, Shiang-Yu Wang, et al. Geospace exploration project erg. Earth, Planets and Space, 70(1):1–13, 2018.

[56] Qinghua Zhou, Fuliang Xiao, Chang Yang, Si Liu, Yihua He, DN Baker, HE Spence, Geoffrey D Reeves, and Herbert O Funsten. Generation of lower and upper bands of electrostatic electron cyclotron harmonic waves in the van allen radiation belts. Geophysical Research Letters, 44(11):5251–5258, 2017.

[57] RB Horne, RM Thorne, NP Meredith, and RR Anderson. Diffuse auroral electron scattering by electron cyclotron harmonic and whistler mode waves during an isolated substorm. Journal of Geophysical Research: Space Physics, 108(A7), 2003.

[58] Binbin Ni, Richard M Thorne, Richard B Horne, Nigel P Meredith, Yuri Y Shprits, Lunjin Chen, and Wen Li. Resonant scattering of plasma sheet electrons leading to diffuse auroral precipitation: 1. evaluation for electrostatic electron cyclotron harmonic waves. Journal of Geophysical Research: Space Physics, 116(A4), 2011.

[59] DJ McComas, SJ Bame, BL Barraclough, JR Donart, RC Elphic, JT Gosling, MB Moldwin, KR Moore, and MF Thomsen. Magnetospheric plasma analyzer: Initial three-spacecraft observations from geosynchronous orbit. Journal of Geophysical Research: Space Physics, 98(A8):13453–13465, 1993.

[60] DA Bryant, DS Hall, and DR Lepine. Electron acceleration in an array of auroral arcs. Planetary and Space Science, 26(1):81–92, 1978.

[61] T Ono and Y Miyoshi. Solar Terrestrial and Space Plasma Physics (Taiyo chikyu ken). 2012.

[62] Yoichi Kazama, Bo-Jhou Wang, Shiang-Yu Wang, Paul TP Ho, Sunny WY Tam, Tzu-Fang Chang, Chih-Yu Chiang, and Kazushi Asamura. Low-energy particle experiments–electron analyzer (lepe) onboard the arase spacecraft. Earth, Planets and Space, 69:1–13, 2017.

[63] Mats André and Christopher M Cully. Low-energy ions: A previously hidden solar system particle population. Geophysical Research Letters, 39(3), 2012.

[64] Gian Luca Delzanno, Joseph E Borovsky, Michael G Henderson, Pedro Alberto Resendiz Lira, Vadim Roytershteyn, and Daniel T Welling. The impact of cold electrons and cold ions in magnetospheric physics. Journal of Atmospheric and Solar-Terrestrial Physics, 220:105599, 2021.

[65] WS Kurth, S De Pascuale, JB Faden, CA Kletzing, GB Hospodarsky, S Thaller, and JR Wygant. Electron densities inferred from plasma wave spectra obtained by the waves instrument on van allen probes. Journal of Geophysical Research: Space Physics, 120(2): 904–914, 2015.

[66] Chao Yue, Yuxuan Li, Lynn Kistler, Qianli Ma, Haobo Fu, Geoffrey D Reeves, Xuzhi Zhou, Qiugang Zong, and Harlan E Spence. The densities and compositions of background cold ions based on the van allen probe observations. Geophysical Research Letters, 50(15):e2023GL104282, 2023.

[67] F Leuterer. Cyclotron harmonic waves in an inhomogeneous plasma. ii. experiment. Plasma Physics, 14(5):499, 1972.

[68] DD Barbosa and WS Kurth. On the generation of plasma waves in saturn's inner magnetosphere. Journal of Geophysical Research: Space Physics, 98(A6):9351–9356, 1993.

[69] Yifan Wu, Xin Tao, Xu Liu, Lunjin Chen, Huasheng Xie, Kaijun Liu, and B Horne, Richard. Particle-in-cell simulation of electron cyclotron harmonic waves driven by a loss cone distribution. Geophysical Research Letters, 47(9):e2020GL087649, 2020.

[70] Hajime Sugiyama, Satyavir Singh, Yoshiharu Omura, Masafumi Shoji, David Nunn, and Danny Summers. Electromagnetic ion cyclotron waves in the earth's magnetosphere with a kappa-maxwellian particle distribution. Journal of Geophysical Research: Space Physics, 120(10):8426–8439, 2015.

[71] Konrad Steinvall, Yu V Khotyaintsev, and Daniel B Graham. On the applicability of single-spacecraft interferometry methods using electric field probes. Journal of Geophysical Research: Space Physics, 127(3):e2021JA030143, 2022.

[72] Zhonglei Gao, Pingbing Zuo, Xueshang Feng, Yi Wang, Chaowei Jiang, and Fengsi Wei. Evidence of nonlinear interactions between magnetospheric electron cyclotron harmonic waves. Geophysical Research Letters, 47(16):e2020GL088452, 2020.

[73] Y Omura, H Matsumoto, T Miyake, and H Kojima. Electron beam instabilities as generation mechanism of electrostatic solitary waves in the magnetotail. Journal of Geophysical Research: Space Physics, 101(A2):2685–2697, 1996.

Publication list

Journal papers

1. Tomoe Taki, Satoshi Kurita, Airi Shinjo, Satoko Nakamura, Hirotsugu Kojima, Yoshiya Kasahara, Shoya Matsuda, Ayako Matsuoka, Yoshizumi Miyoshi, and Iku Shinohara, "Phase Difference of Electron Cyclotron Harmonic (ECH) Waves Observed by Using the Interferometry Observation Mode of the Arase Satellite," URSI Radio Science Letters, 4, 46, 2023. (Chapter 5)

2. Tomoe Taki, Satoshi Kurita, Hirotsugu Kojima, Yoshiya Kasahara, Shoya Matsuda, Ayako Matsuoka, Yoichi Kazama, Chae-Woo Jun, Shiang-Yu Wang, Sunny W. Y. Tam, Tzu-Fang Chang, Bo-Jhou Wang, Yoshizumi Miyoshi, and Iku Shinohara, "Cold electron temperature in the inner magnetosphere estimated through the dispersion relation of ECH waves from the Arase satellite observations," Radio Science, 59(6), e2023RS007927. (Chapter 6)

3. Tomoe Taki, Satoshi Kurita, Airi Shinjo, Ibuki Fukasawa, Satoko Nakamura, Hirotsugu Kojima, Yoshiya Kasahara, Shoya Matsuda, Ayako Matsuoka, Yoshizumi Miyoshi, and Iku Shinohara, "On the phase difference of ECH waves obtained from the interferometry observation by the Arase satellite," Earth, Planets and Space, 76.1: 106, 2024. (Chapter 5)

Peer-reviewed proceedings in international conference

1. Tomoe Taki, Satoshi Kurita, Hirotsugu Kojima, Yoshiya Kasahara, Yoshizumi Miyoshi, Ayako Matsuoka and Shoya Matsuda, "Isolated Electrostatic Potentials Observed by the Arase Satellite," in *URSI GASS*, Online-session, 2021.

Other presentations in international conference

1. Tomoe Taki, Hirotsugu Kojima, Yoichi Kazama, Yoshiya Kasahara, Yoshizumi Miyoshi, Iku Shinohara, Hideyuki Usui, Wang S.-Y., Tam Sunny W. Y., Ayako Matsuoka, and Shoya Matsuda, "Isolated electrostatic potential structures observed by the Arase satellite," in *ARN 4th Symposium*, Nanjing, China, 2019.

2. Tomoe Taki, Hirotsugu Kojima, Satoshi Kurita, Yoichi Kazama, Yoshiya Kasahara, Yoshizumi Miyoshi, Iku Shinohara, Hideyuki Usui, Shoya Matsuda, Wang S.-Y., Tam Sunny W. Y., and Ayako Matsuoka, "Isolated Electrostatic Potential Structures Observed by the Arase Satellite," in *VERSIM*, Online-session, 2020.

3. Tomoe Taki, Hirotsugu Kojima, Satoshi Kurita, Yoichi Kazama, Yoshiya Kasahara, Iku Shinohara, Yoshizumi Miyoshi, Hideyuki Usui, Shoya Matsuda, Wang S.-Y., Tam Sunny W. Y., Ayako Matsuoka, "Isolated electrostatic potential structures correlated with low energy electron beams: Arase satellite observations," in *AGU Fall Meeting*, Online-session, 2020.

4. Tomoe Taki, Satoshi Kurita, Hirotsugu Kojima, Yoshiya Kasahara, Yoshizumi Miyoshi, Ayako Matsuoka, Shoya Matsuda, "Isolated Electrostatic Potentials Observed by the Arase Satellite," in *JpGU*, Online-session, 2021.

5. Tomoe Taki, Satoshi Kurita, Airi Shinjo, Satoko Nakamura, Hirotsugu Kojima, Yoshiya Kasahara, Shoya Matsuda, Ayako Matsuoka, Yoshizumi Miyoshi and Iku Shinohara, "Interferometry observation of ECH and chorus waves by the Arase satellite," in *URSI-JRSM*, Tokyo, Japan, 2022.

6. Tomoe Taki, Satoshi Kurita, Airi Shinjo, Satoko Nakamura, Hirotsugu Kojima, Yoshiya Kasahara, Shoya Matsuda, Ayako Matsuoka, Yoshizumi Miyoshi, Iku Shinohara, "Phase difference of ECH waves observed by using the interferometry observation mode of the Arase satellite," in *JpGU*, Chiba, Japan, 2023.

7. Tomoe Taki, Satoshi Kurita, Airi Shinjo, Satoko Nakamura, Hirotsugu Kojima, Yoshiya Kasahara, Shoya Matsuda, Ayako Matsuoka, Yoshizumi Miyoshi, Iku Shinohara, "Phase difference of ECH waves observed by using the interferometry observation mode of the Arase satellite," in *URSI*, Hokkaido, Japan, 2023.

Research Grant

1. This work was supported by JST SPRING Grant Numbers JPMJSP2110.